THÈSE

En vue de l'obtention du

DOCTORAT DE L'UNIVERSITÉ DE TOULOUSE

Délivré par :

Institut National Polytechnique de Toulouse (Toulouse INP)

Discipline ou spécialité :

Génie Électrique

Présentée et soutenue par :

Mme SABA AMIRDEHI

le mardi 21 juillet 2020

Titre :

Optimisation des modèles électriques du système de traction ferroviaire. Application aux essais virtuels avec l'unité de contrôle

---

Ecole doctorale :

Génie Electrique, Electronique, Télécommunications (GEETS)

Unité de recherche :

Laboratoire Génie de Production de l'ENIT (E.N.I.T-L.G.P.)

Directeurs de Thèse :

M. PAUL-ETIENNE VIDAL

M. BAPTISTE TRAJIN

Rapporteurs :

M. DANIEL HISSEL, UNIVERSITE DE FRANCHE COMTE

MME MANUELA SECHILARIU, UNIVERSITE DE TECHNOLOGIE DE COMPIEGNE

Membres du jury :

M. BRUNO SARENI, TOULOUSE INP, Président

M. BAPTISTE TRAJIN, ECOLE NATIONALE D'INGENIEURS DE TARBES, Membre

M. HUBERT RAZIK, UNIVERSITE LYON 1, Membre

MME JOHANNA VALLY, ALSTOM TRANSPORT SEMEAC, Membre

M. PAUL-ETIENNE VIDAL, ECOLE NATIONALE D'INGENIEURS DE TARBES, Membre

M. SERGIO JUNCO, UNIVERSITE DE ROSARIO, Membre

Abstract

Validation and verification are the most important issues in railway applications due to cost and security reasons. Among various methods of validation, real time simulator is the best tool due to the availability, low price, low risk of danger and so on. In this case having an accurate system model considering physical phenomena would be necessary to improve its representativity of measurements and reduce the number of tests on test bench or train.

The aim of this thesis is to develop the electrical model of traction subsystems in order to be implemented on real time simulator. To do so, the limitations are identified at the beginning of this thesis by comparing the measurements on train or test bench and real time simulator. As most of embedded models are linear, we believed that paying attention on subsystem models of the simulated traction system improve the targeted accuracy in which this implies to consider nonlinear components in virtual models. These subsystems are such as: asynchronous motor (ASM), pantograph bounce, transformer, and PEM fuel cell (PEMFC).

To improve these subsystems model, the bond graph methodology is used to model energy exchanges within traction system components. This method allows us to create the state equations of whole desired system considering physical phenomena.

The asynchronous motor model is improved considering the variation of magnetizing inductance based on state variable. The bond graph methodology leads to achieve the state equations of the system that can be easily simulated on the real time simulator. The model proposed in this thesis improves fundamental current accuracy by 7% compared to the test bench.

The pantograph bounce model considering its nonlinear arc behavior includes all significant parameters such as relative airflow, variable disconnection length in this thesis. Pantograph arc phenomenon is integrated in the input side of traction system; this allows to study the effect of pantograph bounce on railway traction system as a whole system including the power supply, catenary and power transformer. The model is established using bond graph to express differential equations of system that can be easily implemented on numerical simulators.

The improved power transformer model considers the nonlinear magnetizing inductance using the bond graph methodology. The magnetizing inductance model is provided by applying the two methodologies: Jiles-Atherton (JA) model and the combination of JA model and curve fitting method. It shows that the JA method is highly representative for the steady and transient state while the maximum value of inrush current is less than nominal value. The combination of JA method and curve fitting model permit us to have the most accurate response even when the transformer is in deep situation region; where maximum value of inrush current more than 2 times of nominal current.

The parameter identification of JA model is also studied in the case of having non ideal test condition (presence of nonlinear sensor, non-ideal voltage source, etc.). It is highlighted that an uncomplete hysteresis cycle, including extremum point and coercive field are mandatory for an

accurate parameter identification. The proposed identification process is applied to a real application case; then obtained parameters are then applied into the overall system model. Finally, the consecutive simulations are compared to experimental data obtained through traction system test bench.

Having an accurate model of proton exchange membrane fuel cell system requires considering several auxiliary circuits. However, in industrial application, the accurate model of proton exchange membrane fuel cell system and corresponding information are not often provided by the designer. Moreover, the simplicity and representativity of model is required to be compatible with overall traction system model. The model has to be suitable for system simulation and not design simulation. In this thesis, a simplified model of PEMFC system is proposed using the experimental profile mission. The impact of all the environment system of proton exchange membrane fuel cell stack is estimated using the average of polarization curve on several operational points. The parameter identification process is applied, and the obtained parameters are then applied on the overall system of fuel cell stack. Finally, the experimental data obtained through train is compared with the consecutive simulation results.

These studies are completed by doing the sensitivity analysis on the identified parameters. The compatibility of proposed models is validated by implementing the models in overall traction system simulation including the control system. The simulation results are compared by test bench measurements. The improvements of subsystems are approved.

Keywords

Bond graph methodology, asynchronous motor, power transformer, hysteresis cycle, pantograph bounce, arc resistance, PEM fuel cell, system model, train traction system simulation, parameter identification, sensitivity analysis

Acknowledgements

I wish to express my sincere appreciation to my industrial supervisor, Dr. Johana VALLY, who has the substance of a genius: she convincingly guided and encouraged me to be professional and do the right thing even when the road got tough. Without her persistent support and confidence, the goal of this project would not have been realized.

Special thanks should be given to Dr. Paul-Etienne VIDAL, my research project supervisor for his professional guidance and valuable support and to Dr. Baptiste TRAJIN for his useful and constructive recommendations on this project.

Additionally, I would also like to extend my thanks to Mr. Sylvain TASTET and Mr. Didier COLIN for their technical contribution which is truly appreciated.

My sincere thanks also go to Dr. Emmanuel BATISTA who provided me an opportunity to join their R&D team as intern, and who manage the financial support for research facilities.

I am particularly grateful for the assistance given by Alstom engineers like Mr. Maxime MELI, Dr. Michel Boyer, Dr, Sebastien BELIN, Dr. Julien D-ARBINY and technicians like Mr. Jerome LACASSAGNE and Mr. Julien PERE-JEAN-GROS and finally all the control command, power and validation groups for their contributions.

I wish to acknowledge the support, help and great love of my husband, Abbas. He kept me going on and this work would not have been easy for me without his presence. Finally, I wish to thank my parents and my sister for their patience of being far from me, well-wishes and encouragement throughout my study.

Saba AMIRDEHI

Table of content

Abstract 1
Acknowledgements 3
Table of content 4
Figures 8
Tables 12
Chapter 1 General Context 13
1.1 Introduction 14
1.2 Traction system 14
1.2.1 Traction system with DC power source 16
1.2.2 Traction system with AC power source 16
1.3 Validation and Verification Methods 17
1.3.1 Offline numerical simulation 17
1.3.2 Test bench (traction system on hardware) 17
1.3.3 Test on Train 18
1.3.4 Real time simulator 19
1.3.4.1 Definitions of real time simulation 19
1.3.4.2 Categories of digital real time simulation 20
1.3.4.3 Characteristics of real time simulator 21
1.3.4.4 Evolution of digital real-time simulation 22
1.3.4.5 Considered hardware in the loop simulator in the thesis 23
1.4 Simulated model limitation, problems and complexities on real time simulator 24
1.4.1 Asynchronous motor 24
1.4.2 Pantograph bounce 26
1.4.3 Transformer 27
1.4.4 Proton exchange membrane fuel cell 28
1.5 Conclusion 29
Chapter 2 Model proposition for traction system components 30
2.1 Introduction 31
2.2 Bond graph 31
2.2.1 The elements of Bond graph 32
2.2.2 Causalities in Bond graph 33
2.2.3 The causal path, causal loop and action chain 34

2.2.4 Analysis of a dynamic system with Bond graph 34
2.3 Proposition of models 35
2.3.1 Asynchronous motor 36
2.3.1.1 Definitions 36
2.3.1.2 Bond graph of asynchronous motor 38
2.3.1.3 State equation of asynchronous motor 39
2.3.1.4 Nonlinear magnetizing inductance 40
2.3.2 Pantograph bounce 42
2.3.2.1 Definitions 42
2.3.2.2 Model of input power chain and arc model 43
2.3.2.2.1 Power part 43
2.3.2.2.2 Pantograph bounce process 44
2.3.2.3 Bond graph of input power chain including arc 46
2.3.2.4 State equations 47
2.3.2.5 Nonlinear model of electrical arc 47
2.3.3 Power transformer 50
2.3.3.1 Definitions 50
2.3.3.2 Input power model 54
2.3.3.3 Bond graph of input power chain including nonlinear magnetizing inductance 54
2.3.3.4 State equations 56
2.3.3.5 Nonlinear magnetizing inductance characteristics 56
2.3.3.5.1 Magnetic curve modelling in transient and steady state 59
2.3.3.5.2 Magnetic curve modelling in saturation region 62
2.3.3.5.3 Magnetizing inductance final model 64
2.3.4 PEM Fuel cell 66
2.3.4.1 Definitions 66
2.3.4.2 The electrical model of PEM Fuel cell 69
2.3.4.3 Bond graph of PEM Fuel cell model 71
2.3.4.4 Equations considering nonlinear characteristics of PEMFC 72
2.3.5 Model summary 73
2.4 Solving of state equations 74
2.4.1 Numerical Methods for Differential Equations 74
2.4.1.1 The Euler method 74

2.4.1.2 The Trapezoidal method 75
2.4.1.3 The Heun method 76
2.5 Conclusion 78
Chapter 3 Parameter identification and comparison with measurements 79
3.1 Introduction 80
3.2 Parameter estimation and estimator 80
3.3 Parameter identification, simulation and comparison with measurements 81
3.3.1 Asynchronous motor model 81
3.3.1.1 Identification of magnetizing inductance model parameters 81
3.3.1.2 Comparison of simulation and measurements 83
3.3.2 Pantograph bounce 86
3.3.2.1 Parameter identification of the nonlinear arc model 86
3.3.2.2 Comparison of simulation and measurements 86
3.3.3 Nonlinear power transformer 90
3.3.3.1 Jiles-Atherton parameter identification 91
3.3.3.1.1 Example of JA model parameter identification 92
3.3.3.1.2 Identification process with complete hysteresis loop 93
3.3.3.1.3 Identification process with uncomplete hysteresis loop 94
3.3.3.1.4 Identification process by the part of a signal period with different start points 96
3.3.3.2 Measurement and simulation results 98
3.3.3.3 Curve fitting parameter identification 104
3.3.3.4 Final model of nonlinear transformer and comparison with measurements 106
3.3.4 PEM Fuel cell 107
3.3.4.1 Experimental profile mission 108
3.3.4.2 Identification of parameter of static model 109
3.3.4.3 Identification of parameter of dynamic model 110
3.3.4.4 Comparison the simulation results with experimental 111
3.4 Conclusion 114
Chapter 4 Traction system experimental measurements, comparison with simulation, sensitivity analysis 116
4.1. Introduction 117
4.2. Validation of proposed models in the overall traction system simulation 117

4.3. Sensitivity analysis 124
4.3.1. Sensitivity functions and definitions 124
4.3.2. DOE definitions and method 126
4.3.3. Applying the sensitivity analysis on proposed models 127
4.3.3.1. Transformer transfer function 128
4.3.3.2. Numerical Estimation and Design of Experiments on transformer model 130
4.3.3.2.1. Impact of individual parameters 132
4.3.3.2.2. Impact of parameter interactions 133
4.3.3.2.3. Sensitivity analysis summary 135
4.4. Conclusion 136
Chapter 5 Conclusions and perspectives 137
Appendix 141
A.1. ASM 141
A.2. Pantograph bounce 143
A.3. Transformer 143
A.4. PEMFC 145
A.5. Numerical solutions for the state equations 148
References 151

Figures

Figure 1-1 An example of traction system 14
Figure 1-2 Two traction system with (a) DC and (b) AC power supply 15
Figure 1-3 Comparison of test cost between different ways of testing (based on internal confidential Alstom document) 19
Figure 1-4 Offline simulation 20
Figure 1-5 Real time simulation 20
Figure 1-6 Basic concept of CHIL 21
Figure 1-7 Real time simulator (based on internal confidential Alstom document) 23
Figure 1-8 Normal Magnetization curve 25
Figure 1-9 Comparison results of simulation results of ASM model considering constant magnetizing inductance and test bench results 25
Figure 1-10 Primary voltage and current of transformer on (a) train measurements and (b) real time simulator in the condition of pantograph bounce 26
Figure 1-11(a) Primary contactor to energize the transformer, (b) primary voltage of transformer, (c) rectified voltage of secondary after preload circuit and (d) primary current of transformer on test bench measurements, (e) primary contactor to energize the transformer, (f) primary voltage of transformer, (g) Rectified voltage of secondary after preload circuit, (h) primary current of transformer on real time simulator 27
Figure 1-12 (a) Characteristics of fuel cell on train (b) on real time simulator 28
Figure 2-1 Power transfer between two subsystems using Bond Graph 32
Figure 2-2 Paynter tetrahedron 32
Figure 2-3 The causality of transformer and gyrator 34
Figure 2-4 The causality of 0-junction and 1-junction 34
Figure 2-5 An Example of Electrical circuit 35
Figure 2-6 The bond graph of electrical circuit shown in figure 2-5 35
Figure 2-7 Traction system bond graph 35
Figure 2-8 Electrical model of asynchronous motor 36
Figure 2-9 Electrical model of asynchronous motor in (α, β) axles with transferred rotor in stator part 37
Figure 2-10 The complete bond graph of asynchronous motor in two axles of (α, β) 38
Figure 2-11Traction system bond graph considering the causality of ASM 39
Figure 2-12 The datasheet information of ASM (a) rotor flux vs magnetizing current (b) magnetizing inductance vs rotor flux 40
Figure 2-13 The block diagram of the incremental magnetizing calculation in this thesis 41
Figure 2-14 Pantograph arcing phenomenon (based on internal confidential Alstom archive) 42
Figure 2-15 Power supply, catenary and traction system including arc resistance 44
Figure 2-16 Pantograph bounce total process 44
Figure 2-17 Pantograph bounce total process without arc extinguished step 45
Figure 2-18 The bond graph of input power chain including state variables shown in red 46
Figure 2-19 Traction system including the causalities of substation, catenary, arc model and ASM model 46

Figure 2-20 Ideal transformer with primary and secondary windings 50
Figure 2-21(a) voltage of inductor (b) calculated flux (c) hysteresis characteristics of inductance (d) computed current of inductor (Inrush current) 52
Figure 2-22(a) voltage of inductor (b) calculated flux (c) hysteresis characteristics of inductance (d) computed current of inductor (magnetizing current) 53
Figure 2-23 Equivalent circuit of single-phase power transformer 53
Figure 2-24 Input power chain including nonlinear model of transformer 54
Figure 2-25 Bond graph of input power of traction system including substation, catenary and non-ideal transformer 55
Figure 2-26 Traction system bond graph considering the causalities 55
Figure 2-27 Ideal magnetic curve 57
Figure 2-28 Non-ideal magnetic curve 57
Figure 2-29 Experimental characteristic of magnetizing inductance in saturation region 58
Figure 2-30 Magnetic flux and magnetic current with extracted peak values 63
Figure 2-31 (a) Extracted peaks of magnetic flux and magnetizing current (b) Mirrored of figure 2-31 (a) 64
Figure 2-32(a) the basic structure of PEMFC single cell (b) Stack (c) system 67
Figure 2-33 PEM FC stack and auxiliary circuits 68
Figure 2-34 Electrical circuit model of PEMFC 71
Figure 2-35 The bond graph of PEMFC 71
Figure 2-36 The causalities in the bond graph of traction system including PEMFC system 71
Figure 2-37 Characteristics of PEMFC single cell in steady state 73
Figure 2-38 Geometric illustration of Euler's method 75
Figure 2-39 Geometric illustration of Trapezoidal method 75
Figure 2-40 Geometric illustration of Euler method and prediction line 76
Figure 2-41 Geometric illustration of Heun method 76
Figure 3-1 Parameter estimation architecture [124] 80
Figure 3-2 Magnetizing inductance based on the datasheet 82
Figure 3-3 Comparison of simulated magnetizing inductance and the datasheet information 82
Figure 3-4 Traction system with DC voltage supply 83
Figure 3-5 Simulation environment 84
Figure 3-6 Comparison of stator current on fundamental frequency on test bench, simulation with and without nonlinear model of magnetizing inductance 85
Figure 3-7 high speed train developed in Alstom transport 86
Figure 3-8 Measurements on voltage of input power chain 87
Figure 3-9 Simulation environment for pantograph bounce model 88
Figure 3-10 Comparison of arc voltage in measurement with simulation one 89
Figure 3-11 Primary voltage of transformer on train and simulation in presence of arc phenomenon 89
Figure 3-12 The preference of two methodology of magnetizing inductance model 90
Figure 3-13 Model of transformer with no load. 92
Figure 3-14 Hysteresis loop of transformer with the JA parameters in table I. 93

Figure 3-15 Uncomplete hysteresis loop (based on percentage of one period of hysteresis loop 20-40-60-80%) 95
Figure 3-16 The difference of JA parameters achieved by percentage of period compared to initial JA parameters..... 95
Figure 3-17 Relative error for coercive, remanence field and hysteresis area calculated for each hysteresis loop..... 96
Figure 3-18 Uncomplete hysteresis loop with different start point for identification 97
Figure 3-19 Measured primary current of transformer (Ip(A)) 99
Figure 3-20(a) Measured primary voltage of transformer ($Ucat2$), (b) Measured primary current of transformer (Ip), (c) Calculated magnetic flux of transformer ($\emptyset m$) and (d) Calculated magnetizing current of transformer (Im) 99
Figure 3-21(a) Computed hysteresis cycle using measurements ($B-H$), (b) Filtered hysteresis cycle. 100
Figure 3-22 two selected part of hysteresis cycle with and without extremum points for identification process..... 100
Figure 3-23 Comparison of measurement and simulated hysteresis cycles 101
Figure 3-24 Comparison of simulation result and measurement of primary current..... 102
Figure 3-25 (a) Primary voltage of transformer and contactor closure time (b) Primary current of transformer on testbench..... 102
Figure 3-26 Inrush current comparison between simulation using JA model and measurements 103
Figure 3-27 Primary voltage of transformer on test bench 104
Figure 3-28 Primary current of transformer by several contactor closure..... 104
Figure 3-29 Experimental peaks of magnetic flux vs peaks of magnetizing current..... 105
Figure 3-30 Inrush current comparison between simulation using curve fitting model and measurements 106
Figure 3-31 Inrush current comparison between simulation using the combination of curve fitting and JA model and measurements 107
Figure 3-32 Polarization curve of PEMFC system impacted by subsystems 107
Figure 3-33(a) measured current and (b) voltage of PEMFC system..... 108
Figure 3-34 Measured voltage response versus the current extracted from profile mission for 3 hours of test procedure 109
Figure 3-35 Average voltage-current points for profile mission in last 2 hours of measurements 110
Figure 3-36 The selected part of measured voltage and current to identify the parameters of dynamic model 111
Figure 3-37 Comparison of measured output voltage of PEMFC system and the simulated one using identified parameters..... 112
Figure 3-38 (a)Comparison of measured voltage and current of PEMFC system on train and the simulated one, example of voltage comparison in (b) mode 1 and (c) mode 2..... 112
Figure 4-1 Block diagram of the overall system test platform for high speed project 118
Figure 4-2 Test bench environment including the AC voltage source, the main contactor, transformer, power modules (converters and rheostat chopper), ASM and control system .. 118
Figure 4-3 The acquisition system and its interface 119

Figure 4-4 The interface software and manipulator in test bench 119
Figure 4-5 The applied percentage of manipulator and recorded speed on test bench..... 120
Figure 4-6 Overall traction system simulation blocks 121
Figure 4-7 (a) Comparison of simulated primary current of transformer and measurements (b) without traction (0% of manipulator and 0 km/h of speed) (c) with traction..... 122
Figure 4-8 Comparison of simulation and test bench result of stator current of ASM..... 123
Figure 4-9 Bond graph of overall traction system 127
Figure 4-10 Bond graph of transformer in test bench condition and isolated secondary ... 128
Figure 4-11 Bode diagram of transfer function (a) $IpsUcat2s$ (b) $ImsUcat2s$ 129
Figure 4-12 Magnetizing inductance variation effect on fundamental frequency of the state variables 130
Figure 4-13 The main effect of Jiles Atherton parameters 133
Figure 4-14 Interaction plots between parameters (a) (a with α) , (b) (a with k), (c)(a with c) , (d) (k with α) (e) (c with α) and (f) (c with k) 134

Tables

Table 1-1 Summary of advantage and disadvantage of validation tools 18
Table 2-1 Equivalent variables of bond graph in different physical domain..... 32
Table 2-2 Bond graph junctions..... 33
Table 2-3 Model parameters 74
Table 3-1 Identified parameters of magnetizing inductance equation..... 82
Table 3-2 Comparison of amplitude of stator current on fundamental frequency..... 85
Table 3-3 Magnetizing inductance variation for different operational points 85
Table 3-4 The identified parameters of electrical arc 88
Table 3-5 Transformer electrical magnetic parameters 92
Table 3-6 Boundaries of JA parameters used in simulation 93
Table 3-7 Parameters achieved by 100% of a period 94
Table 3-8 Relative error of JA parameters achieved by different start points compared to initial JA parameters..... 97
Table 3-9 Relative error of JA parameters achieved by different start points compared to JA parameters achieved by 20% of period 97
Table 3-10 Relative error of hysteresis cycle area..... 98
Table 3-11 Transformer electrical parameters..... 98
Table 3-12 Identified JA parameters..... 101
Table 3-13 Identified parameters of proposed equation for magnetizing inductance on deep saturation region..... 106
Table 3-14 Identified parameters of PEM Fuel cell model..... 111
Table 4-1 Comparison of simulated current peak and measurement in zone 2 of figure 4-7 123
Table 4-2 Example of experimental plan for DOE method for 2 factors and 2 level..... 126
Table 4-3 Full 24 factorial design experiments of JA parameters and the simulation results for all the combinations..... 131
Table 4-4 The rearranged of Table 4-3 to calculate the parameters of equation (4.12) 132
Table 4-5 The effect of each JA parameter on the maximum peak of primary current..... 132
Table 4-6 The rearranged of Table 4-3 to calculate the parameters of equation (4.14) 133
Table 4-7 The effect of parameter interactions on the maximum peak of primary current 133
Table 4-8 The effect of parameter interactions (3 and 4 parameters) on $Ipmax$ 134

Chapter 1

General Context

1.1 Introduction

The railway applications like all transport applications face some energy and economic constraints. The design method of railway system should provide the economic gain in verification and validation process. The verification and validation process and its corresponding methods would have an important role in economic aspects of industrial railway. Traditionally, validation and verification procedures are done in three main methods which are: simulation method on computer (offline simulation), test bench and test on train respectively. These three methods of validation have several advantages and disadvantages in economic aspects and the result accuracy. Following these advantages and disadvantages, real time simulator is known as a best validation tool which can be representative of train or test bench. This can be possible if the whole train system is implemented accurately on real time simulator. In this chapter, the railway system that do the traction is explained generally and then advantages and disadvantages of four different methods of validation (above mentioned) are explained and compared in several aspects. The model requirements of actual real time simulator are obtained and expressed by comparing the results of real time simulator with the one on train or test bench.

1.2 Traction system

A traction system consists of train components. It comprises the installed systems, from electrical energy network as an input of whole train system to mechanical system which result the output. Traction system converts the electrical energy which is captured by pantograph from catenary to mechanical energy, at the wheel level. The management of the converted energy allows the wheels to turn and the train can accelerate or brake. Figure 1-1 shows an example of traction system in railway application. The traction system is usually composed of an electrical power source (AC or DC), of a transformer, which role is to adapt the AC voltage level, of converters to do the conversion of AC/DC, DC/AC or regulate the level of voltage, of motors to lunch the cinematic to do the traction.

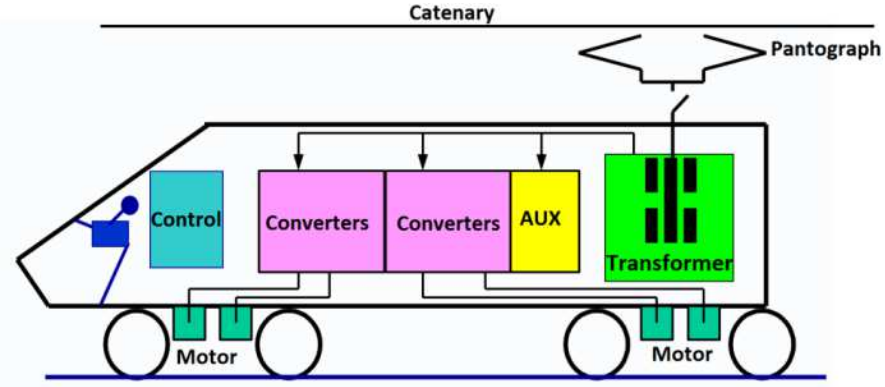

Figure 1-1 An example of traction system

However, depending on power source with its different level of voltage and frequency, the traction system can have different forms. Figure 1-2 illustrates two traction system with DC

and AC power supply including auxiliary and control system. A part of traction system from converters to motor is called traction chain (shown by red dot dash in figure 1-2). The traction chain including auxiliary and control system are implemented in motor block (shown in green dash in figure 1-2).

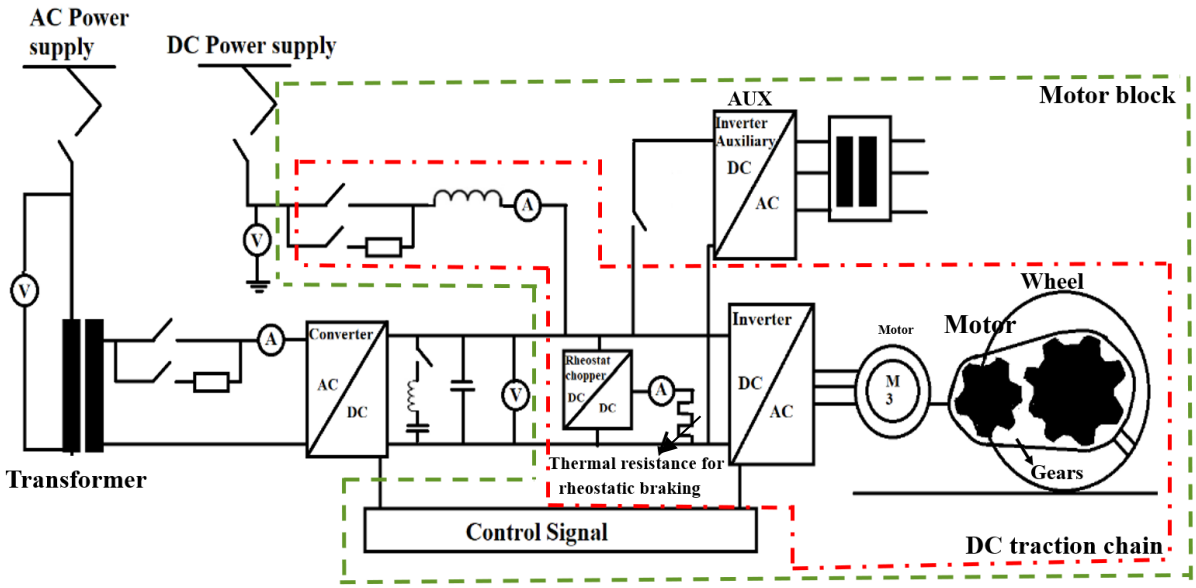

(a)

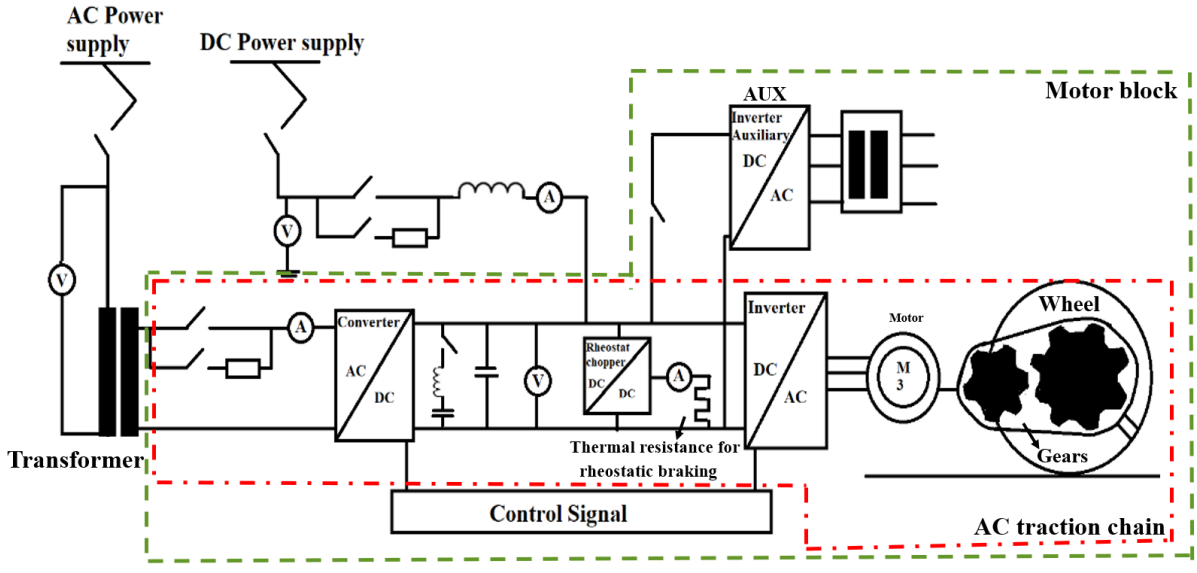

(b)

Figure 1-2 Two traction system with (a) DC and (b) AC power supply

Depending on project requirements, it is possible to have several traction chains in a motor block and/or several motor blocks for one traction system. In section 1.2.1 and 1.2.2, two different structure of traction system are explained.

1.2.1 Traction system with DC power source

In traction system with an input DC power source, it is possible to have: the power source using catenary and pantograph, third rail in metro project, fuel cell and battery applications, supercapacitors etc. Figure 1-2 (a) shows the traction system with DC power source. Before connecting the source to the whole traction system, it is needed to have main circuit breaker to protect an electrical circuit from damage caused by excess current from an overload or short circuit. To supply the traction system, there is a contactor to connect the traction system to the network. In order to avoid overshoot voltage at the instant of contactor closure, a preload circuit is considered to decrease the instantaneous value of voltage and increase it slightly. After preload process, depending on the design of traction system, it is needed to have a chopper to reduce the value of DC voltage. After filtering of the reduced DC voltage, it has to be converted to AC voltage using inverter in order to be injected to AC motor (Synchronous or Asynchronous). The mechanical part connected to AC motor has a role as the output section of traction system. Due to the gears between electrical motor and mechanical wheel, the speed of the train will be proportional of motor speed.

1.2.2 Traction system with AC power source

In the case of AC power source as an input of traction system, the voltage of source can reach 25 kV in some cases, shown in figure 1.2 (b). Therefore, in order to be used for traction, it is needed to reduce it by a transformer. Then, a rectifier is added on the secondary of transformer. The rectifier is a converter with four semiconductors that allows feed a DC bus under one phase catenary. This converter regulates the DC output voltage, prepares a power factor close to 1 (Catenary current is almost sinusoidal and in the same phase as voltage) and recovers the energy while braking. After rectifying the voltage, an inverter is needed to produce an AC and three-phase voltage for motor part. The rest of the traction system is similar as the DC traction design (Figure1-2 (b)).

The braking system in traction system operate in three different forms. Magnetic braking, dynamic and pneumatic braking. There are two possibilities to do the dynamic braking: regenerative and rheostatic braking. To do the regenerative braking, the current of motor is sent back to the network. While it is not possible for the source to accept all the returned current, rheostat braking is the second way to do the dynamic braking. This is done using a resistance load fed by a DC/DC converter on DC bus. Pneumatic braking is applied in low braking effort. It is also used in high speed by conjugating with dynamic braking.

There are also two different types of auxiliary system (AUX in figure 1-2) in both case of traction system to control energy for cooling system inside traction system such as transformer and motor and to prepare electrical supply for passengers.

All converters, switches and circuit breakers are controlled and receive the commands. The commands are generated by a control system. To ensure the harmonic features, power losses etc., the control system applies PWM methods on converters (rectifier and inverter).

To validate and verify modifications and new propositions on traction system, there are several methods. Offline numerical simulation, testbench and train are traditionally employed to do these procedures. However, each method has some advantages and disadvantages and in addition, it is employed for a specific purpose. In section 1.3, different validation and verification methods are explained in detail.

1.3 Validation and Verification Methods

Validation and verification process and its corresponding methods have the important role in economic aspects of industrial railway. Therefore, it is necessary to choose the best way to do the validation in terms of cost and security as well. In this section, offline numerical simulation, test bench, test on train are explained in detail and their advantages and disadvantages are discussed. Real time simulator is also illustrated as a new tool validation.

1.3.1 Offline numerical simulation

Simulation is the representation of real-world process or system behavior. In order to describe a system, a model has its own conceptual framework. Simulation of power system on computer involves power system modelling and network simulation with mathematical equations. It is usually used to analyze electrical power systems in the case of validation, modification, new model propositions and testing on degraded modes using offline data.

This method is the best suited to analyze complex and large practical problems when it is not possible to solve them with mathematical method. It is flexible, available and the least expensive way in verification process. It is more available and less expensive than other procedures. It is easy and fast to change the configuration of whole system and doing the test of degraded modes by simulation. Policy decision can be made much faster by knowing the options well in advance and by reducing the risk of experimenting in real system. However, the results from simulation on computer are sometimes not enough accurate. This is often due to the fact that the simulation is not based on real measurements inputs and is not associated with a real control system. Therefore, this method can be sufficient in the first step of validation, planning, design and implementation of system in order to make an initial decision. However, to have reliable results of validation, it is necessary to use a method in real time with real environment condition [1].

1.3.2 Test bench (traction system on hardware)

The second method of validation is test bench. Test bench or testing on workbench is an environment used to verify and validate the correctness of a design. The test bench is an environment with traction and control system. A reliable power source is also needed for developing and testing the traction system in variety conditions which is representative of substation and catenary. In the test bench a technician does the test manually with measurement and manipulation tools such as oscilloscope, multi meters and so on.

Validation process and results from test bench are more reliable compare to offline numerical simulation on computer. It is a real time control and the characteristics of each component in traction system is quite the same as train condition. However, due to the simplicity of traction system i.e. considering one motor block instead of several on train, the impact of elements in one motor block to another one can not be detected. Generally, the validation of system in the aspects of performance (Effort vs speed curve), norms, acoustic and thermal are done on test bench.

The disadvantages of doing tests on test bench are unavailability, high price and risks of danger. Therefore, there are several limitations on doing some kinds of test such as: effect of electrical arc of pantograph and test on degraded mode. It is not also easy to change the configuration of traction system in order to do some specific tests.

1.3.3 Test on Train

The last step to validate and verify the train systems (figure 1.4) is doing the test on real train prototype directly. In this case the tests are done in real operating conditions. Therefore, the results are the most reliable compare to the other methods of testing.

By this way, it is also possible to observe different phenomena that can not be predicted or reproduced in test bench. However, this step of validation is the most difficult compare to the other methods because there are several risks of danger during the test procedure. Testing on degraded mode is more complicated compare to test bench therefore it is the least flexible way. It is also too expensive and not always available to do different tests.

Based on all the explanation, advantages and disadvantages of different validation method in sections 1.3.1 to 1.3.3 which is summarized in Table 1-1, it is necessary to a have an alternative for testing which is much more economic and more safety.

Table 1-1 Summary of advantage and disadvantage of validation tools

Validation Tools	**Advantage**	**Disadvantage**
Offline simulation	Low cost No risk of danger Availability	Reliability (It is not representative of measurements on train)
Test bench	Reliability	Expensive Unavailability
Train	Reliability	Expensive Unavailability Risk of danger

The best way would be a tool that has the advantages of simulation on computer such as flexibility, lower price, availabilities and the representative of test bench and train. This is the purpose of real time simulation [2] which is explained in detail in the following.

1.3.4 Real time simulator

Real time simulators have been used extensively in the planning and design of electrical systems for decades [2]. This validation tool has flexibility of doing the test in different conditions like offline numerical simulation thanks to mathematical modelling of power system, but it receives the control signals from hardware part like test bench or train. In this case there are real signals and the simulations are done in real time depending on computation complexities. This validation method has less risk of danger and prices compare to the other validation methods. Figure 1-3 depicts the cost comparison of different validation method with real time simulator method.

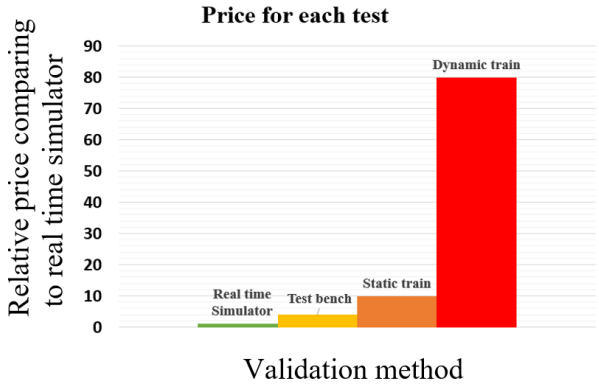

Figure 1-3 Comparison of test cost between different ways of testing (based on internal confidential Alstom document)

As shown in figure 1-3, the price of each test on simulator is 80, 10 and 4 times less than test on dynamic train, static train and test bench one, respectively. Therefore, it would be more reasonable to do the greatest number of tests on real time simulator. Following sections explains the real time simulation, different structure of real time simulators and the one used in this thesis.

1.3.4.1 Definitions of real time simulation

Since the early 1950s, simulation tools have supported the development of engineering systems. The fast simulation of a complex system is possible by the powerful computing available today [3]. It is more valuable in control systems simulation because the computer model must run at the same rate as the actual physical system (real time) [3], [4]. Nowadays, real time simulation has a critical role across several stages of the technology chain that enables the transfers of new control concepts into successful power products [4]. In real time simulation, it is desired to reproduce the representative output waveform of a power system with a desired accuracy. To do so, the models of power systems are simulated on a hardware platform employing computation. To solve the mathematical model equations of power systems and determine the state variables at a given step time, two possibilities can occur depending on the computation time and real-world clock for one step time [5]:

1. If the execution time for the simulation of all variables of system (T_{exe}) is greater than its selected step-time, the overrun will occur, and simulation is offline or non-real time simulation (Figure 1-4) which means simulation will be uncomplete in real time simulator.

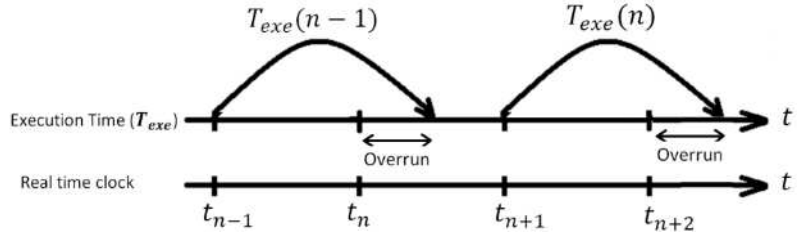

Figure 1-4 Offline simulation

During the offline simulation, the aim is to obtain results as fast as possible. And this objective depends on available computation capabilities and the computation complexity.

2. If the execution time for the simulation of all variables of system T_{exe}, is shorter or equal to the selected step time, the simulation is real time (Figure 1-5).

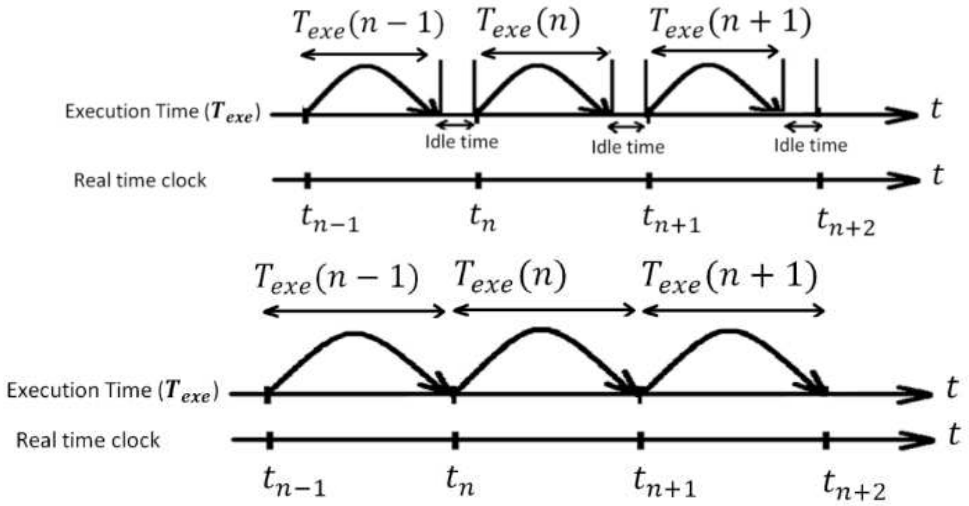

Figure 1-5 Real time simulation

Note that Idle time is the time difference between T_{exe} and selected step time.

It means that the simulator has to perform all the operations necessary such as driving inputs and outputs (I/O) to and from externally connected devices to make a real time simulation. Therefore, it is expected that real time simulator would be able to solve all equations and states of the simulated system accurately for one step-time within the same time in real-world clock, with an acceptable resemblance to its physical counterpart [6] and [7].

1.3.4.2 Categories of digital real time simulation

There are two type of digital real time simulation in power systems [8]: the fully digital real time simulation and the hardware in the loop.

1- Fully digital real time simulation

In this type of simulation, the whole system such as control, protection and other accessories are modelled inside simulator and there are no external interfaces as an input or output (I/O).

2- Hardware in the loop

In hardware in the loop, some parts of fully digital real time simulation such as filters, digital to analog converter, analog to digital converter and signal conditioners are replaced by actual physical components. Control of real time simulation can be executed with user-defined control inputs, like, closing or opening of switches to connect or disconnect the components in the simulated power system. In this type of simulation, if there is a real controller hardware which has connection with rest of the simulated system, it is called Controller Hardware in the Loop (CHIL). The power system is modeled as a virtual system inside the simulator and the external control system has an exchange as I/O with the system inside the simulator. Figure 1-6 shows the basic concept of CHIL.

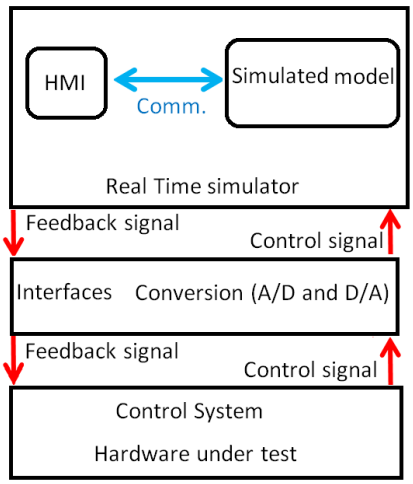

Figure 1-6 Basic concept of CHIL

In general, a fully digital simulation is often used for understanding the behavior of a system under certain circumstances resulting from external or internal dynamic influences. Whereas hardware in the loop simulation uses a prototype which is established with the help of a fully digital real time simulation in order to minimize the risk of investment [8].

1.3.4.3 Characteristics of real time simulator

Most of digital real time simulators have common characteristics such as [8]:

- **Multiple processors** which forms the target platform when the simulation runs in real time.
- **Host Computer:** In order to have offline model, compiling and then load it on target platform, host computer is used. It is also used for monitoring the results of real time simulation.

- **Input / Output (I/O) Terminals** which are used as interfaces with external Hardware.
- **Communication network:** When the model is split into multiple subsystems, it is needed to have a network in order to exchange data between multiple targets. It is also needed to have a separated communication link in order to exchange data between host and the target.

1.3.4.4 Evolution of digital real-time simulation

In 1991, the first commercial real time digital simulator (RTDS) was demonstrated by RTDS Technologies Inc. using DSPs [9]. In order to evaluate its performance, it was connected to a high voltage direct current controller [3]. There was also a combination of digital and analog parts in that kind of simulator. This kind of RTDS became a widely used commercial simulator. Its small-scale was used for real-time test of the power system equipment called Digital Transient Network Analyzer (DTNA). This digital real time simulator was based on multipurpose parallel computer system [10]. The DTNA simulators had ability to simulate electromagnetic phenomena up to 3 kHz, AC/DC interactions, electromechanical transients, and similar longtime phenomena. With that feature, it was possible to simulate a wide variety of components, equipment, and controllers associated with power electronics.

Before 1996, there was no fully digital real time simulator. Électricité de France created the first real time simulator ARENE [11] which was able to simulate the high frequency phenomenon in a standard, multipurpose parallel computer. SIEMENS proposed NETMAC which was PC-based real time simulator. It was used to simulate large power grids [12] and [13]. OPAL-RT Technologies Inc. introduced general-purpose processor-based real time simulator [14]-[18]. This simulator uses MATLAB/Simulink as a main modeling tool for the simulation. Another fully digital real-time simulator for analyzing the electromagnetic and electromechanical transient in large and complex power system is called HYPERSIM [19]-[21].

There are also some upcoming simulators in future. These real time simulators use a combination of hardware and software to be used in some specific requirements. Due to being user-friendly, block coding, automatic code generation capability and interfacing capability with Simulink, the hardware is used as an auxiliary platform of large simulators. This allows to model and then to simulate a system within a time step of nanoseconds while the main simulation runs at a larger time-step (in microsecond) [8]. In future real time applications, to improve the power of computation, FPGA (Field Programmable Gate Array) applications are going to replace by DSPs (Digital Signal Processing) which means that the simulated model would directly be implemented on FPGAs. In this case, the parallel computations will be enabled by FPGA which consequently the minimum simulation time step will decrease to several microsecond approximately [22].

1.3.4.5 Considered hardware in the loop simulator in the thesis

In this thesis, a hardware in the loop simulator is considered which does the digital simulation with discrete-time and constant step time. Figure 1-7 shows the configuration of real time simulator used in this thesis:

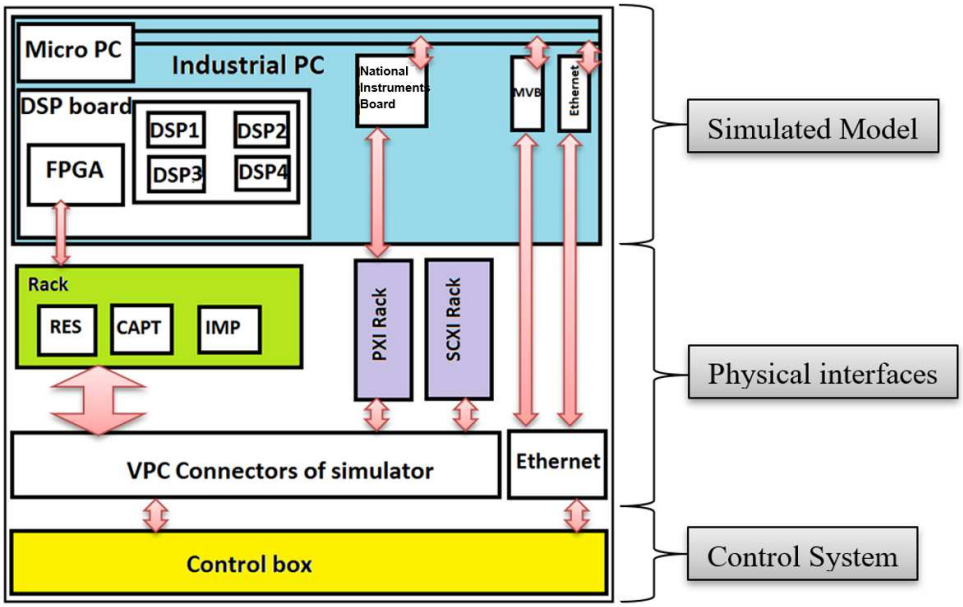

Figure 1-7 Real time simulator (based on internal confidential Alstom document)

As it is discussed in section 1.3.4.2, there are three main parts in hardware in the loop simulator (Figure 1-7). Simulated model of traction system is implemented on four DSPs. Sources and converter model are implemented on DSP1, loads such as filters, motors, inverters, rheostat chopper, etc. on DSP2 and DSP4 and the kinematic part on DSP3. All these DSPs dialog with physical interfaces through FPGA. The physical interfaces make connection between control part and industrial PC.

Based on the advantages of real time simulator, it would be more interesting to do the major part of the validation process on it. This means that real time simulator has to be enough representative of reality. This could be possible if the whole railway system and the effect of environment would be implemented accurately on real time simulator with enough accuracy. The aim of this thesis is to complete or develop the electrical model of the components involved in typical railway traction system. To improve the simulated model of traction system and physical phenomena, it is required to detect the limitations of traction system subsystem. To identify the limitations of simulated models embedded into the actual simulator, the comparison has to be done between the results on real time simulator and measurements. Some criteria of inaccuracy that have to be stated, will be based on real measurements either on test bench or train.

In next section, the important problems and limitations on simulated model of different part of traction system is explained by comparing the results of measurement on test bench and/or train and real time simulator.

1.4 Simulated model limitation, problems and complexities on real time simulator

The virtual model has to take into account the physical phenomena. To represent the virtual model of traction system, state equations are required considering input and output of system. In simulated part of real time simulator (industrial PC), state equations of each component model are solved, and it resulted the output of system.

Based on all advantages of real time HIL simulator explained in last sections, it is important to have a complete and accurate virtual model for whole traction system. To develop the virtual model of traction system, it is necessary to detect the limitations of existing models on simulator. The limitations can be detected by doing the comparison between the measurements on real time simulator and on experimental measurements on different components of traction system. Based on the comparison of voltage and current in different situations on traction system, the inaccuracy is mainly detected in the simulated models. As most of embedded models are linear, we believed that paying attention on subsystem models of the simulated traction system will improve the targeted accuracy. That implies to take into account nonlinear components in virtual models. These subsystems are such as asynchronous motor, pantograph bounce, transformer, and PEM fuel cell based on Alstom needs. Effectively, the limitations from catenary to motor are probably associated to lack of impedance model of catenary model based on distance from substation, pantograph bounce and arc modelling, inrush current model in transformer, up to date model of fuel cell, complex model of asynchronous motor including magnetizing inductance. In section 1.4.1 to 1.4.4, the detected complexity and limitations of electrical model of mentioned subsystems on real time simulator are explained in detail.

1.4.1 Asynchronous motor

In design of asynchronous motor (ASM) and modelling of real drive motor systems, the equivalent circuit model of ASM and its lumped parameters are widely applied. In order to produce desired performance of motor e.g. vector control systems where electromagnetic state of the motor is estimated and controlled, the lumped parameters have to be determined correctly. However, the lumped parameters are not constant following load conditions. Magnetizing inductance is one of the lumped parameters which changes according to magnetization curve ($B-H$) (magnetic induction - magnetic field).

As ASM is constructed by ferromagnetic material, it has a nonlinear behavior in the case of applying an external magnetic field. This nonlinear behavior is due to nonlinear permeability of material. This can be graphed by the quantity of magnetic field (H equal to field force (mmf) divided by the length of material) and magnetic induction (B equal to flux density divided by cross section area of material). Figure 1-8 shows a normal magnetization curve or $B-H$ curve.

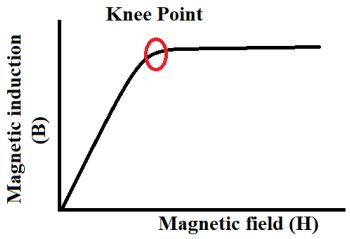

Figure 1-8 Normal Magnetization curve

Depending on the materials, knee point is different which shows the saturation effect. This point means as more flux apply to the cross-section area, fewer atoms are available to align their electrons so it takes more and more magnetic field force to have a little augmentation in flux density. Therefore, the magnetization curve determines the magnetizing inductance characteristics by flux linkage against magnetizing current. Generally, the motor magnetization curve obtained by no load test is linear in the non-saturation region, therefore, magnetizing inductance can be considered as constant parameter. However, in the case of variation of motor load, the operating points on nonlinear $B-H$ curve also vary. Hence, magnetizing current is changed. Based on its characteristic, the magnetizing current increases by increasing the load on motor and for large value of magnetizing current, the magnetization curve become nonlinear. Thus, it would be necessary to determine the nonlinear magnetizing curve that would give us reliable results of magnetizing current for different load conditions. The nonlinear magnetization curve can be accurately acquired by standard no load test on motor or some other methods proposed on different literatures [24, 25]. Let us remind that in the beginning of thesis, this parameter is considered constant in actual model of ASM on real time simulator.

To demonstrates the effect of magnetizing inductance in the ASM model, a comparison is done between the simulation results considering the constant magnetizing inductance (the same model as actual ASM model on real time simulator) and Alstom test bench results. Several operating points (demand of speed) are demanded from traction system feed by a DC source (1500V). The ASM stator current at fundamental frequency were different for these operating points. Figure 1-9 shows the comparison of stator current at fundamental frequency between simulation with constant magnetizing inductance and test bench. Note that the stator current at fundamental frequency is in per unit (it is united by the nominal current of ASM).

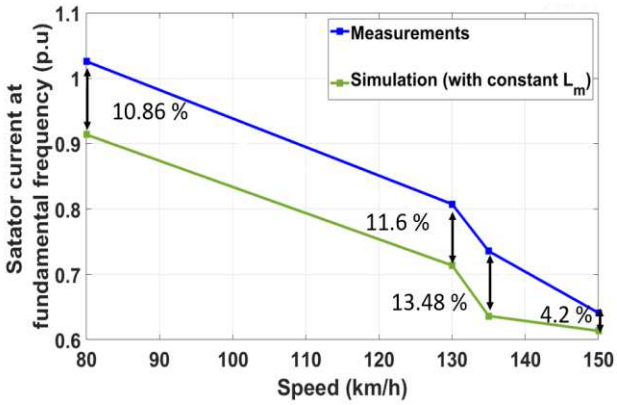

Figure 1-9 Comparison results of simulation results of ASM model considering constant magnetizing inductance and test bench results

As it is shown in this figure, the relative error between simulation and test bench results are high at speed of 135 km/h, 130 km/h and 80 km/h and it is more than the acceptable error in the industrial point of view which is less than 5%. This is due to the constant value of magnetizing inductance considered in the actual model of ASM in real time simulator. Therefore, having a model of ASM with corrected parameters at every operating point is necessary. The proposed ASM motor model for real time simulator are explained in detail in chapter 2.

1.4.2 Pantograph bounce

In electrified railway applications, the traction power input is fed by sliding contact between contact wires called pantograph and catenary. During the power supplying process, the oscillations and vibrations between catenary and pantograph are encountered due to the irregularity of catenary or high speed of train. The vibration causes the separation of pantograph from contact wire which leads to have an electrical arc. The electrical arc on pantograph causes the current flowing to be deformed with high frequency transient. The transient current will significantly deteriorate the power quality of power system. The test process to reproduce pantograph bounces is risky and dangerous. Therefore, it is important to have virtual model of this phenomena in order to be able to predict and analyze the effect of electrical arcing on power input system. However, the correct behavior and model of arc phenomena is not considered in real time simulator at the beginning of the work. Figure 1-10 shows the effect of pantograph bounce on voltage and current of catenary on train and real time simulator.

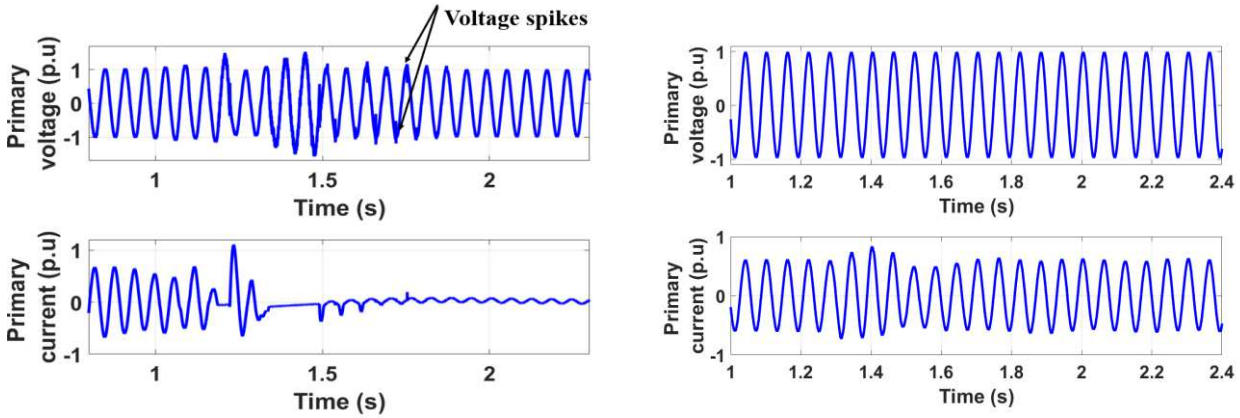

(a) (b)

Figure 1-10 Primary voltage and current of transformer on (a) train measurements and (b) real time simulator in the condition of pantograph bounce

As it is shown in figure 1-10 (a), electrical arc causes several spikes on the input voltage of traction system and it deforms the current shape. However, the results from real time simulator show only a reduction on primary current due to the arc electric and it does not change the input voltage (figure 1-10 (b)). This means the electrical model of arc implemented on real time simulator is not enough accurate to reproduce the real phenomena and it has to be improved. This will the purpose of a section of chapter 2.

1.4.3 Transformer

One of the most common nonlinear elements in traction system is the transformer. It is also an important element in power systems since its continuity of operation has a huge importance in maintaining the reliability of power supply. The development and validation of transformer performance require the preliminary determination of transformer model. As an example, the re-energization of an unload power transformer may generate high nonsymmetrical magnetizing currents, known as inrush current. These transient currents can reach up to 5 times of the rated current and decrease for up to several seconds. Figure 1-11 (a) shows the behavior of primary current of transformer on test bench while energization and preloading. When the primary contactor is closed, the transformer will be energized. As it is shown in figure 1-11 (d), the primary current has huge value which is about 2 times more than nominal current. This phenomenon is due to the nonlinearity caused by magnetizing characteristics of the transformer iron core. After several seconds, the preload is done to avoid the overshoot of voltage and then the secondary of transformer is connected to voltage bus. However, as it is shown in figure 1-11 (h), there is no current during the energization of transformer on real time simulator.

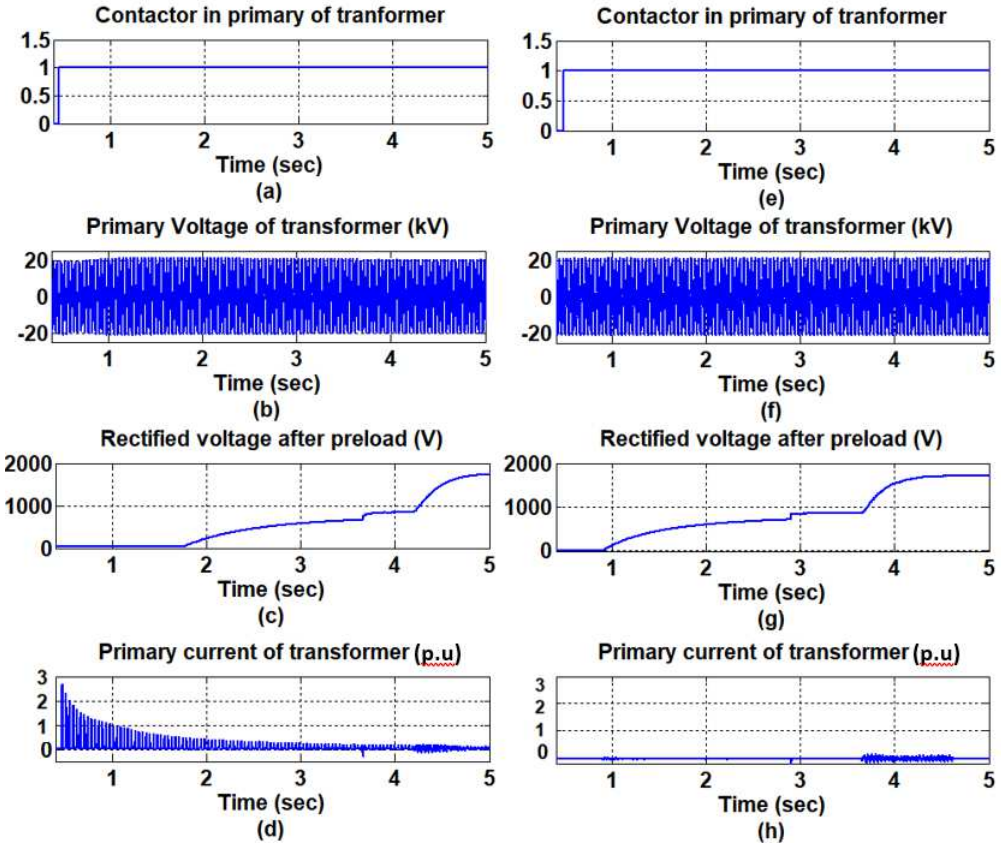

Figure 1-11(a) Primary contactor to energize the transformer, (b) primary voltage of transformer, (c) rectified voltage of secondary after preload circuit and (d) primary current of transformer on test bench measurements, (e) primary contactor to energize the transformer, (f) primary voltage of transformer, (g) Rectified voltage of secondary after preload circuit, (h) primary current of transformer on real time simulator

Therefore, it is required to consider the nonlinearity behavior of transformer and more precisely during transient state.

1.4.4 Proton exchange membrane fuel cell

One of the most promising sources of renewable energy is fuel cell. It is often presented as a green power source due to the low emission of oxides of nitrogen and sulfur and having low level of noise. Proton exchange membrane fuel cell (PEM fuel cell) has more benefits compared to other types of fuel cell. This is due to its low temperature, high energy density and zero emission. It is also considered to run with pure hydrogen. In order to generate a reliable and efficient power response, it is necessary to have mathematical models for simulation of PEM fuel cells, stacks, and their associated power systems. As a first step of modelling and simulation, it is required to have the characteristics of the real fuel cell obtained with experimental results. In ALSTOM, these measurements were realized on a PEM fuel cell embedded on a train. Figure 1-12 (a) shows the behavior of fuel cell output voltage as a function of current demanded. Based on this figure, it is observed that there is nonlinearity in the characteristics of the fuel cell which should be considered on modelling to have correct value of output voltage on real time simulator. However, as shown in Figure 1-12 (b), this nonlinearity is not considered on electrical model of fuel cell at the beginning of the work.

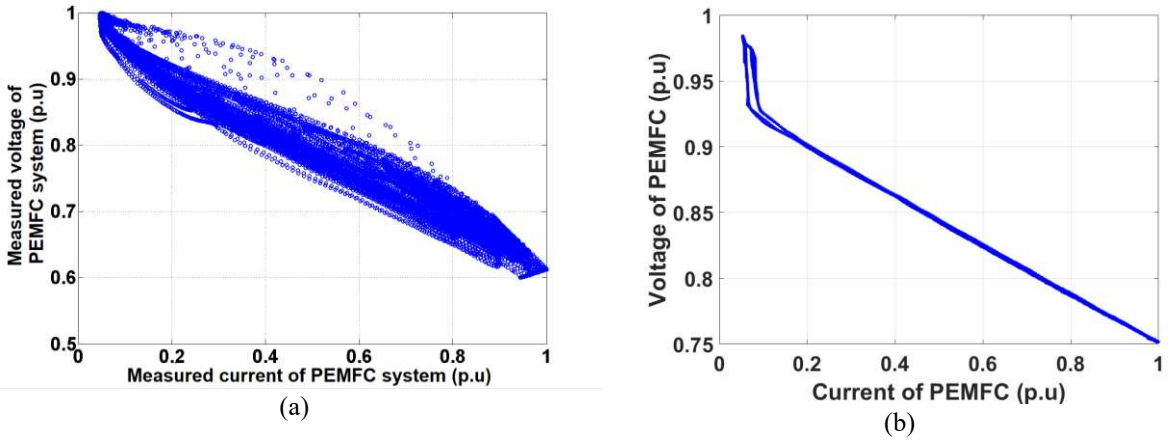

(a) (b)

Figure 1-12 (a) Characteristics of fuel cell on train (b) on real time simulator

In chapter 2, the static and dynamic model of PEM fuel cell is presented in detail.

Once the limitations of traction subsystems are detected, it is required to improve these models in order to achieve the target accuracy. Based on the industrial criteria, less than 5% relative error between simulation and measurements are acceptable. Therefore, to achieve this accuracy in the following chapters, it is aimed to develop the old model by considering the nonlinear parameters of subsystems.

1.5 Conclusion

Due to the several difficulties in the process of validation and certification on train or test bench such as risk of danger, unavailability, high price and so on, it is necessary to use an alternative tool to reduce the number of tests made on real systems. Real time simulators would be the best choice for validation, and verification of the system if the virtual models of whole system are implemented especially by considering the nonlinearity and physical phenomena. The aim of this thesis is to detect the limitation of models embedded into the real time simulator of the company, then develop these models using a methodology that permit to consider physical phenomena and lead to equations than can be solved on real time simulator. Based on the comparison of the results from measurements (train and test bench) with the ones on simulator, it is observed that different nonlinear parameters were not considered on subsystems such as asynchronous motor, pantograph bounce phenomena, non-ideal transformer and PEM Fuel cell.

Nevertheless, the different phenomena to take into account implies several fields of physics. It appears to our knowledge that it would be benefit for the company to get a common framework for the modeling. To propose new models, it is required to select a methodology in which express the model and physical phenomena using state equations and propose the links between differential equations. In next chapter, it is explained the definitions of all these four models in detail and proposed a methodology which permit us to have global state equations considering energy transfer liens between the components of each model. By improving the initial model of subsystems, it is aimed to achieve the accuracy of 5% between simulation and measurements.

Chapter 2

Model proposition for traction system components

2.1 Introduction

In the previous chapter, by comparing the measurements on electrical components of traction system with the results on real time simulator, it was obtained that the model of ASM, pantograph bounce, transformer and proton exchange membrane fuel cell have to be improved. In this chapter, it is aimed to improve the initial model for these components which can be applied on real time simulator. To improve the target accuracy to respect the industrial criteria, it is needed to consider the nonlinear parameters in the subsystem. These nonlinear elements correspond to physical phenomena which exist on experimental condition.

To propose a new model for mentioned components of traction system, it is required to have a modelling method that illustrates the relation between the nonlinear physical phenomena and other electrical elements of electrical circuit. It is expected that the selected modelling method permits us to obtain the state equations considering energy variables between several elements of mentioned components. Then, these state equations have to be solved using numerical method.

As a recent modelling method, there is also the graphical methodology or formalism which takes into account the energy variables. A formalism is a set of symbols used systematically in the construction of mathematical theories. This graphical methodology has to have a complete interpretation energy transfer in the whole system by respecting the principle of causality. Physical causality has integral definitions because it unites the cause to the effect (the effect is always obtained after cause). The causality definition highlights the fact that the energy can not be discontinued. It is also needed to take into account energy nodes that represent the coupling between different elements of desired components.

Based on previous literature [23] there are several graphical methodologies to model a system such as bond graph, causal information graph, energetic macroscopic representation [24]. In this thesis, bond graph methodology is selected as a systematic and common way to represent the power flow between the models of components. This representation permits us to create the state equations of whole desired system considering physical phenomena [25], [26].

In this chapter, the definitions and the required rules of bond graph methodology are explained in section 2.2. Then, the model of ASM, pantograph bounce, transformer and PEM fuel cell are developed in sections 2.3.1, 2.3.2, 2.3.3 and 2.3.4 respectively. The state equations are obtained based on bond graph considering nonlinear elements in the circuit.

2.2 Bond graph

Bond graph method is proposed in 1960 and it is improved in the years of 1970. At the end of 70s, this method was used in Europe and in France as well [27]. It is used regularly in different companies particularly the automobile industry such as PSA, Renault, Ford, Toyota, etc. This method represents the energy transfer using power links which are shown by a half-arrow. Therefore, the orientation of the half-arrow shows the direction of power transfer. Each

half arrow represents the variable of flow (*f*) and effort (*e*) which product the power. Figure 2-1 represents the power transfer between two simple systems:

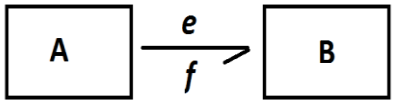

Figure 2-1 Power transfer between two subsystems using Bond Graph

There are also two other variables in bond graph method: the momentum *p*, the displacement *q* which are the integral of the effort and flow respectively. These variables have different definitions based on each kind of physical domains. These definitions are explained in Table 2-1.

Table 2-1 Equivalent variables of bond graph in different physical domain

Domain	**Effort** ***e***	**Flow** ***f***	**Momentum** ***p***	**Displacement** ***q***
Electrical	Voltage *V*	Current *I*	Magnetic flux ∅	Load *q*
Mechanical Translation	Force *F*	Speed *v*	Impulsion *p*	Displacement *x*
Mechanical Rotation	Torque *T*	Angular speed *ω*	Angular impulsion *h*	Angle *θ*
Thermodynamic	Temperature	Flow of entropy		Entropy
Magnetic	Magnetomotive force	Derivative magnetic flux	-	Magnetic Flux

2.2.1 The elements of Bond graph

There are two types of elements on bond graph: active and passive elements. The active elements are the source of effort or flow which can have independent value from all the external influences. The symbols of active elements are S_e for source of effort and S_f for source of flow.

Figure 2-2 which is called Paynter tetrahedron, illustrate the mathematical relations between the general variable of bond graph and passive elements (*R, I, C*) [27].

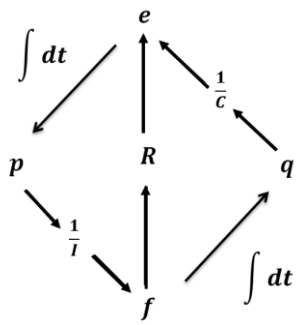

Figure 2-2 Paynter tetrahedron

R, *I*, *C* represent the dissipated energy, kinetic energy, potential energy respectively. These passive elements illustrate resistance, pure inductance and pure capacitor respectively in

electrical domain. As an example, figure 2-2 shows that the flow (f) which represents the current in electrical domain multiply by dissipated energy (R) which represent the resistance provides effort (e) which represent the voltage. In order to split the bond graph elements, there are four different junctions as Table 2-2.

Table 2-2 Bond graph junctions

Junctions	Definitions
1	It behaves such that all flow values are equal across the bonds.
0	It behaves such that all effort values are equal across the bonds.
TF	It behaves as a transformer (there is a relationship between flow in and flow out)
GY	It behaves as a Gyrator (there is a relationship between flow in and effort out)

2.2.2 Causalities in Bond graph

The bond graph methodology not only represents the power transfer in the system, but also it takes into account the integral causalities between different elements of system. The causalities in bond graph indicate which side of a bond determines the instantaneous effort, and which determines the instantaneous flow [28]. The causalities can define the independency and dependency of each element in the dynamic systems. By propagating the causation graphically from one modeling element to the other, the analysis of large-scale model will become easier.

In bond graph notation, a causal stroke can be added to one end of the power link to indicate that the opposite end is defining the effort. Obviously, the only one end of a power link can define the effort and so only one end of a bond can have a causal stroke. Therefore, the causality orientations of *C* and *I* components that define the effort and the flow respectively, are presented below.

$$\boldsymbol{Junction} \longmapsto \boldsymbol{C} \qquad\qquad \boldsymbol{Junction} \longrightarrow\!\!| \boldsymbol{I}$$

The corresponding equations of these passive components would be as below considering the Paynter tetrahedron state.

$$e(t) = \frac{1}{C}\int f(t)\,dt \qquad\qquad f(t) = \frac{1}{I}\int e(t)\,dt$$

The component *R* which does not have dependency of time can apply a voltage and get a flow or inversely.

$$\boldsymbol{Junction} \longrightarrow\!\!| \boldsymbol{R} \qquad \text{Or} \qquad \boldsymbol{Junction} \longmapsto \boldsymbol{R}$$

The transformers (*TF*) do not dissipate or store the energy so the causality can pass through them. The gyrators transform the flow to the effort and inverse. So, if the flow causes one side, the effort will cause on the other side. Figure 2-3 shows the causal orientations for transformer and gyrator.

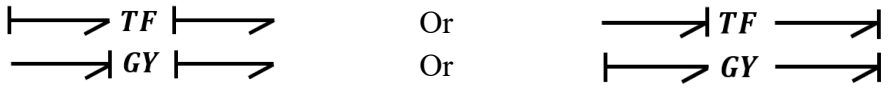

Figure 2-3 The causality of transformer and gyrator

In the points that we have junctions, it has to be considered that 0-junction has one causality and 1-junction has one power bond as shown in figure 2-4.

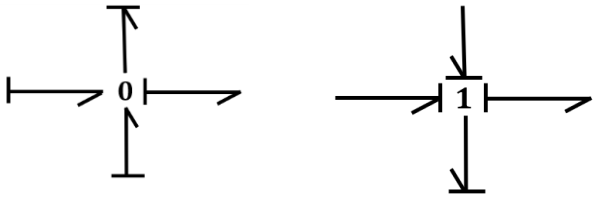

Figure 2-4 The causality of 0-junction and 1-junction

2.2.3 The causal path, causal loop and action chain

A path between an element of the set $J_1 = \{C, I, R, S_e, S_f\}$ and an element of the set $J_2 = \{C, I, R, S_e, S_f\}$ is a chain of intercalated bonds, junctions and elements such that a complete and correct causality is given to all the sequence called causal path. The causal path which passes through one element to another just by traversing the junctions is a direct path. If the variables are the same, the corresponding path is called simple causal path. In the presence of an element like gyrator that changes the variable, causal path is called mix. In the case of having passive elements (*R*, *C* and *I*), causal path is called indirect [27].
Causal loop is a closed path loop between a set of elements such as (*C*, *I*, *R*). The causal path has to start from one element and at the end it returns to the same element without passing any bond more than once. An action chain is a causal path between a source and output.

2.2.4 Analysis of a dynamic system with Bond graph

Based on the explanations in last paragraphs, an electrical circuit like in figure 2-5 is considered to do the analysis based on its bond graph. This circuit consists of a voltage source, an inductance, a capacitor and a resistance. Based on the methodology of bond graph, the tranfered energy and causalities are shown in figure 2-6. As it is shown in figure 2-6, there is a voltage source that excite the storage elements in the circuit. Based on the definitions of bond graph, there are two passive elements (*I* and *C*) in the circuit which impose the flow and effort respectively. The flow of inductor is the current $i(t)$ and the effort of capacitor is $e_c(t)$. Based on the links between source and storage elements, it can be obtained that there is a direct causal path between voltage source and element passive (*I*), an indirect causal path between source and elements $J_1 = [I, 1, 0, C]$, and a causal loop between passive elements (*C, I, R*).

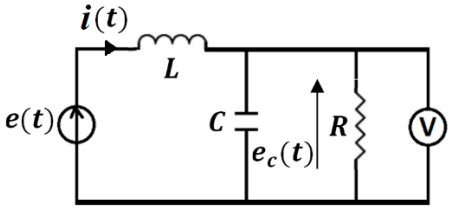

Figure 2-5 An Example of Electrical circuit

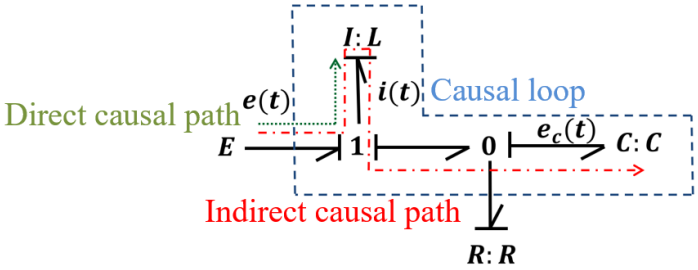

Figure 2-6 The bond graph of electrical circuit shown in figure 2-5

Based on the causalities on the bond graph, the state equations can be obtained considering state variables. The state variables based on energy variables are $i(t)$ for I element and $e_c(t)$ for C element. Here are the state equations:

$$\begin{bmatrix} i'(t) \\ e_c'(t) \end{bmatrix} = \begin{bmatrix} 0 & -\frac{1}{L} \\ \frac{1}{C} & -\frac{1}{CR} \end{bmatrix} \begin{bmatrix} i(t) \\ e_c(t) \end{bmatrix} + \begin{bmatrix} \frac{1}{L} \\ 0 \end{bmatrix} [e(t)] \tag{2.1}$$

Note that the matrix representation of state equations can be used assuming that the equations are linear. In the following, all the desired parts of traction system are improved based on the methodology of bond graph.

2.3 Proposition of models

Based on the bond graph rules and definitions, the macro model of railway traction system considered in this thesis is illustrated in figure 2-7.

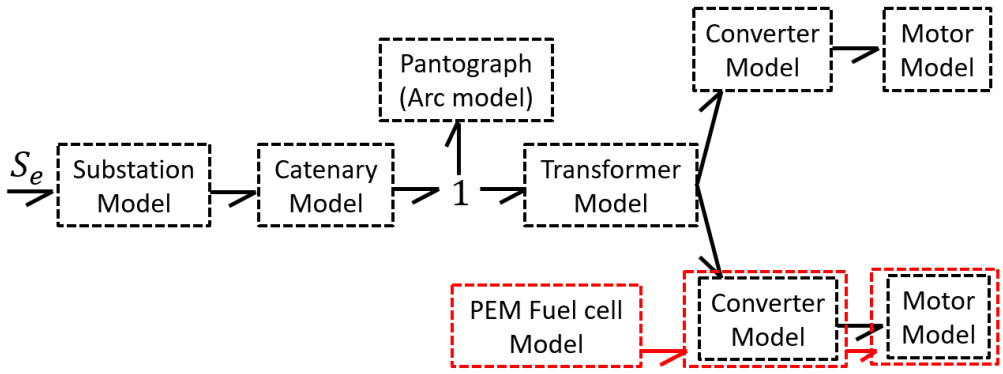

Figure 2-7 Traction system bond graph

In this figure, two type of traction system used in this thesis are presented: a traction system with substation voltage and catenary shown in black, a traction system fed by PEM fuel cell shown in red. The corresponding causalities of figure 2-7 are completed by representing the bond graph of component in each section. The mentioned components of traction system explained in chapter 1 are considered to develop based on their limitations in this chapter. The corresponding nonlinear parameters are considered based on the comparisons done in chapter 1. The limitations and definitions about the nonlinear parameters of ASM, pantograph bounce, transformer and fuel cell are explained in parts 2.3.1.1, 2.3.2.1, 2.3.3.1 and 2.3.4.1 respectively. Then, the propositions for each model are proposed. All the models are presented based on energy links using bond graph. All state equations achieved by the bond graph analysis are provided. Then, equations are proposed for modelling nonlinear physical phenomena in each component. The models of converters are out of scope of this thesis and it is not presented.

2.3.1 Asynchronous motor

2.3.1.1 Definitions

The equivalent circuit model of ASM and corresponding lumped parameters have been widely used in motor designs and real time modelling of motor drive systems. The basic and initial implemented model of ASM on simulator is shown in figure 2-8.

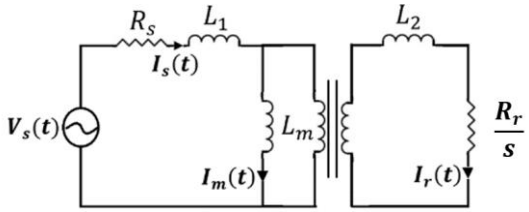

Figure 2-8 Electrical model of asynchronous motor

The model of ASM in figure 2-8 is a known electrical model in power electronic where V_s, R_s, R_r, L_1, L_2 and L_m are stator voltage (phase to neutral), stator resistance, rotor resistance, stator leakage inductance, rotor leakage inductance and magnetizing inductance, respectively. Slip, s, is defined as the difference between stator field (synchronous) and the rotor speed. As explained in last section, the state equation corresponding to the electrical circuit can be easily obtained using bond graph method. Before proposing the bond graph of ASM, it is needed to simplify the system and consider the rotor elements as the point of view of stator. Therefore, some transformations are required to be applied on electrical system of motor.

First, to simplify the analysis and equations, Clarke transformation (α, β) is applied to three phase $(a, b$ and $c)$ voltages and currents of desired asynchronous motor (Appendix A.1 (eq. A.1.1)). The basic electrical equations of ASM (figure 2-8) are proposed in Appendix A.1 (eq. A.1.3) - eq. (A.1.10). Note that rotor speed is considered as $\omega(t) = P_p\Omega(t)$ where P_p is number of pairs. The voltage of rotor is zero because it is short circuit.

It is possible to transfer the rotor elements to stator part by changing the parameters of electrical circuit. Figure 2-9 shows the electrical circuit of asynchronous motor by transferred rotor to stator part in (α, β) axles.

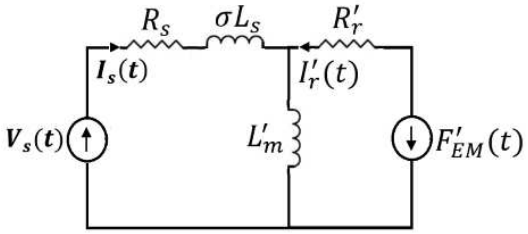

Figure 2-9 Electrical model of asynchronous motor in (α, β) axles with transferred rotor in stator part

where σ is the magnetic leakage coefficient, R'_r is the transferred rotor resistance to stator part, L'_m is the magnetizing inductance considering the rotor effect, $F'_{EM}(t)$, $I'_r(t)$ are the electromagnetic force and rotor current which are transferred to stator part. Equations (A.1.11) – (A.1.16) in Appendix A.1 shows the equivalent expression for each element, current and flux of rotor in figure 2-9 [29].

As ASM is an electrical and mechanical system therefore the definitions such as inertia J_{ASM}, friction f_{meca} and torque T have be considered. The relation between the mechanical part of motor which transfers the electromotive force to the electromagnetic torque can be defined by rotor flux and stator current (Appendix A.1 equation (A.1.17)) [29].

As explained in chapter 1, the correct machine parameters are essential to produce desired drive performance especially in vector control systems where electromagnetic states of the motor are estimated and controlled by using measurements and lumped parameters. However, due to several effects, lumped parameters of ASM are changed by different load conditions. Therefore, these parameters should be evaluated at different load conditions in order to get reliable results compare to experiments.

ASM are usually designed to be magnetically saturated in the operating point. The most important and dominating parameter of motor is magnetizing inductance which vary largely during different load condition. Thus, it must be evaluated during the operation of motor under different load condition [30].

Many researches has been done to evaluate magnetizing inductance of an induction motor as a function of magnetizing current [31] and [32]. The dependency of magnetizing inductance on torque has been discussed in [30]. In [33] and [34], it is discussed about the dependency of magnetizing inductance on slip frequency. However, as the bond graph methodology is selected in this thesis, it is desired to evaluate the magnetizing inductance function based on state variables. In section 2.3.1.3, it is discussed in detail.

All the parameters and physical model of asynchronous motor expressed in Appendix A.1, will be used to create its bond graph and then calculate the state equations. All the explanations corresponding to the bond graph of motor are proposed in next part.

2.3.1.2 Bond graph of asynchronous motor

As it is shown in last part, figure 2-9 depicts electrical schematic corresponding to each phase of ASM. Based on the bond graph laws, 1-junction can connect the voltage source to leakage inductance and resistance of stator. 0-junction is also needed to make a connection between L'_m and the two other branches. Based on Paynter tetrahedron, the derivation of momentum will be an effort in which in the case of electrical domain is magnetic flux. Therefore, the derivate of rotor flux transferred to stator part ($\dot{\phi}'_r(t)$) will produce the effort on 0-junction. The relation between electrical part and mechanical part can be depicted by a gyrator with a command signal (MGY). The command signal for gyrator can be obtained by the integral of the voltage on 0-junction multiplied by number of pairs P_p. Figure 2-10 depicts the bond graph of asynchronous motor for two axles of (α, β).

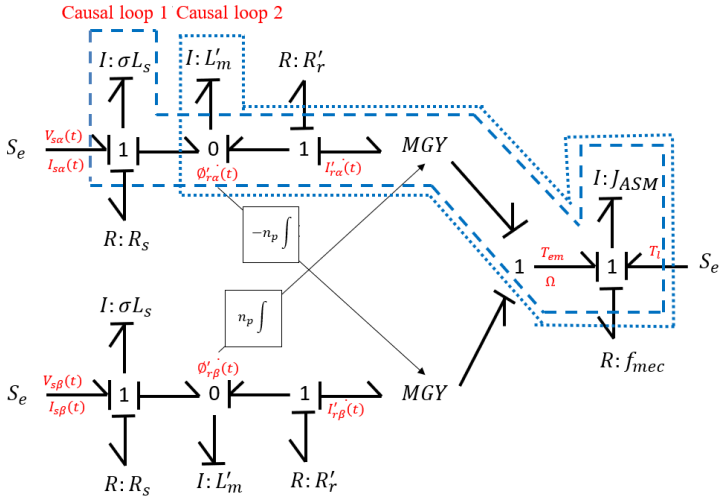

Figure 2-10 The complete bond graph of asynchronous motor in two axles of (α, β)

As state variables are the flow, effort and their deviations in bond graph methodology, five state variables such as stator current as flow, derivate of rotor flux as effort in (α, β) axles and angular speed of rotor as flow are detected. Two causal loops are shown in figure 2-10. These two causal loops link the inductance of inertia to two storage elements of ASM which are stator and magnetizing inductance.

Based on the bond graph and causalities, it can be concluded that input of the system is a voltage and the output is a current. Therefore, the causality in the motor model in the overall traction system is as figure 2-11.

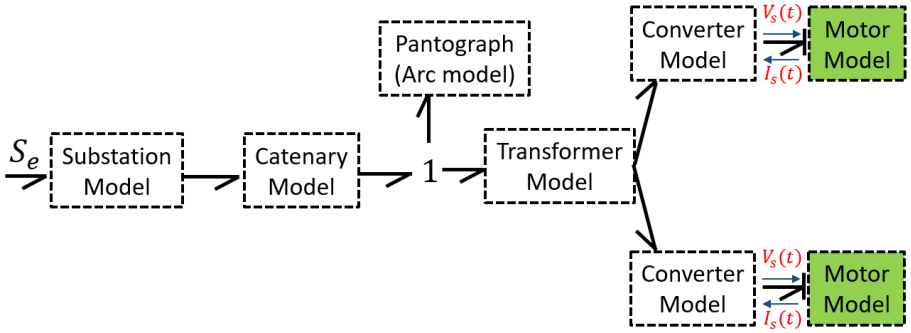

Figure 2-11Traction system bond graph considering the causality of ASM

As the ASM causalities are defined, it is shown in green in figure 2-11. In next part, the state equations of whole system can be easily achieved by the analysis done using bond graph.

2.3.1.3 State equation of asynchronous motor

In order to explain the causalities in the electrical system of ASM, the state equations considering the inputs and the state variables are selected. The state model of the whole system will be presented in two axes of Concordia; the same as its bond graph model. Based on the parameters on bond graph of the system, it can be observed that there are five state equations in the system ($I_{s\alpha}(t), I_{s\beta}\ (t), \emptyset_{r\alpha}(t), \emptyset_{r\beta}(t)$ and $\Omega(t)$). The input and output of the system are stator voltages which come from the output of the inverter in traction chain and the stator currents, respectively. Using the equations (A.1.3) – (A.1.10) in Appendix A.1, five state equations of ASM can be obtained as below:

$$\dot{I}_{s\alpha}(t) = \left(\frac{-1}{\sigma T_s} - \frac{1-\sigma}{\sigma T_r}\right) I_{s\alpha}(t) + \frac{1-\sigma}{\sigma L_m T_r}\emptyset_{r\alpha}(t) + \frac{1-\sigma}{\sigma L_m}\omega(t)\emptyset_{r\beta}(t) + \frac{1}{\sigma L_s}V_{s\alpha}(t) \tag{2.2}$$

$$\dot{I}_{s\beta}(t) = \left(\frac{-1}{\sigma T_s} - \frac{1-\sigma}{\sigma T_r}\right) I_{s\beta}(t) - \frac{1-\sigma}{\sigma L_m}\emptyset_{r\alpha}(t) + \frac{1-\sigma}{\sigma L_m T_r}\omega(t)\emptyset_{r\beta}(t) + \frac{1}{\sigma L_s}V_{s\beta}(t) \tag{2.3}$$

$$\dot{\emptyset}_{r\alpha}(t) = \frac{L_m}{T_r} I_{s\alpha}(t) - \frac{1}{T_r}\emptyset_{r\alpha}(t) - \omega(t)\emptyset_{r\beta}(t) \tag{2.4}$$

$$\dot{\emptyset}_{r\beta}(t) = \frac{L_m}{T_r} I_{s\beta}(t) + \omega(t)\emptyset_{r\alpha}(t) - \frac{1}{T_r}\emptyset_{r\beta}(t) \tag{2.5}$$

where $T_s = \frac{L_s}{R_s}$ and $T_r = \frac{L_r}{R_r}$ are time constant of stator and rotor respectively and $\omega(t) = P_p\Omega(t)$ is electrical angular speed of rotor which can be obtained using state equation in mechanical part. In mechanical part of asynchronous motor shown in figure 2-10, the state equation is as below:

$$\dot{\Omega}(t) = \frac{1}{J_{ASM}}(T_{em} - f_{mec}\Omega(t) - T_l) \tag{2.6}$$

where $\Omega(t)$ is angular speed of rotor, J_{ASM} is combined rotor and load inertia constant which is set to infinite to simulate locked rotor and f_{mec} is combined rotor and load viscous friction coefficient. T_{em} and T_l are electromagnetic and load torque.

As it is discussed previously, to have more accurate results compared to experiment, it is required to consider the variation of circuit parameter due to several impacts in the system. Magnetizing inductance is one of the important circuit parameters that changes by variation of flux which makes its characteristics to be nonlinear. Let us remind that this parameter was considered as constant parameter in the beginning of thesis. To consider its nonlinear characteristic proposed by the providers in the datasheet of ASM, it is required to have an equation which represents the magnetizing inductance variation as a function of state variables. In next paragraphs, the equations considered for magnetizing inductance is explained in detail.

2.3.1.4 Nonlinear magnetizing inductance

Depending on the type and performance of windings and parameters of magnetic circuits in ASM, its electrical properties can be determined. The magnetic circuits of ASM is made of ferromagnetic materials. As it is explained in chapter 1, the ferromagnetic materials have nonlinear characteristics including saturation and hysteresis phenomena. To conclude whether the given ferromagnetic material has linear or nonlinear behavior, it is required to have the magnetization characteristic which is known by $B-H$ curve. This characteristic can be obtained using the measurements or on magnetic flux and magnetizing current of motor Finite Element method (FEM) simulation.

Based on the datasheet of ASM in our case, the characteristic of magnetizing current is provided based on rotor flux based on simulation. Figure 2-12 presents the magnetizing current, rotor flux and the variation of magnetizing inductance as a function of rotor flux.

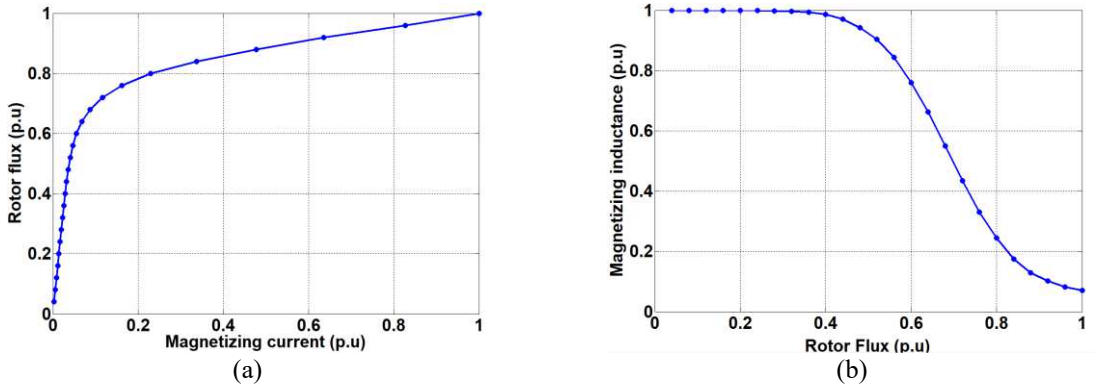

(a) (b)

Figure 2-12 The datasheet information of ASM (a) rotor flux vs magnetizing current (b) magnetizing inductance vs rotor flux

The relation between rotor flux and magnetizing current provides the magnetizing inductance value (equation A.1.19 in Appendix A.1). The corresponding equation is obtained using curve fitting. Equation (2.7) is a polynomial equation that provides the value of magnetizing current as a function of rotor flux.

$$I_{m_{p.u}}(\emptyset_{r_{p.u}}) = \left(\frac{1}{c}\right)\left(a\emptyset_{r_{p.u}} + (1-a)\emptyset_{r_{p.u}}{}^{b}\right) \tag{2.7}$$

where *a, b* and *c* are constant coefficient which perform the shape of nonlinear magnetizing inductance curve as a function of rotor flux. Note that all the elements are in per unit ($\emptyset_{r_{p.u}} = \frac{|\emptyset_r|}{\emptyset_{r_{nominal}}}$). By considering relation between magnetizing current and rotor flux, magnetizing inductance can be obtained for each value of rotor flux as (2.8).

$$L_m(\emptyset_{r_{p.u}}) = \frac{\emptyset_{r_{p.u}}}{\left(\frac{1}{c}\right)\left(a\emptyset_{r_{p.u}} + (1-a)\emptyset_{r_{p.u}}{}^{b}\right)} \tag{2.8}$$

a, b and c are different for each kind of ASM. Therefore, it is needed to identify these parameters based on experimental data mentioned in datasheet or obtained experimentally. In next chapter, all the procedure of identification is explained in detail.

Let us remark that the value of magnetizing inductance is calculated in quasi-static time step and we use the incremental value of magnetizing inductance during the simulation. This means that there is no specific nonlinear function like $\emptyset_m = g_m(I)$ for magnetizing inductance characteristics in our case. However, the corresponding value of magnetizing inductance is calculated for every value of current in each time step (like a look up table). The block diagram in figure 2-13 represents aforementioned to calculate L_m.

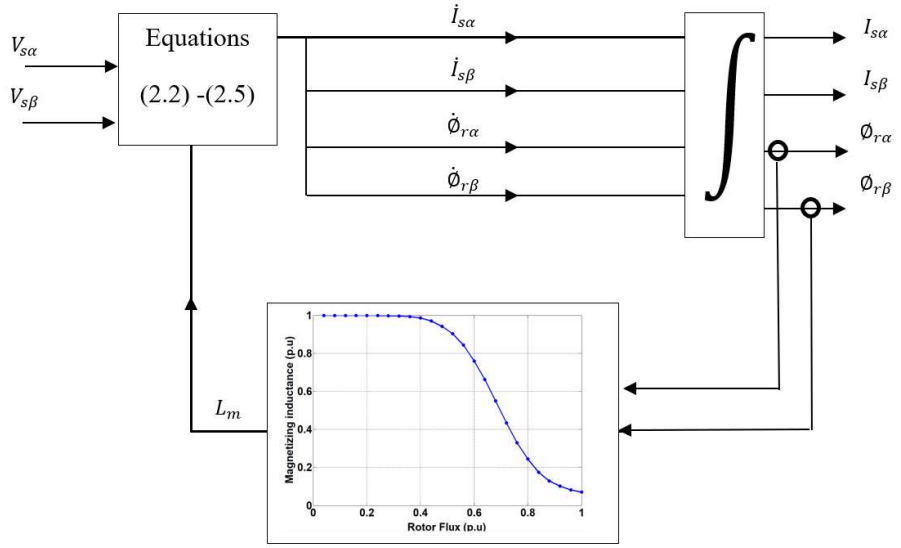

Figure 2-13 The block diagram of the incremental magnetizing calculation in this thesis

This process is applied in the dynamic simulation in chapter 3 and 4.

2.3.2 Pantograph bounce

2.3.2.1 Definitions

In recent years, high-speed trains become more popular due to its low-cost, safety, large compacity to carry the heavy loads, eco-friendly etc. The high speed for electrified railway becomes more important and development trend along with the safety and reliability of railway transport in which the operational speed of high-speed trains has been exceeded until 300 km/h in some countries.

In certain electrified railway applications, trains collect the current through the sliding electrical contact between pantograph strip and catenary. Therefore, the quality of voltage affects directly the operational properties of train. There are different phenomena that can have an impact on catenary voltage and current. One of these frequent phenomena is pantograph bounce which appears due to the pantograph-catenary disconnection. The disconnection between catenary and pantograph can happen due to the irregularity of the contact wire, mechanical oscillation of running high speed train and neutral section etc. [35]. Figure 2-14 depicts this phenomenon on train.



Figure 2-14 Pantograph arcing phenomenon (based on internal confidential Alstom archive)

The undesirable distance created between pantograph and catenary causes electrical arc which distorts the sinusoidal waveform, generates a net dc component, harmonics (including even harmonics and inter-harmonic), generates the transients cause high-frequency conducted and radiated electromagnetic interference and discontinuous current flowing through the locomotive equipment [36]-[39]. The discontinuous current will deteriorate the quality of power supply significantly as well. This effect can be aggravated by rising the train speed and the arc time lasting [40]. The validation process of input power chain in the case of having electrical arc is dangerous and risky. Therefore, it is necessary to use the simulation models for such kind of test.

Many previous investigations were done on the effect of electrical arc on voltage and current. The electrical arc created on AC pantograph distorts the current waveform and it generates the transient effects during the current zero crossing (CZCs) on voltage [41]-[43]. To define the effect of arc phenomena, it is required to characterize the CZCs region. In [44] and [45], the CZCs regions are determined using Mayr's equation. Moreover, the power of traction in high-speed and heavy-load trains is increasingly larger. As a result, the traction current to catenary is larger [46]. Many investigations were done corresponding to pantograph arcing tests and current collection [41]- [43] and [47]. It is determined that in train applications with high current and low resistance state before CZCs, the initial Mayr arc model is not suitable enough. Then,

the Cassie equation is proposed which is more accurate for describing the electrical arc characteristics [48]. The Hebdank's equation considers two different pantograph arc behavior of high and low current of catenary [49].

In initial model of pantograph bounce on our simulator system, arc phenomenon is considered as a constant resistance which was not representative enough as it is shown in the comparison results in chapter 1. Moreover, in order to analyze the global influence of pantograph bounce and electrical arcing, it is needed to have a complete model of input power chain including substation, catenary and transformer.

There are several approaches which proposed arc model inside circuits [41], [50] and [51] . However, the results obtained in laboratory scale which are not exactly representative for this phenomenon on complete traction system. In this thesis, alternating current power chain including pantograph bounce effects is modeled considering the bond graph methodology to ensure the overall consistency of the simulation. The state equations of the system are deduced for simulation purposes. In order to validate the proposed model, simulation results are given and compared with train measurements in chapter 4.

In next part, the proposed electrical model including arc model is proposed and the procedure of arc phenomena is explained in detail.

2.3.2.2 Model of input power chain and arc model

2.3.2.2.1 Power part

In this part, power chain from substation source to secondary part of transformer is particularly under concern to have global view of energy transferred in the input system. And the electromechanical part and associated power converters of the traction chain are simplified through equivalent voltage sources based on experimental steady state measurements (U_{s_1},U_{s_2}). The corresponding traction system schematic is depicted in figure 2-15. The transformer is considered as a linear one to predict its characteristics. There are two windings in the secondary which are associated to traction chains rectifiers. The variation of resistance, inductance and capacitor of catenary π model due to the distance between train and substation is considered in electrical model. Note that these parameters may also depend on environmental conditions such as temperature and humidity. However, these effects will not be studied in this thesis. Only general values of parameters will be indicated and should be adapted. As described in [52], electrical arc can be modelled as a nonlinear resistance. This variable resistance (R_{arc}) represents the connection or disconnection of pantograph and catenary including arcing phenomenon.

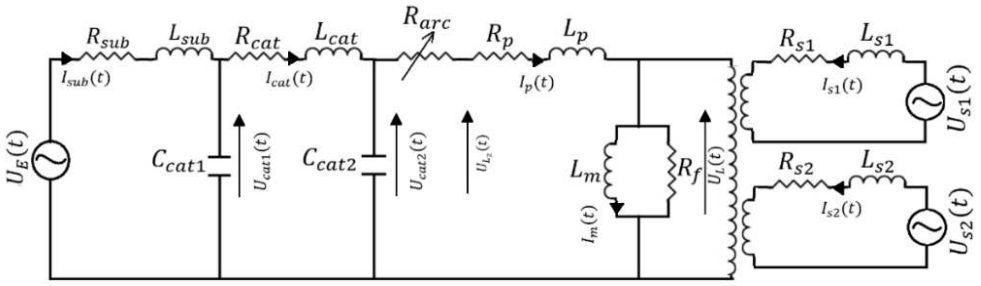

Figure 2-15 Power supply, catenary and traction system including arc resistance

Figure 2-15 depicts our desired single-phase transformer with resistance and inductance leakage in primary winding (R_p, L_p) and R_f, L_m in the shunt branch represent the core behavior. For simplicity, magnetizing inductance L_m considered as a constant parameter in this model. R_{sub} and L_{sub} represent resistance and inductance of substation respectively. The equivalent catenary π model is consisted of resistance, capacitors and inductance (R_{cat}, C_{cat_1}, C_{cat_2} and L_{cat}). R_{s_1}, L_{s_1}, R_{s_2} and L_{s_2} represent leakage resistance and inductance of two windings in secondary part respectively.

Now, it is needed to consider the nonlinear model of arc.

2.3.2.2.2 Pantograph bounce process

The pantograph detachment is a dynamic phenomenon and it is mostly due to the hard points existing on contact wire [53]. As [54], the moving of train in oscillator manner excite the vibration of a bean which causes the pantograph detachment. Generally, there are four different conditions during the pantograph bounce [50]; No arc, arc drawn, arc extinguished and arc approach as depicted in figure 2-16. Under common trend of trajectory, the trajectory will be influenced by the factors of changing train speed, specific mechanical oscillation of train, airflow strong, irregularity degree of the contact wire, etc. [52]. Therefore, some conditions (No arc, arc drawn, arc extinguished and arc approach) may not happen due to the different case of disconnection. Figure 2-16 shows the general procedure of pantograph bounce.

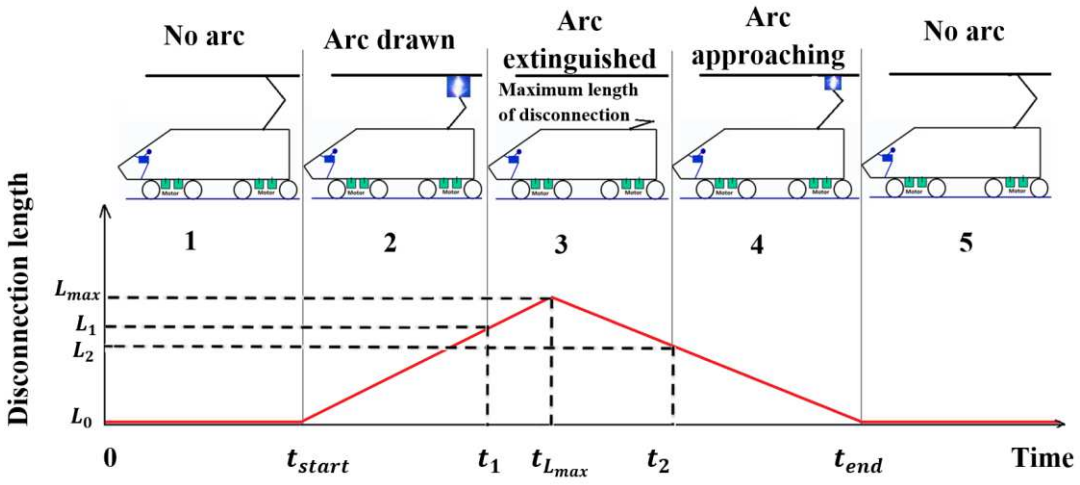

Figure 2-16 Pantograph bounce total process

As it is shown in figure 2-16, the moment that there is no disconnection (no arc) between pantograph and catenary (region 1 and 5). Once the pantograph started to be disconnected from catenary, the electrical field in the air gap will creates an electrical arc. As the electrical arc behaves like a nonlinear resistance, the electrical current is already flowing with some reduction. And due to the nonlinear variation of arc resistance, the waveform of voltage begins to be deviated from sinusoidal form. When the pantograph continues to increase the disconnection length, the arc does not have enough energy to exist (arc drawn). Once the electrical arc is disappeared, there is not any connection between catenary and pantograph (arc extinguished). In region 4, the pantograph begins to come back to the catenary and the arc phenomena will appear due to the created electrical field between the pantograph and catenary (arc approaching). In drawn arc condition, the arc will continue to maintain its channel once established. It is obvious to have much longer distance in drawn arc condition in comparison of the region of arc approaching. Another reason is that the ignition of the arc in drawn arc results from combination of thermal ionization and field emission, while only field emission is responsible for the initial breakdown of air gap in the condition of approaching arc.

To have a model of detachment variation in time, it is required to consider speed of train, time interval and maximum detachment length. In this thesis, it is considered that the disconnection length increases by time with ramp function [52]. Assuming the start point of detachment, maximum detachment and reconnection point of pantograph and catenary are $t_{start}, t_{L_{max}}, t_{end}$ respectively. t_1 and t_2 are respectively the time that arc distinguished region is started and ended. The total equation is presented in Appendix A.2 (eq. A.2.1):

In some trajectory, it is possible to not have the arc extinguished region (Figure 2-17) which means there is always the electrical connection by electrical arc during the pantograph bounce, $t_2 = t_1 = t_{L_{max}}$ and $L_1 = L_2 = L_{max}$ (equation (A.2.2) in Appendix A.2).

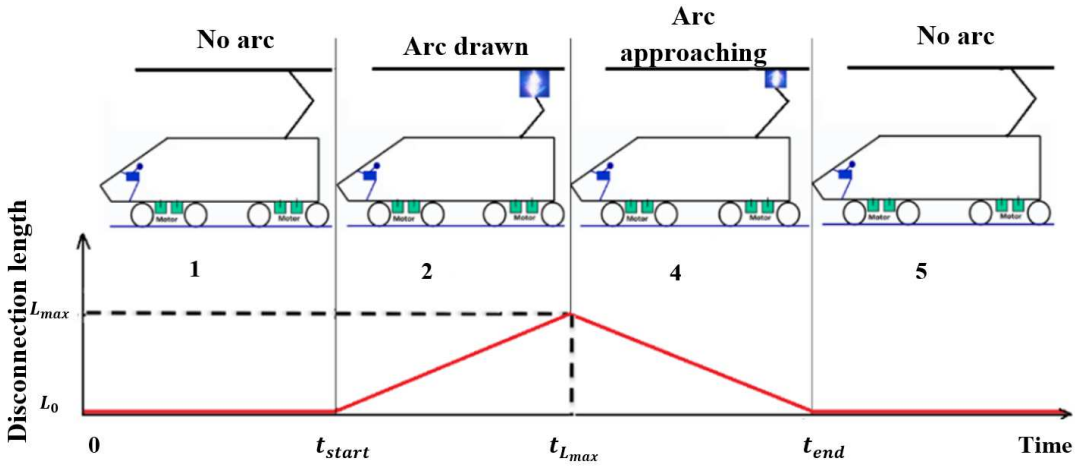

Figure 2-17 Pantograph bounce total process without arc extinguished step

In next part, the bond graph of whole system including arc model is described in detail.

2.3.2.3 Bond graph of input power chain including arc

In order to have a complete model of power chain, the bond graph directly allows us to identify not only the inputs of the system but also state variables. Electrical schematic of power chain is shown in figure 2-15. Based on bond graph definitions and laws, substation source can be connected to its impedances by 1-junction. π model of catenary is needed to be connected to substation circuit and primary of transformer by two 0-junctions. In the primary part of transformer, R_p, L_p and R_{arc} have the equal current which must be connected by 1-junction. To illustrate the transferred flow (current) and effort (voltage), TF element is chosen. Electromechanical part and associated power converters of the traction chain simplified through equivalent voltage sources must be connected to the secondary of transformer using 1-junctions. Figure 2-18 shows the bond graph of power chain with state variables and voltage sources.

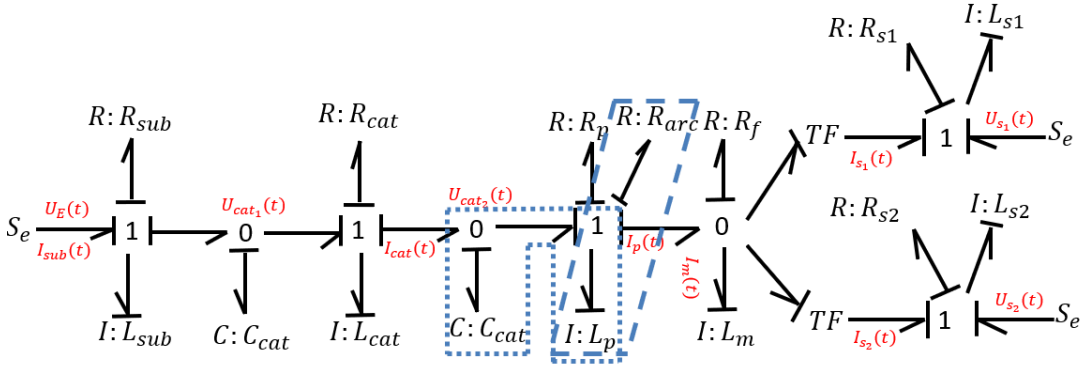

Figure 2-18 The bond graph of input power chain including state variables shown in red

There is a causal loop between capacitor of catenary and primary leakage inductance of transformer and another causal loop between the resistance of arc and primary inductance of transformer. Based on the bond graph of detail model of input power chain, it can be deduced that substation, catenary and arc model in pantograph get the flow and apply an effort on overall system. It is depicted in the bond graph of traction system as figure 2-19.

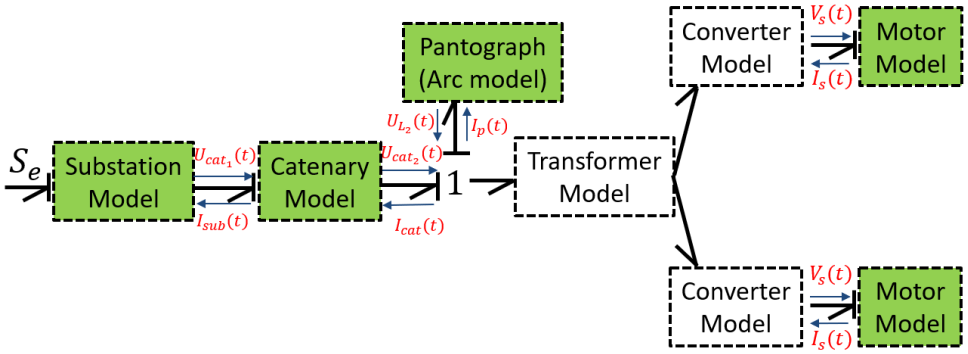

Figure 2-19 Traction system including the causalities of substation, catenary, arc model and ASM model

As the causalities of the substation, catenary, electrical arc models are identified, they are shown in green in figure 2-19. In the next part, state equations of whole power chain considering arc

phenomenon is presented using the energy transferring links in the bond graph of system shown in figure 2-18.

2.3.2.4 State equations

Following junction equations presented in section 2.2, state equations of the whole system can be directly achieved considering energy variables and causality:

$$\dot{I}_{sub}(t) = \frac{-R_{sub}}{L_{sub}} I_{sub}(t) - \frac{1}{L_{sub}} U_{cat_1}(t) + \frac{1}{L_{sub}} U_E(t) \tag{2.9}$$

$$\dot{I}_{cat}(t) = \frac{-R_{cat}}{L_{cat}} I_{cat}(t) + \frac{1}{L_{cat}} U_{cat_1}(t) - \frac{1}{L_{cat}} U_{cat_2}(t) \tag{2.10}$$

$$\dot{U}_{cat_1}(t) = \frac{1}{C_{cat_1}} I_{sub}(t) - \frac{1}{C_{cat_1}} I_{cat}(t) \tag{2.11}$$

$$\dot{U}_{cat_2}(t) = \frac{1}{C_{cat_2}} I_{cat}(t) - \frac{1}{C_{cat_2}} I_p(t) \tag{2.12}$$

$$\dot{I}_p(t) = \frac{U_{cat_2}(t)}{L_p} - \frac{\left(R_{arc}(t) + R_p\right)}{L_p} I_p(t) - \frac{U_L(t)}{L_p} \tag{2.13}$$

$$\dot{I}_m(t) = \frac{U_L(t)}{L_m} \tag{2.14}$$

$$\dot{I}_{s_1}(t) = \frac{(-R_{s_1} I_{s_1}(\mathrm{t}) + m_1 U_L(\mathrm{t}) - U_{s1}(\mathrm{t}))}{L_{s_1}} \tag{2.15}$$

$$\dot{I}_{s_2}(t) = \frac{(-R_{s_2} I_{s_2}(\mathrm{t}) + m_2 U_L(\mathrm{t}) - U_{s_2}(\mathrm{t}))}{L_{s_2}} \tag{2.16}$$

with,

$$U_L(t) = R_f\left(I_P(t) - m_1 I_{s_1}(t) - m_2 I_{s_2}(t) - I_m(t)\right) \tag{2.17}$$

where m_1 and m_2 are primary to secondary ratios of transformer.

Now, it is needed to have the electrical arc model that behaves like a nonlinear resistance described before. Next section explained it in detail.

2.3.2.5 Nonlinear model of electrical arc

To consider two situations of the current zero crossing (CZCs), high current and low resistance state before CZCs, Habedank's equation-based arc model is selected [48]. The Habedank arc model consists in association of Mayr's model (2.18) and Cassie's model (2.19). Therefore, the arc resistance can be calculated by (2.20).

$$\frac{dg_m(t)}{dt} = \frac{1}{\tau_1}\left[\frac{I_p(t)^2}{P_0(t)} - g_m(t)\right] \tag{2.18}$$

$$\frac{dg_c(t)}{dt} = \frac{1}{\tau_2}\left[\frac{I_p\,(t)^2}{u_c(t)^2 g_c(t)} - g_c(t)\right] \tag{2.19}$$

$$R_{arc}(t) = \frac{1}{g_{arc}(t)} = \frac{1}{g_c(t)} + \frac{1}{g_m(t)} \tag{2.20}$$

where $g_m(t)$, $g_c(t)$, $\tau_1$and τ_2 are arc conductance and time constant in the model of Mayr and Cassie, respectively. $g_{arc}(t)$ is the conductance of the arc model. $P_0(t)$ and $u_c(t)$ are dissipated power and arc voltage gradient time-varying parameters, which depend on the varying pantograph detachment distance.

Based on several analysis concerning pantograph arc characteristics, it is observed that there are five steps for an AC arc from the beginning of arc approach to arc extinguished [53] which are listed below respectively:

- Start burning of arc
- Unstable establishment of arc
- Stable combustion of arc
- Unstable period before arc's extinction
- Arc extinction.

The stable combustion part of the arc almost occupies the whole time of arc approaching level [52]. Therefore, the arc voltage gradient is equal to stable value and it depends on the voltage drop of arc $u_c(t)$ which is only related to arc length $L_{arc}(t)$. There is a constant ratio between $u_c(t)$ and $L_{arc}(t)$ which can be obtained empirically. $P_0(t)$ represents the arc dissipated energy which related to arc conductance and $L_{arc}(t)$.

However, as it is explained in [35], the dissipated power of arc is derived and calculated considering convection effects. The convection effects are based on the disconnection length and speed of train which effect strongly the reignition and extinction of the pantograph arc. One of the common ways of convection effects is traverse blowing arc effect which is perpendicular to the arc axis. Based on [55], the dissipated power of per unit length generated by traverse blowing arc has a relation with speed of train which is obtained by experimental result [55]. The detailed explanations about the relation of dissipated power with speed of train are expressed in Appendix A.2 (eq. A.2.3 – eq. A.2.5). The total equation of dissipated power of arc can be obtained by equation (2.21) considering the speed of train.

$$P_0(t) = \begin{cases} k g_{arc}^{\beta}(t) L_{arc}^{n}(t) & if \quad v < v_0 \\ L_{arc}(t) b k_1 (v + a)\sqrt{I_p(t)} & if \quad v \geq v_0 \end{cases} \tag{2.21}$$

where $k, g_{arc}, \beta, n, k_1, v$ and v_0 are the coefficient of pyroelectric, arc conductance, the power constant of arc dissipation, undetermined arc parameter, correlation coefficient of dissipated power for arc, speed of train and specific value of train speed, respectively. For the parameters k and β, the ranges of their values are k >0 and 0< β <3, according to measured data in the

pantograph arcing test system developed in [46] and [56]. a and b have to be identified based on experimental data. The equation (2.22) depicts all the important relations to obtain the arc resistance.

$$\begin{cases} R_{arc}(t) = \dfrac{1}{g_{arc}(t)} = \dfrac{1}{g_c(t)} + \dfrac{1}{g_m(t)} \\ \dfrac{dg_m}{dt} = \dfrac{1}{\tau_1}\left[\dfrac{I_p(t)^2}{P_0(t)} - g_m(t)\right] \\ \dfrac{dg_c}{dt} = \dfrac{1}{\tau_2}\left[\dfrac{I_p\,(t)^2}{u_c(t)^2 g_c(t)} - g_c(t)\right] \\ \text{with,} \\ u_c(t) = CL_{arc}(t) \\ P_0(t) = \begin{cases} kg^{\beta}L_{arc}(t)^n & if \quad v < v_0 \\ L_{arc}(t)bk_1(v+a)\sqrt{I_p} & if \quad v \geq v_0 \end{cases} \\ L_{arc}(t) = \dfrac{L_1}{t_1 - t_{start}}(t - t_{start}) \qquad if \qquad t_{start} \leq t \leq t_1 \\ L_{arc}(t) = \dfrac{L_2}{t_2 - t_{end}}(t - t_{end}) \qquad if \qquad t_2 \leq t \leq t_{end} \end{cases} \tag{2.22}$$

Based on equation (2.22), it can be deduced that the minimum value of arc conductance, i.e. the maximum value of arc resistance occurs in $I_p(t) = 0$. Thus, voltage spikes appear on primary of transformer for zero crossing current. Considering the elements in the power model, such as inductance and capacitances that change the phase shift of current must be precisely known at each time in order to have accurate values of voltage. Finally, voltage spikes time location depends on train position regarding substation, catenary parameters and electromechanical chain that modify phase shift of current on the secondary part of the transformer.

All the required information to calculate the arc resistance are presented. Now, it is needed to identify the required parameters which are $k, \beta, n, k_1, v, v_0, a, b$ and C based on experimental results which are explained in detail in next chapter.

2.3.3 Power transformer

Power transformers are one of the most expensive components in railway traction systems. In order to reduce industrial costs and facilitate validation and verification steps, having an accurate simulation model of power transformer is necessary. The model is then used in a simulation process to test several risk occurrences, previously to verification process. The simulated model should consist of physical phenomena considering exchanged energies. As a part of a whole traction system, the transformer model should be simple enough from user point of view as well. The simulation parameters are determined using experimental results in ideal conditions. Those results are often used to validate the simulation results.

In this section, the definitions and principles of power transformer are described in detail. The electrical circuit of power transformer including the nonlinear magnetizing inductance in input power chain is considered. The bond graph methodology is used to describe the energy transfer in whole system and to be able to extract the state equation of input power system.

2.3.3.1 Definitions

Transformers are static devices that induce magnetic coupling between electrical circuits to transfer energy from one circuit to another. This thesis deals with the power transformer used in power application such as electrified railway exclusively.

A usual transformer consists of two or more coupling windings on a magnetic core. There is a pair of winding for each phase of power transformer, namely, primary and secondary which are linked by magnetic core. The transformer core is also made of a high magnetic-permeability iron that makes high magnetic flux density. Principally, a transformer works on electromagnetic induction. Figure 2-20 shows a single-phase power transformer which consists of a magnetic core and two windings wound in the primary and secondary part around the core [57].

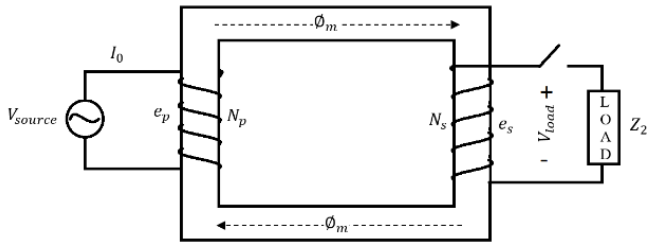

Figure 2-20 Ideal transformer with primary and secondary windings

The windings in primary and secondary are linked by a mutual flux. As an ideal transformer, it must consider following features:

- The windings have perfect conductivity which means the copper losses are zero in primary and secondary coil.
- The energy dissipation from hysteresis and eddy currents in the magnetic core is zero.

- The magnetic permeability in the core is perfect and constant that means the reluctance or magnetic resistance is zero. So, there is no leakage inductance.
- There is no need to have magnetizing current to set up the magnetic flux.
- Due to the constant permeability, the core has linear magnetic characteristics.

Due to the same linkage flux induces voltage in primary and secondary windings, the volts per turn is the same for both winding. If a load is connected to the secondary part, the current will flow in the secondary and hence in primary part (Appendix A.3 (equations (A.3.1) and (A.3.2))).

These assumptions and analysis for ideal transformer are helpful when the fundamental operation of transformer is considered. However, these features and assumptions are not applicable on experimental power transformer. In experimental transformer, there are loss of energy in no load and load conditions. These losses are such as copper, leakage flux, magnetic flux and core losses which have to be considered in non-ideal model of transformer.

- Copper losses

The total losses take place in the winding of transformer are known as the copper losses. It is important to keep these losses as low as possible to increase the efficiency of the transformer. To determine the copper losses, the short circuit test is performed on the transformer.

- Leakage flux losses

The leakage flux is the part of the total flux of winding that links only in the windings itself and the metallic body parts of the transformer. It is represented by an inductance in secondary and primary of transformer. Due to the cost constraints, it is always considered to minimize the leakage reactance as possible in design aspects.

- Magnetic flux looses

The part of total flux linked with both windings in secondary and primary is called magnetic flux. This effect is represented by an inductance in the parallel of primary windings.

- Core losses

The power losses take place in iron core are called core losses. They occur due to alternating flux set up in the core. These power losses are constant and independent of load. To determine the core losses, it is required to perform the open circuit test on transformer. These power losses have two components explained in the following.

- Eddy current losses

Due to the alternating flux in the transformer, the electromotive force (EMF) is induced in the core. This EMF causes a current to flow through the transformer core which is called eddy

currents. As the transformer core has some finite resistance, some power losses take place known as Eddy current losses.

- Hysteresis losses

Hysteresis loss is due to the successive reversal of flux in the magnetic circuit and it is proportional to the area of hysteresis loop in the $B-H$ curve. This loss increases when the operating frequency is increased [57].

The hysteresis behavior of core losses has an impact on primary current of transformer during energization. This impact can be important depending on the amplitude of supply voltage at instant of contactor closure and the residual flux at that moment. The produced flux in the transformer would be different due to the different applied voltage level at the closure time. The detailed equations are presented in Appendix A.3 (equation (A.3.4) -(A.3.7)).

Therefore, to obtain the magnetizing current in transformer, it is required to have hysteresis characteristics of magnetizing inductance in transformer which illustrates the variation of magnetizing current as a function of magnetic flux.

Assuming that the energization of transformer is done once the voltage value is zero at t=0. Figure 2-21 illustrates the current behavior obtained by hysteresis characteristics of transformer.

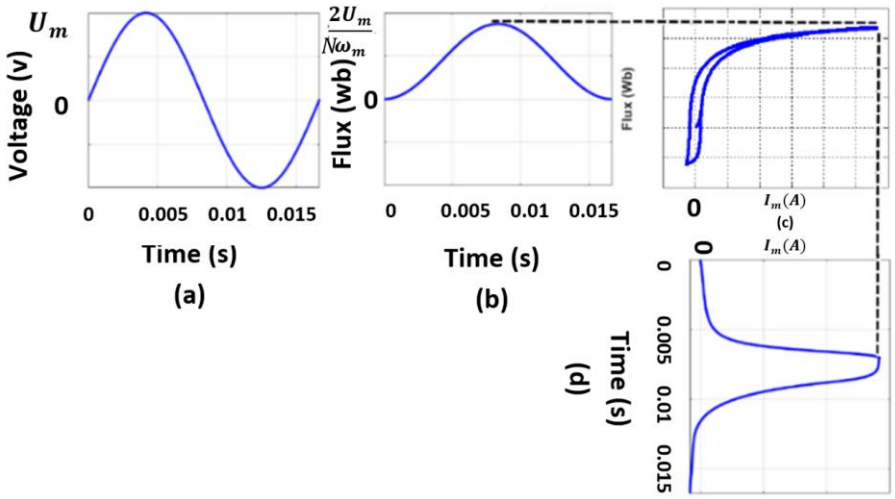

Figure 2-21(a) voltage of inductor (b) calculated flux (c) hysteresis characteristics of inductance (d) computed current of inductor (Inrush current)

Note that the initial value of residual flux is assumed zero in figure 2-22. This current, namely inrush current, can appear during energization of transformer and can reach up several times more than nominal current of transformer [58]-[65]. It can cause undesirable effects to the power transformer or even the entire system, such as mechanical stress on winding, noise, reduction of power quality, etc [66]. This current decreases in steady state condition, namely magnetizing current. If the applied voltage has maximum value of peak at *t=0*, the flux will have less amplitude at this moment and the current can be obtained from steady state part of

hysteresis loop as figure 2-22. In this case, the magnetizing current will be started from the beginning and the inrush current will not appear or negligible.

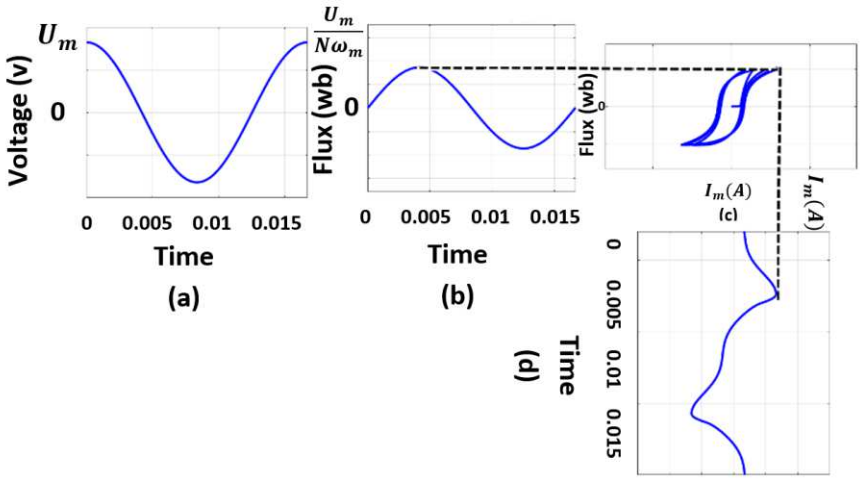

Figure 2-22(a) voltage of inductor (b) calculated flux (c) hysteresis characteristics of inductance (d) computed current of inductor (magnetizing current)

Therefore, having nonlinear characteristic of transformer core can help us to predict the dynamic behavior of transformer in different conditions.

Considering mentioned losses on non-ideal transformer, the practical single-phase power transformer can have equivalent electrical circuit as figure 2-23.

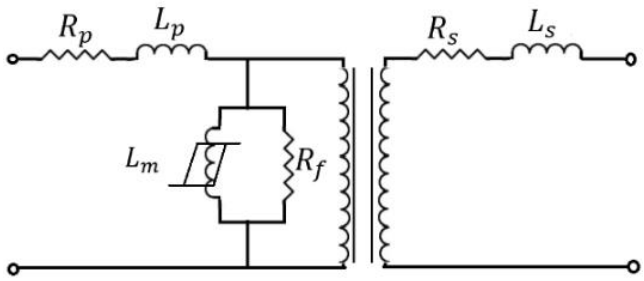

Figure 2-23 Equivalent circuit of single-phase power transformer

A precise model of power transformer depends on the accurate description of its magnetic characteristics. This characteristic depicts the nonlinear, hysteretic, and dynamic behavior due to copper and core losses in electrically conducting magnetic materials [66].

In many previous studies, non-ideal transformer model was proposed [67]-[70]. In [71], the analysis and modelling of the transformer is presented based on Kirchhoff law by neglecting the influence of leakage flux and hysteresis behavior of magnetizing inductance. These approaches allow to establish equivalent electrical circuit model. Nevertheless, these models do not express inner electromagnetic nonlinear phenomena. To address this drawback, numerical simulations of single-phase transformer using inaccurate characterization of Jiles-Atherton (JA) model is proposed in [72] based on the finite element method. In [73], the transformer model

based on Transmission Line Model (TLM) is proposed using an accurate characterization of JA model.

However, characteristics and effects of substation and catenary are necessary in our case but are not associated with non-linear transformer model in previous literature. In this thesis, the innovation is to accurately model the transformer nonlinearities as a part of the whole input part of the traction system. Using the complete model of input power chain let us simulate its behavior in different conditions such as steady state and transient. The nonlinear model of transformer is used considering mentioned losses with hysteresis behavior of magnetizing inductance and R_f as eddy current losses. Using the complete model of input power chain let us simulate its behavior in different conditions such as steady state and transient.

2.3.3.2 Input power model

In this thesis, the complete input power chain is considered including nonlinear model of transformer with two windings in the secondary part (figure 2-24).

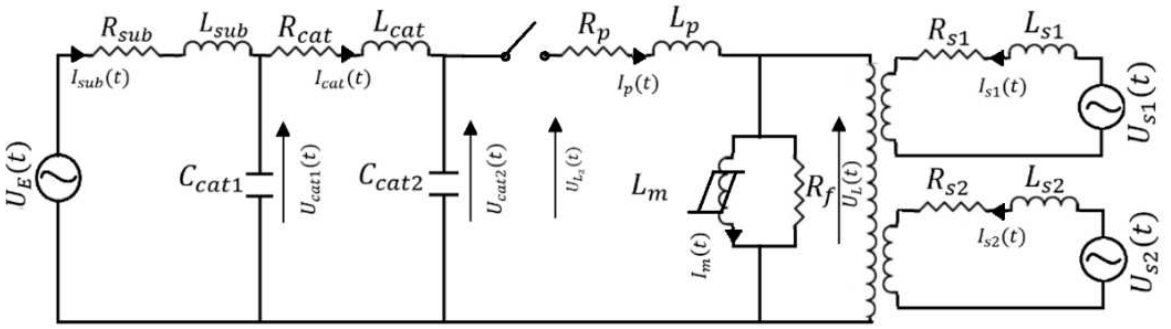

Figure 2-24 Input power chain including nonlinear model of transformer

Figure 2-24 represents input power of traction system with single phase transformer considering nonlinear characteristics of magnetizing inductance. Other elements of equivalent circuit of input power chain are the same as previous section (2.3). As it is done in two last sections, the state equations are needed to have simulation model of input power chain. The state equations can be obtained based on generalized variables and causalities described in the bond graph. In next part, the bond graph of whole system is presented in detail.

2.3.3.3 Bond graph of input power chain including nonlinear magnetizing inductance

Considering the electrical circuit of input power chain, all the series and parallel elements must be connected by 1-junction and 0-junctions respectively. Figure 2-25 shows the bond graph of whole traction system considered in figure 2-24 using elements, junctions and integral causality described in [28].

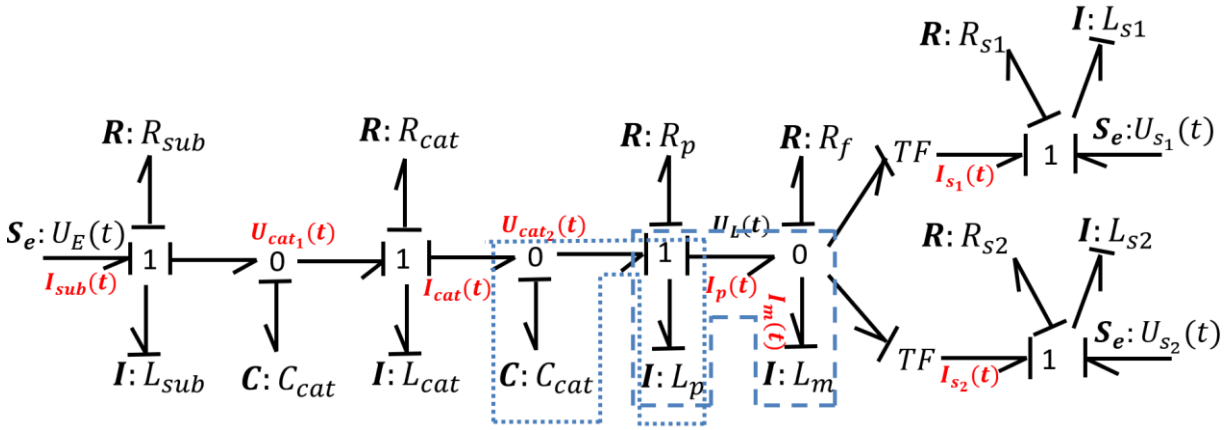

Figure 2-25 Bond graph of input power of traction system including substation, catenary and non-ideal transformer

As shown in figure 2-25, there are eight state variables: Current of substation, catenary, primary of transformer, magnetizing current and two secondary windings and two voltages of catenary in two side of ∏ model. There are also three input sources: voltage of substation and two voltage sources which represent the rest of traction system in the secondary. Two causal loops are demonstrated between storage elements in figure 2-25: a causal loop between capacitor of catenary and leakage inductance of transformer, leakage inductance and magnetizing inductance of transformer.

Based on the bond graph of transformer, it is concluded that it gets the flow and apply the voltage. Therefore, the bond graph of traction system including the causalities is completed considering the converter model as a linear model which transfer the voltage from transformer to motor. Figure 2-26 illustrates the overall traction system with all the causalities.

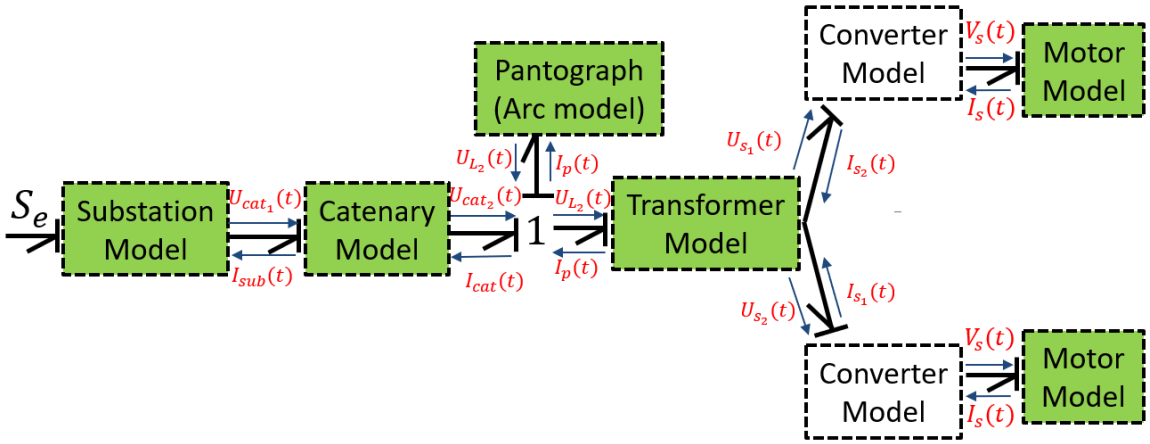

Figure 2-26 Traction system bond graph considering the causalities

In next part, the state equations are presented using causalities in figure 2-25.

2.3.3.4 State equations

Considering all energy variables and causalities illustrated in figure 2-25, state equations and variables can be easily obtained as equations (2.23) -(2.29).

$$\dot{I}_{sub}(t) = \frac{-R_{sub}}{L_{sub}} I_{sub}(t) - \frac{1}{L_{sub}} U_{cat_1}(t) + \frac{1}{L_{sub}} U_E(t) \tag{2.23}$$

$$\dot{I}_{cat}(t) = \frac{-R_{cat}}{L_{cat}} I_{cat}(t) + \frac{1}{L_{cat}} U_{cat_1}(t) - \frac{1}{L_{cat}} U_{cat_2}(t) \tag{2.24}$$

$$\dot{U}_{cat_1}(t) = \frac{1}{C_{cat_1}} I_{sub}(t) - \frac{1}{C_{cat_1}} I_{cat}(t) \tag{2.25}$$

$$\dot{U}_{cat_2}(t) = \frac{1}{C_{cat_2}} I_{cat}(t) - \frac{1}{C_{cat_2}} I_p(t) \tag{2.26}$$

$$\dot{I}_p(t) = \frac{U_{cat_2}(t)}{L_p} - \frac{R_p}{L_p} I_p(t) - \frac{U_L(t)}{L_p} \tag{2.27}$$

State equations in secondary part of transformer are such as:

$$\dot{I}_{s_1}(t) = \frac{\left(-R_{s_1} I_{s_1}(\mathrm{t}) + m_1 U_L(\mathrm{t}) - U_{s_1}(\mathrm{t})\right)}{L_{s_1}} \tag{2.28}$$

$$\dot{I}_{s_2}(t) = \frac{\left(-R_{s_2} I_{s_2}(\mathrm{t}) + m_2 U_L(\mathrm{t}) - U_{s_2}(\mathrm{t})\right)}{L_{s_2}} \tag{2.29}$$

In (2.27) -(2.29), $U_L(t)$ is:

$$U_L(t) = R_f\left(I_P(t) - m_1 I_{s_1}(t) - m_2 I_{s_2}(t) - I_m(t)\right) \tag{2.30}$$

To complete the set of state equations, it is required to express the derivative of the magnetizing current $I_m\ (t)$ using magnetic relations in core and state variables. In next part, magnetizing inductance characteristics under different conditions of contactor closure are discussed and related model are proposed to calculate the magnetizing current.

2.3.3.5 Nonlinear magnetizing inductance characteristics

When the transformer is connected to the source and the secondary is on the no load operating point, there is current flow in the primary part. This current creates magnetic field that produces magnetic flux in the transformer core. The magnetic field (H) is equal to the product of magnetizing current and number of turns. And B is magnetic induction that can be obtain by division of the magnetic flux and the cross-section area of transformer. Depending on magnetic materials, the magnetic curve ($B - H$) that represents the magnetic inductance characteristics can be plotted ideally as figure 2-27.

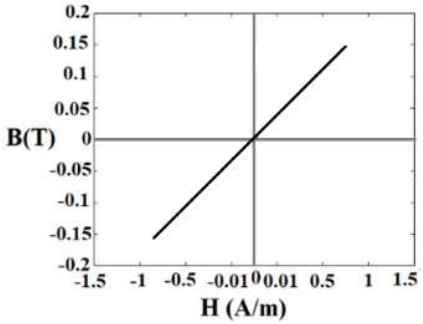

Figure 2-27 Ideal magnetic curve

However, the magnetic materials retain some of their magnetization even the magnetic field is reduced to zero. This is called the remanence. Therefore, magnetic curve is not the same while decreasing and increasing the magnetic field. Thus, magnetic curve is like a hysteresis loop shown in figure 2-28.

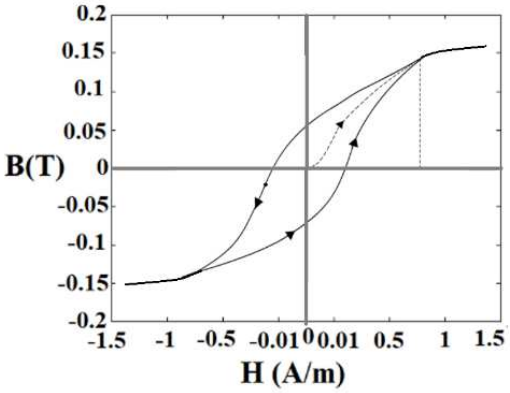

Figure 2-28 Non-ideal magnetic curve

To have the characteristics of the magnetizing inductance, it is required to obtain the $B-H$ function which illustrates different behavior of magnetic core. Subsequently, it permits us to have the magnetic flux-magnetizing current curve ($\emptyset_m - I_m$) curve. There are different models to reproduce the hysteresis characteristics of magnetic components for instance: [74], [75] and [76]. Among them, Jiles-Atherton (JA) model is the most accurate and precise description of hysteresis characteristics of iron losses for power transformers [77]. This method is used in previous researches such as [78]. However, it is not able to model the behavior of core in deep saturation region accurately [79], especially the values of peaks in current for each cycle. Note that, in this thesis, the deep saturation region is defined when the primary current of transformer is more than nominal current value (shown in figure 2-29). In [80], to predict the correct value of inrush current, JA parameters are calculated for different test conditions and current amplitude. The test procedure to calculate the JA parameters and proposition of an algorithm to calculate the parameters for each period are complicated and takes time to test on power transformers.

Therefore, it is needed to have more accurate method to model the behavior of magnetic core in deep saturation region to model the inrush current. In [81], a $B-H$ curve is proposed for

magnetizing inductance using a tangent function. As tangent function approaches infinity in the saturation region, this model can not be representative enough. The first peak of inrush current has the biggest magnitude which is important to design the protection system of transformer. Therefore, it should be estimated precisely [82]-[85]. In [86]-[88], an analytical formula is presented to obtain the envelope of inrush current. However, to propose this formula, it is required to have the information of core saturation in addition to the magnetic core characteristics and electrical parameters. A model for magnetization curve is proposed in [89] which only requires the electrical parameters and core magnetization characteristics. However, the behavior of transformer in steady state and deep saturation region are considered as a linear equation. This approach has quite accurate result however in practice the deep saturation region as shown in figure 2-29. This result is obtained from Alstom test bench.

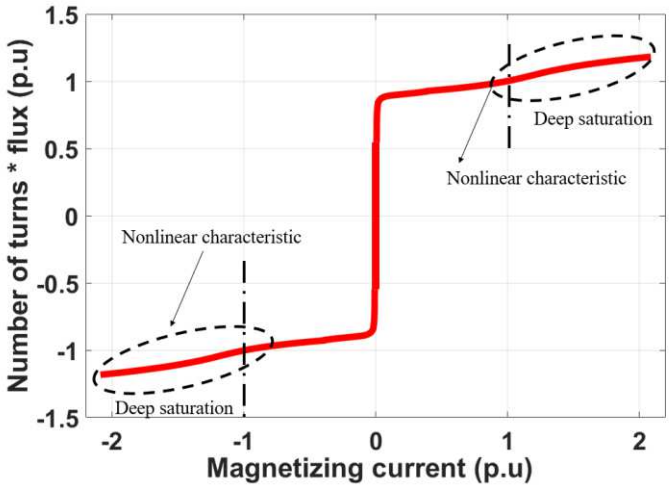

Figure 2-29 Experimental characteristic of magnetizing inductance in saturation region

This phenomenon occurs due to the line impedance in deep saturation working condition. The line impedance deviates the primary voltage of transformer. The deviation of primary voltage impacts the inrush current in deep saturation region consequently. Therefore, the characteristic of magnetizing inductance ($\emptyset_m - I_m$) will be nonlinear in deep saturation region as shown in figure 2-29. However, in real time simulator, the primary voltage of transformer is a pure sinusoidal. Therefore, in order to reproduce the nonlinear behavior of magnetizing inductance in deep saturation, it is required to demonstrate this phenomenon in ($\emptyset_m - I_m$) curve. The proposed model is discussed in detail in the following section.

In this thesis, three different working regions are considered for transformer: deep saturation region (while the current is more than nominal current), transient state (having inrush current less than nominal current) and steady state (while inrush current is negligible, and it exists just the magnetizing current). These three regions are taken into account in the proposed models.

In this chapter, to estimate the magnetic curve ($B - H$ curve), two methodologies are proposed. The behavior of magnetic curve in transient and steady state condition is considered to be a hysteresis cycle. Therefore, a specific writing of JA equations is proposed that can be inserted into state equations of the whole system and solved by a real time simulator using numerical

integrations methods (subsection 2.3.3.5.1(a)). The accurate behavior of magnetizing inductance in deep saturation region is modelled (subsection 2.3.3.5.1 (b)). In subsection 2.3.3.5.1 (c) a final model for magnetizing inductance is proposed considering both methodologies that can be easily implemented on real time simulator.

2.3.3.5.1 Magnetic curve modelling in transient and steady state

(a) Magnetic core equations

The magnetizing current $I_m(t)$ in single-phase transformers is calculated using the magnetic flux ($\emptyset_m$), the magnetic core field (H), magnetic induction (B) and magnetization (M). The magnetic flux can be obtained by taking into account the voltage of magnetizing branch $U_L(t)$ and number of turns in primary winding N (Appendix A.3 (equation (A.3.4))). The magnetic induction can be easily calculated by magnetic flux using Faraday's law (Appendix A.3 (equation A.3.8)).

The three fundamental magnetic terms can be related such as:

$$B(t) = \mu_0\big(H(t) + M(t)\big). \tag{2.31}$$

For simplicity purpose, in the following, the time dependence of B, H, M and I_m will not be mentioned in the following expressions.

Considering the relation between magnetic field and magnetization [90], (2.32) is achieved by derivative of (2.31).

$$\frac{dB}{dt} = \mu_0\left(\frac{dH}{dt} + \frac{dM}{dt}\right) = \mu_0\frac{dH}{dt}\left(1 + \frac{dM}{dH}\right). \tag{2.32}$$

Based on Ampere theorem, magnetizing current can be easily obtained (Appendix A.3 (equation A.3.9)).

Therefore, substitution of magnetic flux relation with voltage, Faraday's law and Ampere theorem in (2.32), the magnetizing current equation will be as (2.33).

$$\dot{I}_m(t) = \frac{U_L(t)}{L_m} = \frac{l.U_L(t)}{N^2 S\mu_0(1 + \frac{dM}{dH})}. \tag{2.33}$$

where l is the average magnetic path. Based on (2.33), we can assume that magnetizing inductance, denoted L_m can be expressed as (2.34).

$$L_m\left(\frac{dM}{dH}\right) = \frac{N^2 S\mu_0(1 + \frac{dM}{dH})}{l}. \tag{2.34}$$

As it is shown in (2.34), derivative of the magnetizing inductance L_m depends on $\frac{dM}{dH}$. This term can be obtained by JA model and its five parameters as detailed in the following section.

(b) Calculation of dM/dH Using JA Model

The nonlinear characteristic of hysteresis loop ($B-H$ curve) can be determined by the model which was developed by Jiles and Atherton [77], [80]. This model is based on physical considerations. The model is defined by a simple first order differential equation and characterized by five parameters. Based on this theory, the magnetization decomposes into a reversible component M_{rev} and an irreversible component M_{irr}.

$$M = M_{rev} + M_{irr}. \tag{2.35}$$

In ferromagnetic materials, the effective field H_e is the interaction between magnetic moments which defined as below:

$$H_e = H + \alpha M, \tag{2.36}$$

where α is the Weiss correction factor that represents the coupling between fields. Anhysteretic curve is the average of ascending and descending parts of the major hysteresis loop, namely, M_{an}. It can be represented by Langevin function [91], and is such as:

$$M_{an}(H_e) = M_{sat}\left[\coth\left(\frac{H_e}{a}\right) - \left(\frac{a}{H_e}\right)\right], \tag{2.37}$$

where a and M_{sat} are shape factor and saturation magnetization, respectively. M_{rev} has a relation with anhysteretic magnetization and irreversible component of magnetization by a reversibility coefficient c which depends on material nature as below:

$$M_{rev} = c(M_{an} - M_{irr}). \tag{2.38}$$

The differential equation associated with irreversible magnetization component is defined by [77]:

$$\frac{dM_{irr}}{dH} = \frac{\delta_m(M_{an} - M_{irr})}{k\delta - \alpha(M_{an} - M_{irr})}. \tag{2.39}$$

where k is the Boltzmann constant which is linked to coercive field and the factor of δ_m and δ as below:

$$\delta_m = \begin{cases} 1:\ if\ \dfrac{dH}{dt} > 0 \text{ and } M_{an} > M_{irr} \\ 1: if\ \dfrac{dH}{dt} < 0 \text{ and } M_{an} < M_{irr} \\ 0: \text{otherwise} \end{cases}, \tag{2.40}$$

$$\delta = \begin{cases} 1 & if \quad \frac{dH}{dt} > 0 \\ -1 & if \quad \frac{dH}{dt} < 0 \end{cases}. \tag{2.41}$$

Using (2.35) and (2.38), magnetization is obtained based on irreversible magnetization and anhysteretic magnetization as (2.42). Then, the differential equation of $\frac{dM}{dH}$ is obtained by derivation of (2.41). Some mathematical formulation on (2.37) and (2.39) are used such as $\frac{dM}{dH}$ is:

$$M = (1-c)M_{irr} + cM_{an}. \tag{2.42}$$

$$\frac{dM}{dH} = (1-c)\frac{dM_{irr}}{dH} + c\frac{dM_{an}}{dH}. \tag{2.43}$$

Several approaches proposed different expressions to calculate $\frac{dM}{dH}$ based on (2.36) -(2.43). However, in order to ease an implementation in real time simulator, it is required to have fewer differential equations and avoid algebraic loop. Based on (2.34), there are two differential expressions: $\frac{dM_{irr}}{dH}$ and $\frac{dM_{an}}{dH}$. As presented in [77], the expression $\frac{dM_{an}}{dH}$ can be obtained using magnetization and magnetic field which is presented in the following. However, it is needed to have another expression for $\frac{dM_{irr}}{dH}$ to reduce the differential equations in simulation. Our objective in this thesis is to propose an expression of $\frac{dM}{dH}$ independent of M_{irr} but only dependent of state variables. These state variables are H and B which are obtained by Ampere theorem and Faraday's law respectively and state variables presented in (2.27)- (2.30) and (2.33). By reforming (2.42), irreversible magnetization is defined as:

$$M_{irr} = \frac{M - cM_{an}}{1-c}. \tag{2.44}$$

Therefore, the differential equation associated with irreversible magnetization is:

$$\frac{dM_{irr}}{dH} = \frac{\delta_m(M_{an} - M)}{(1-c)\left(k\delta - \frac{\alpha(M_{an}-M)}{1-c}\right)}. \tag{2.45}$$

Then, the differential equation of anhysteretic magnetization based on magnetic field will be as equation (2.46):

$$\frac{dM_{an}}{dH} = \frac{dM_{an}}{dH_e}\frac{dH_e}{dH}. \tag{2.46}$$

Considering equation (2.36), the differential of anhysteretic magnetization is established as:

$$\frac{dM_{an}}{dH} = \frac{dM_{an}}{dH_e}\frac{d(H+\alpha M)}{dH} = \frac{dM_{an}}{dH_e}\left(1 + \frac{\alpha dM}{dH}\right), \tag{2.47}$$

where,

$$\frac{dM_{an}}{dH_e} = \frac{M_{sat}}{a\left(1 - Coth^2\left(\frac{H_e}{a}\right) - \left(\frac{a}{H_e}\right)^2\right)}. \quad (2.48)$$

Finally, the differential of magnetization is rewritten as given in (2.49).

$$\frac{dM}{dH} = \frac{\frac{cdM_{an}}{dH_e} + \frac{\delta_m(M_{an} - M)}{\delta k - \frac{\alpha(M_{an} - M)}{1 - c}}}{1 - \frac{\alpha c dM_{an}}{dH_e}}. \quad (2.49)$$

Therefore, as it is discussed in previous section, magnetizing current is calculated using (2.49). The term $\frac{dM}{dH}$ depends on M, M_{an} and $\frac{dM_{an}}{dH_e}$. First of all, as shown in (2.31), M is a function of B and H. B is itself a function of state variables through the integration of U_L (Appendix (A.3.4)) and Faraday's law. H is also a function of a state variable (Ampere theorem). Finally, M_{an} and $\frac{dM_{an}}{dH_e}$ are functions of $H_e$established by (2.37). H_e is itself a function of H and M (equation (2.38)) and then a function of state variables. Therefore, the equation (2.50) expresses the magnetizing current as a function of all state variables.

$$\dot{I}_m(t) = \frac{l.(R_f(I_P(t) - m_1 I_{s1}(t) - m_2 I_{s2}(t) - I_m(t)))}{N^2 S \mu_0 (1 + \frac{dM}{dH})}. \quad (2.50)$$

So, all state variables of input power system of our traction system can be easily calculated using (2.23) -(2.29), (2.50). However, to simulate the whole system, it is necessary to identify the five parameters of JA model (α, k, c, a, M_{sat}) and then to have the hysteresis characteristic of the magnetic core based on experimental results. In the next chapter, the procedure of parameter identification and an analysis on process of identification are done.

Nonlinear characteristics of magnetic core by hysteresis loop leads us to obtain the behavior of transformer. However, while the transformer is fully magnetized and produce the maximum magnetic flux, JA model cannot be representative enough for the nonlinear behavior of magnetic core in deep saturation condition. Therefore, in next section, a method is proposed to obtain its characteristics in deep saturation.

2.3.3.5.2 Magnetic curve modelling in saturation region

The performance of transformer is constrained by the limitation of magnetic material. The ferromagnetic core transformer can not support infinite magnetic flux densities due to the causalities. Which means that increasing the magnetic field force, the magnetic field flux does not increase proportionally, and it will be saturated in a limited value. This phenomenon happens while transformer is overloaded from excessive applied voltage or during the energization process. In this case, the transformer experiences inrush current due to initial value

of magnetic flux in core. It distorts the waveforms and creates harmonics in the primary and secondary in the case of having load. In practice, the hysteresis cycle of $B-H$ curve in the deep saturation condition tends to be thin. This means that the variation of magnetic induction is negligible during decreasing and increasing of magnetic field compare to the maximum value of magnetic field and magnetic induction.

To have $B-H$ curve experimentally in the saturation region, it is required to do some steady state test on no load transformer with 1.5 p.u of nominal input voltage [92]. This allows to have magnetizing curve behavior in wide ranges to propose the model. However, this kind of measurements are not feasible on power transformer. As it is required to have oversized power supplies, there are several risks of damage for transformer due to the over voltage and over current condition. In addition, to propose an adequate model for magnetizing inductance in deep saturation, it would require at least 2 p.u test which is not possible to do on high power units. Therefore, the best opportunity to obtain the magnetizing curve in saturation region in deepest condition, is during the energization of transformer. In this condition, the transformer has to be fed by nominal input voltage and then the contactor closure has to be done at *t=0* or at least an instant that sinusoidal voltage has minimum value. This test procedure has to be done for number of times in order to achieve the deepest condition.

Once, the largest amplitude of inrush current is obtained experimentally, the experimental magnetic flux and magnetizing current have to be computed using the input voltage of transformer and inrush current (Appendix A.3 (equation (A.3.4), (A.3.9) and (A.3.10)). As the magnetizing current and the magnetic flux have different values in each period during the transient state, it allows us to have the exact characteristics of $B-H$ curve for different functional points. To extract the functional points, the maximum point of magnetizing current and then the corresponding point on magnetic flux are desired. Figure 2-30 shows an example of magnetic flux and magnetizing current and their extracted maximum values.

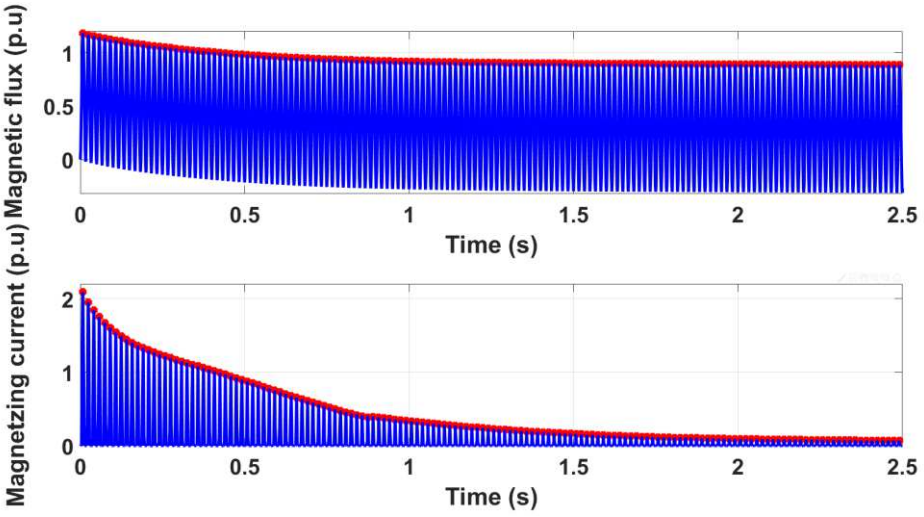

Figure 2-30 Magnetic flux and magnetic current with extracted peak values

Note that the units are in per unit which means that all values are divided by the nominal value of flux and current of transformer presented in datasheet.

Then, by replotting the extracted maximum points of magnetizing current and magnetic flux, $B-H$ curve for the transformer in saturation region can be obtained. To have the magnetic curve in negative part, the obtained figure can be mirrored as figure 2-31.

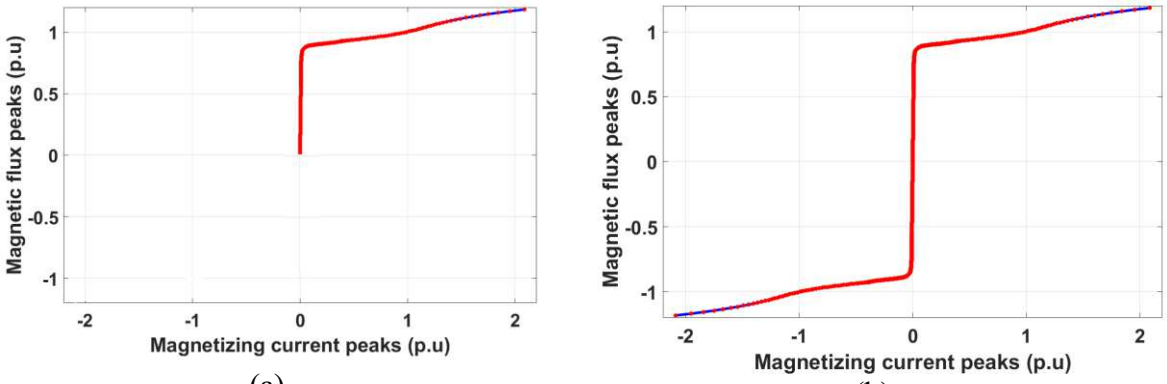

(a) (b)

Figure 2-31 (a) Extracted peaks of magnetic flux and magnetizing current (b) Mirrored of figure 2-31 (a)

Figure 2-31 represents the magnetic behavior of transformer for different points in deep saturation region. The two deep saturation regions in positive and negative quarter and one in the middle. Therefore, the general relation between magnetic flux and magnetizing current can be represented by conditional functions as below:

$$I_m(\emptyset_m) = \begin{cases} f_1(\emptyset_m) & for \quad \emptyset_m \geq \emptyset_m \\ f_2(\emptyset_m) & for \quad |\emptyset_m| < \emptyset_m \\ -f_1(\emptyset_m) & for \quad \emptyset_m \leq -\emptyset_m \end{cases} \tag{2.51}$$

where $f_1(\emptyset_m)$ represents nonlinear characteristics of magnetizing inductance in deep saturation region. It is required to use curve fitting methodology to find out a model for $f_1(\emptyset_m)$. Then, it is required to identify the parameters of model obtained by curve fitting method. The proposed methodology to find out $f_1(\emptyset_m)$ based on the extracted peaks from experimental results, allows us to simulate the envelope of inrush current. It is also possible to propose a mathematical relationship such as polynomial equations for $f_2(\emptyset_m)$ and then, identify the coefficients of the equations. However, considering linear or polynomial equation is not accurate enough for steady state. To simulate accurately the region in the middle of $B-H$ curve, it is required to consider the normal condition of transformer in transient and steady state. Therefore, the equations for hysteresis characteristics of transformer proposed in subsection 2.3.3.5.1 are suitable to be replaced by $f_2(\emptyset_m)$. The final model of magnetizing inductance is proposed in next subsection.

2.3.3.5.3 Magnetizing inductance final model

As it is needed to propose magnetizing current equation to calculate all the state equations of input power chain in section (2.3.3.4). The magnetizing inductance characteristics is different

in the deep saturation region, transient and steady states. Therefore, it is required to propose a model that can cover these two important states. In steady transient and steady conditions or generally non-saturated regions, hysteresis cycle has the best representation for magnetizing inductance. As explained in subsection (2.3.3.5.1), the rewritten JA model is proposed to simulate the hysteresis cycle and non-saturated condition. As mentioned previously, in deep saturation region while the amplitude of current can be several times more than nominal value. In this case, the $B-H$ curve is impacted by line impedances which causes nonlinearity in its characteristics. A nonlinear function is proposed based on experimental extracted peaks of magnetizing current and magnetic flux. Before presenting the final equation, it is necessary to note two important points. In practice, once the contactor is closed, there are two possibilities. Either, the transformer is in the deep saturation region and after a while, it will be in the transient and then steady state, or, the transformer is in the non-saturated region in the beginning of switching time. To start the simulation, the peak amplitude of primary current of transformer in the first cycle has to be known. If its absolute value is less than the critic value (which is considered as nominal current value in this thesis), the transformer is in transient state. Therefore, the JA model would be selected as a model of magnetizing inductance. Otherwise, if the absolute value of current is more than critical value, the transformer is in deep saturation condition. Therefore, the simulation has to be started by solving the equations in the saturation region and then, once the value of peak in the magnetizing current reduces to a critic value, simulation continues using JA model. The final equation for magnetizing current is as 2.52:

$$\begin{cases} If\ \ I_{m_{peak_1}} < I_{m_0}: \\ \qquad \dot{I}_m(t) = \dfrac{l.\left(R_f\left(I_P(t) - m_1 I_{s1}(t) - m_2 I_{s2}(t) - I_m(t)\right)\right)}{N^2 S \mu_0 \left(1 + \dfrac{dM}{dH}\right)} \\ If\ \ I_{m_{peak_1}} \geq I_{m_0}: \\ \qquad I_m(t) = \begin{cases} f_1(\emptyset_m) & if\ peak\left(I_m(t-1)\right) > I_{m_0} \\ \displaystyle\int \frac{l.\left(R_f\left(I_P(t) - m_1 I_{s1}(t) - m_2 I_{s2}(t) - I_m(t)\right)\right)}{N^2 S \mu_0 \left(1 + \dfrac{dM}{dH}\right)} & if \left|peak\left(I_m(t-1)\right)\right| < I_{m_0} \\ -f_1(\emptyset_m) & if\ peak\left(I_m(t-1)\right) < -I_{m_0} \end{cases} \end{cases} \tag{2.52}$$

Let us remind that the critical value is considered as nominal current of transformer ($I_{m_0} = I_{p_{nominal}}$) in this thesis.

In next chapter, the required parameters for proposed model are identified based on experimental measurements on test bench.

2.3.4 PEM Fuel cell

Fuel cells (FCs) are electrochemical device which convert the chemical energy to electricity. They are one of the most promising renewable energy sources. They are environmentally clean, and they have low emission of oxides of nitrogen and sulfur. In addition, they have low level of noise and they can provide energy in a controlled way with higher efficiency compare to conventional power plants [93]. For this reason, this technology is expanding rapidly, and many research lines associated with various sectors are done recently. Basically, there are three different sectors namely, transport sector, the portable device sector and stationary application sector [94]. The transportation sector is a major consumer of FC.

There are wide range of FC technologies classified into different categories based on fuel used, operating temperature and type of electrolyte. The main FC technologies based on electrolyte are proton exchange membrane (PEMFC), direct methanol (DMFC), Alkaine (AFC), phosphoric acid (PAFC), molten carbonate (MCFC) and solid oxides (SOFC). PEMFC has lower temperature (under 100°C), fast connection time and easiest manufacturing process compare to the other types of FC [95]. It has dynamic response in the case of load variation, and it is compact, lightweight, noiseless [95]. In this thesis, PEMFC model in transportation applications are presented. The state equations are proposed based on energy transfer links in the whole system using multi physical method of bond graph.

2.3.4.1 Definitions

The proton exchange membrane fuel cell (PEMFC), also called the solid polymer fuel cell (SPFC), was first developed by General Electric in the United States in the 1960s for use by NASA on their first manned space vehicles [95]. The development of PEMFC went more or less into abeyance in the 1970s and early 1980s. However, there was a renaissance of interest in this type of cell [96] in the latter of 1980s and the early 1990s. The developments have brought reduction of platinum use by a factor of over 100 and current density up to around 1 A. cm^{-2} [95]. These improvements cause a huge reduction in cost and improved power density [95]. Therefore, PEMFCs are being used on different industrial applications such as electrified railways.

The open circuit voltage of PEMFC is obtained by the differential potential between oxidant (Oxygen coming from air) and fuel (Hydrogen) in cathode and anode, respectively [95]. The maximum differential potential provided by PEMFC is about 1.23 V. In the railway applications, to have sufficient amount of power (around 250 kW) to supply the whole traction system, PEM fuel cell system is used. It consists of several PEMFC stacks in different configuration in series, parallel or combination of series and parallel. To manage an adequate gas, it is required to have several auxiliaries such as hydrogen, cooling, air and the humidification circuit. Figure 2-32 illustrates a PEMFC single cell (a), stack (b) and system (c) schematic. In figure 2-32 (b), the PEMFC stacks consists of a multitude of single cells stacked up. Each single cell is constituted by membrane, electrodes which are the catalyst layer, gas diffusion layer and bipolar plate to separate the cells connected in series.

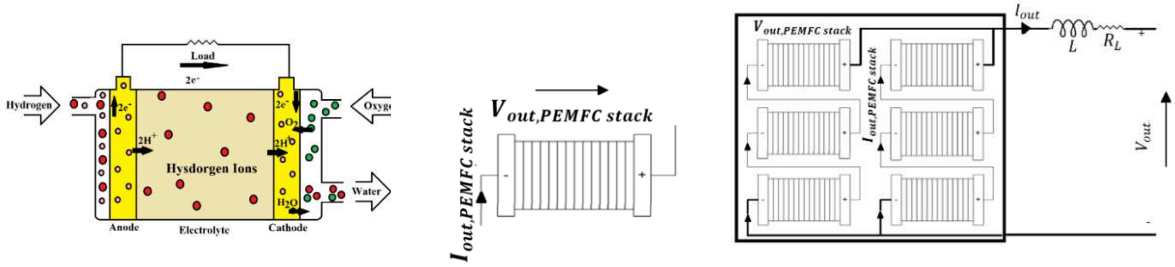

(a) (b) (c)

Figure 2-32(a) the basic structure of PEMFC single cell (b) Stack (c) system

In the structure of PEMFC single cell in figure 2-32 (a), hydrogen is fed through a channel and it accumulates in the anode layer where it is dissociated into protons flows through the membrane. The membrane part of fuel cell works as an electrolyte which does not allow the electrons to pass. So, the electrons are collected as electrical current by external load linked to the electrodes. In cathode side, the oxygen flows through a similar channel and it accumulates in cathode where it combines with electrons transferred to the platinum and the protons in membrane react. Therefore, water will be produced. All the relations and information corresponding to chemical reactions in anode and cathode parts are explained in detail in Appendix (A.4) (equations (A.4.1) -(A.4.10)).

In the PEMFC stack structure, the cathode of a single cell is electrically connected to the anode of the adjacent cell. In this thesis, it is assumed that the parameters in individual cells can be lumped together to represent PEMFC stacks. Thus, it is assumed that the same current passes through each cell on the stack, denoted $I_{cell}(t)$. Considering the overall current of PEMFC system as $I_{out}(t)$, the current for each single cell is as below:

$$I_{cell}(t) = \frac{I_{out}(t)}{N_{stack,parallel}} \tag{2.53}$$

where $N_{stack,parallel}$ number of series stacks in parallel, respectively. Supposing the output voltage response of each single cell as $V_{cell}(t)$, the output voltage of PEMFC system can be calculated as (2.54).

$$V_{out}(t) = \left(N_{cell}N_{stack,series}V_{cell}(t)\right) - V_L(t) - V_{R_L}(t) \tag{2.54}$$

where N_{cell} and $N_{stack,series}$ are number of single cells in PEMFC stacks and number of stacks in series, respectively. $V_L(t)$ and $V_{R_L}(t)$ represent the voltage losses due to impedance of cables which can have an impact on dynamic response. The output voltage of each cell depends on the internal configuration of PEMFC which is explained in the following.

PEMFC stacks are obviously the heart of PEMFC system. However, it is required the supporting equipment to be useful and perform efficiently. Typically, the PEMFC systems

involves several subsystems such as oxidant supply, fuel supply, heat management, water management, power conditioning and instrumentation and controls. Figure 2-33 depicts a PEMFC stack with the involved auxiliary circuits [97].

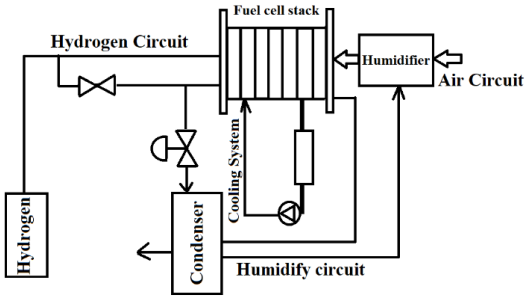

Figure 2-33 PEM FC stack and auxiliary circuits

The hydrogen circuit controls the pressure, mass/volume flow rates, temperature and vapor content of hydrogen. It has three different operation modes, open, close and feedback [97]. While the hydrogen circuit is in open mode, the remainder of hydrogen is released to the water condenser used by cooling system [97]. The hydrogen exit valve is closed during the close mode. In the feedback mode, the remainder hydrogen is re-injected into the cell [97]. The humification process involves heating air and its humidification at high temperature. Then cooling of this process is to have low temperature until to get the saturated mix of water vapor and air at the desired temperature measured by sensors. The most important auxiliary circuit is the air supply circuit. In order to have medium or high power PEMFC stacks, the air circuit depends on an air compressor [97]. There is also a control system which sends or receives the commands depending on the operating modes. The control system structure is different depending on the designers.

The testing activities are the most important issue due to security and cost reasons in railway traction system design. Therefore, having a representative simulation model of chain components is required. The simulated model of components such as PEMFC system has to be compatible with overall traction system model. Thus, the simplicity and representativity of PEMFC system model are in priority. The model has to be suitable for system simulation and not for design purpose. The PEMFC system model has to consist of the PEMFC stack model and the auxiliary circuits.

Several approaches are done to propose the static and dynamic model of PEMFC stacks [98]-[103] which provide the polarization curve (voltage as a function of current). In last few years, the numerical modeling, computer simulation and PEMFC stacks performance have been proposed [95] and [104]- [106] . State-space modelling of PEMFC is proposed in [107]. These approaches allow us to establish equivalent electrical model of PEMFC. There are several approaches to propose the PEMFC stacks model using graphic way of power transfer in the system. In [108]-[110], PEMFC stack model is proposed based on bond graph methodology [111] which illustrates the energy exchange within overall system. Generally, the methodology of bond graph is applied to model the PEMFC stack in the following sections.

As mentioned in previous approaches, the polarization curve depends on numerous factors such as membrane thickness and state of hydration, catalyst loading, catalyst layer structure flow filed design and operating conditions (temperature, pressure, humidity, flowrates and etc.) [112]. Experimentally, the polarization curve is also impacted by the transient load use, which causes a hysteresis effect on the dynamic characteristics of PEMFC stack [113]. Based on several studies, the hysteresis effect occurs due to several reason such as double layer charging effect [114] and its interaction with activation losses [115] and water management in the cells [116]. Therefore, it would be necessary to take into account the PEMFC stack dynamic model, auxiliary circuits model, its control command system to realize the polarization curve of overall system in various operating modes. The detailed model of PEMFC system are presented in [117] and [118].

However, in railway application, a simplified model from user point of view is required to test the overall performance of system in different operating modes. Moreover, the detailed information and data about the PEMFC system are not often provided by the manufactures. Therefore, it is required to propose a model based on the overall profile mission of PEMFC system.

In this chapter, a simplified model of PEMFC system is proposed using the experimental profile mission on train. The PEMFC stack model is obtained using bond graph methodology. To adapt the PEMFC stacks model parameters, the output polarization curves on experimental measurements affected by several auxiliary circuits is estimated by a specific average curve. The identification process is explained in next chapter.

2.3.4.2 The electrical model of PEM Fuel cell

The electrochemical reactions which occurs between hydrogen and oxygen can be expressed by thermodynamic laws (Nernst equation). Based on this law, a DC voltage source can be considered as an output internal potential of fuel cell. However, once the electrical load is connected to the fuel cell, the internal potential will decrease due to the voltage drops caused by the kinetic electrochemical reactions, convection and diffusion process, resistance of electrons flow, and transferred ions through solid polymer membrane and electrode materials [99].

- Activation losses

Once the load is connected to two electrodes, several losses will appear inside the PEMFC due to flowing current. In the beginning of reactions, the kinetics of electrochemical reactions taking place inside fuel cell which produce activation losses. In fact, the transfer of electrical charge between chemical species and electrodes causes the variation of the Gibbs free energy at the different process stages. The energy demanded in this reaction is known as activation energy (V_{act}) [119].

- Concentration losses

The concentration phenomena are related to mass transport which is mainly occurs due to the process of convection and diffusion. The convection and the diffusion process refer to the transport of species by the bulk movement of a fluid and concentration gradients, respectively. Mainly, the mass transport in the electrodes of the FC is due to the diffusion effect. The main reason for the concertation voltage drops at high current densities is the slow transportation of reactance to reaction sites [119].

- Ohmic losses

Ohmic phenomenon is due to the resistance to the flow of electrons and transferred ions through solid polymer membrane and electrode materials, respectively. Generally, the ohmic voltage drop consists of the conductive resistance between membrane and electrodes, polymer membrane and electrodes.

However, there are some other phenomena in fuel cell that effect its dynamic behavior such as double layer charging effect, fuel and oxidant delay of internal potential etc. [119].

- Double layer charging effect

As it is mentioned before, the membrane is located between two electrodes which does not allow the electrons to pass. Therefore, the electrons will flow from anode to cathode part and gather at its surface. In one side, membrane H+ ions and on the other hand, the electrons gathered on the cathode side, create two charged layers in opposite polarity between cathode surface and membrane. These two charged layers are able to store electrical energy. They are known as electrochemical double layer and react like a super capacitor which is in the order of several Farads [95], [120].

- Thermodynamic effect

There is also the effect of system heat which will rise or drop the temperature during load transition on PEMFC. The net heat is due to the chemical reactions in fuel cell. It can be obtained considering chemical and heat energy subtracted by electrical energy, heat loss sensible and latent heat. However, the effect of net heat is managed by cooling system to avoid high temperature in the PEMFC and maintain it around a constant value defined by suppliers. Therefore, the temperature variation and consequently the thermodynamic block will not be considered in this thesis.

- Fuel and Oxidant delay

During the transient condition, a delay can be appeared between the time that the load current is changed and the time that flux and oxidant flow. The chemical reactions and details relations about the fuel and oxidant delay are proposed in Appendix A.4 (equations (A.4.11) -(A.4.18)).

Considering internal potential of PEMFC and all voltage drops and effects that change the output behavior of fuel cell, the electrical circuit model of PEMFC can be obtained as figure 2-34:

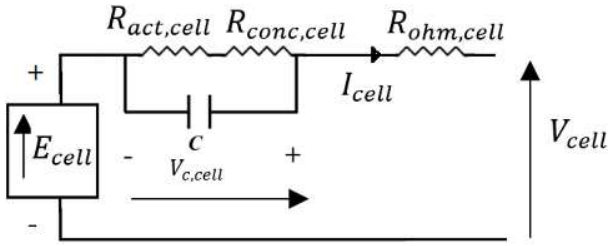

Figure 2-34 Electrical circuit model of PEMFC

2.3.4.3 Bond graph of PEM Fuel cell model

As explained in the beginning of this chapter, bond graph method helps us to define and understand the mutual energetic coupling inside the global multi-physical system. Following the methodology of bond graph, electrochemical reactions in PEMFC and its electrical model, the bond graph of the global system of PEMFC can be obtained as figure 2-35:

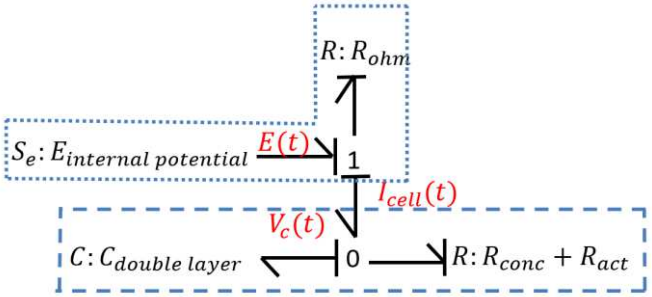

Figure 2-35 The bond graph of PEMFC

The voltage drops due to the activation, concentration and ohmic losses are modelled by $R: R_{act}$, $R: R_{conc}$ and $R: R_{ohm}$. The dynamic behavior of PEMFC driven by double layer charging effect represented by $C: C_{double\ layer}$. Two causal loops are shown in figure 2-35: a causal loop between voltage source and ohmic loss, a causal loop between a storage element $C: C_{double\ layer}$ and activation and concentration loss.

As PEMFC system produce voltage and get the flow, therefore in the traction system including PEMFC system, the causalities are as below:

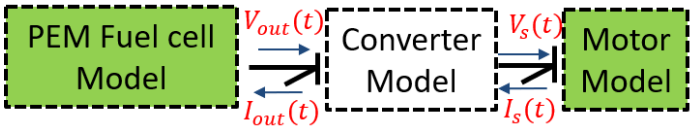

Figure 2-36 The causalities in the bond graph of traction system including PEMFC system

Based on the bond graph of figure 2-35, the state equation and the equations of electrical model of PEMFC are presented in next section.

2.3.4.4 Equations considering nonlinear characteristics of PEMFC

In figure 2-35, E_{cell} is internal voltage of PEMFC provided by chemical and mass reactions in open circuit condition. The dynamic output voltage of PEMFC (2.55) can be obtained using equations of (2.56)- (2.61).

$$V_{cell}(t) = E_{cell}(t) - V_{c,cell}(t) - V_{ohm,cell}(t) \tag{2.55}$$

where,

$$E_{cell}(t) = {E_{0,cell}}^{o} + \ln({p_{H2}}^{*}.({p_{O2}}^{*})^{0.5}) - E_{d,cell}(t) \tag{2.56}$$

where ${E_{0,cell}}^{o}, p_{H2}^{*}, p_{O2}^{*}$ and $E_{d,cell}$ represent standard reference potential at standard state (298K and 1-atm pressure), partial pressures (hydrogen and oxygen) and the fuel and oxidant delay of PEMFC, respectively (Appendix A.4 equation (A.4.19) –(A.4.22)). The fuel and oxidant delay are obtained as below [121]:

$$E_{d,cell}(t) = \lambda_e \left(I_{cell}(t) - I_{cell}(t) * exp\left(-\frac{t}{\tau_e}\right)\right) \tag{2.57}$$

where λ_e and τ_e are constant value (Ω) and overall flow delay in seconds, respectively. Note that $(*)$ is convolution product. $E_{d,cell}(t)$ is zero in steady state [119].

The ohmic voltage loss and state equation which represents the double layer charging effect are provided in (2.58) and (2.59) respectively.

$$V_{ohm,cell}(t) = I_{cell}(t)\frac{l}{S\sigma} \tag{2.58}$$

$$\dot{V}_{c,cell}(t) = \frac{1}{C} I_{cell}(t) - \frac{1}{(R_{act,cell} + R_{conc,cell})C} V_{c,cell}(t) \tag{2.59}$$

where S, l and σ are cell active area in cm^2, l is the thickness of membrane in cm (electrolyte of cell) and σ is membrane conductivity, respectively.

$R_{act,cell}$ and $R_{conc,cell}$ are activation and concentration losses of each single cell of PEMFC, respectively. They can be expressed as (2.60) and (2.61).

$$R_{act,cell}(t) = \frac{RT}{I_{cell}(t)\alpha n F} ln\left(\frac{I_{cell}(t) + I_n}{I_0}\right) \tag{2.60}$$

where n, α, I_0 and I_n are the number of transferred electrons in chemical reactions, the charge transfer coefficient, corresponding current of activation and the internal leakage current, respectively. F and R are Faraday's constant (C/kmol) and universal gas constant ((l atm)/(kmol

K)), respectively. The number of transferred electrons is 2 in PEMFC. α, I_0 and I_n are the parameters which should be found experimentally.

$$R_{conc,cell}(t) = -\frac{RT}{I_{cell}(t)\beta nF} ln\left(1 - \frac{I_{cell}(t)}{I_{limit}}\right) \tag{2.61}$$

where I_{limit} and β are the limit diffusion current and a transfer coefficient of concertation loss, respectively.

The output voltage of PEMFC single cell in steady state condition (without load transition) turns to (2.62).

$$V_{cell}(t) = E_{cell}(t) - V_{act,cell}(t) - V_{conc,cell}(t) - V_{ohm,cell}(t) \tag{2.62}$$

The static polarization curve of PEMFC stack is as figure 2-37.

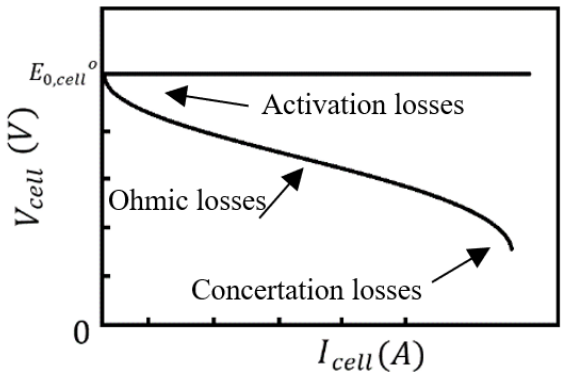

Figure 2-37 Characteristics of PEMFC single cell in steady state

As it is shown in the PEMFC equations, there are several model parameters such as: I_n, I_{limit}, I_0, λ_e, τ_e and T_C that have to be identified. This will be done and discussed precisely in chapter 3.

Since the fuel cell stack developed for railway application are commercial product, the author has no access of detailed information about stack characteristics; and the control command of the auxiliary system is considered as a black box. Therefore, the dynamic behavior of PEMFC system is estimated using the profile mission measured on train. The estimated polarization curve is presented during the identification process in the following chapter.

2.3.5 Model summary

In this section, the model of four traction subsystem are developed by considering the nonlinear parameters which were not considered in the beginning of the thesis. It is shown for each proposed model that there are several parameters in nonlinear models that required to be identified after modelling process. Table 2-3 presents list of parameter model that have to be identified.

Table 2-3 Model parameters

Proposed models	Parameters
ASM	Magnetizing inductance model parameters: a, b, c
Pantograph bounce	Electrical arc resistance model: $k, \beta, n, k_1, v, v_0, a, b, C$
Transformer	JA model: k, α, c, a
	Curve fitting model: It depends on the equation which will be proposed
PEM Fuel cell	Nonlinear voltage loss model: I_n, I_{limit}, I_0, λ_e, τ_e, T_C

The parameter identification process is done by comparing the measurements and simulation results and then, finding a set of parameters for nonlinear model using an estimator. This will be explained in detail in chapter 3 and will applied on proposed models. To get the simulation results, it is needed to solve the state equation of traction subsystems. In the following section, the state equation solving method used in this thesis is explained in detail.

2.4 Solving of state equations

In this chapter, four models of traction system component are proposed using bond graph methodology. This methodology helps us to extract the state equation of each model using energy links. The state equations are used to describe a system by a set of first-order differential equations using state variables. In this section, selected numerical methods for solve these differential equations are explained in detail.

2.4.1 Numerical Methods for Differential Equations

The basic first-order differential equation is as following:

$$\dot{y}(t) = f(t, y(t)) \tag{2.63}$$

To solve the simple differential equations, it is possible to have formal form solutions [122] (Appendix A.5 (equations (A.5.1) -(A.5.2))). However, most of differential equations in different applications are so complicated and there is no form of solution. Numerical integration method is a powerful tool for solving the differential equations. There are several types of integration method [123]. In our case, it is needed to have the methods which are low-order, fix step and gives the accurate results rapidly by choosing the accurate time steps. Therefore, three methods presented below are chosen.

- Euler method
- The trapezoidal method
- Heun method

These methods are explained in the following.

2.4.1.1 The Euler method

The Euler method was formed by Leonhard Euler in 1768 [123] which is nowadays the basic of all the advanced numerical methods. It is a simplest method compare to the other integration

methods. This method is not an efficient numerical method, however, the most of involved ideas in the numerical solution of differential equations can be simplified with it. Based on Euler method, the integration of an equation like (2.63) would be as below (Appendix A.5 (equations (A.5.1) -(A.5.3)):

$$y_{n+1} = y_n + hf(t_n, y_n), \qquad 0 \le n \le N-1 \tag{2.64}$$

After sufficient number of steps, the final step T is reached. The initial value of $y(t)$ can be achieved empirically or some close approximation of Y_0. The discrete point of $y(t)$ and approximate initial value lead us to have some error. These aspects affect the consistency and stability of numerical method. Figure 2-38 shows the geometric illustration of Euler's method.

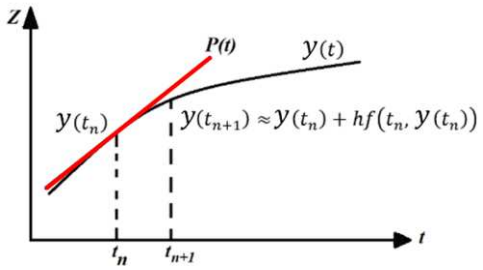

Figure 2-38 Geometric illustration of Euler's method

$P(t)$ is tangent to the graph of $y(t)$ and at t_n, it has slope of $y'(t_n) = f\big(t_n, y(t_n)\big)$. The tangent line is used to approximate the curve point at $\big(t_n, y(t_n)\big)$ (Appendix A.5, equations (A.5.7)).

2.4.1.2 The Trapezoidal method

Based on the trapezoidal rule, the graph of $G(t)$ in figure 2-39 is approximated on [a, b] by a linear function like $P_1(t)$. $P_1(t)$ interpolates $G(t)$ at the endpoint of [a, b]. Then the integral of $G(t)$ in the period of [a, b] can be approximated by the integral of $P_1(t)$ at the same period. Figure 2-39 illustrates this rule.

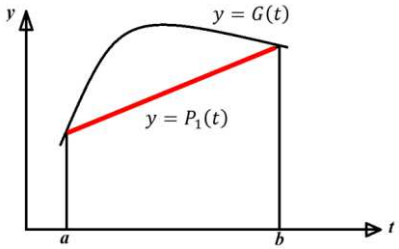

Figure 2-39 Geometric illustration of Trapezoidal method

The approximations and detailed explanations about trapezoidal method is presented in Appendix A.5 (equations (A.5.8) -(A.5.10)). The trapezoidal final method presented in Appendix (A.5.11) is an implicit method and this integration solution of $y(t)$ can be rewritten as bellow generally:

$$y_{n+1} = y_n + \frac{h}{2}[f(t_n, y_n) + f(t_{n+1}, y_{n+1})] \tag{2.65}$$

where h is the time interval. Note that, to start the simulation, it is required to have the initial value of $y(t)$. In this thesis, this method is used to do the integral calculation on the experimental measurements.

2.4.1.3 The Heun method

As explained in section 2.4.1, the basic idea of Euler method is to use tangent line as an estimation of the curve. In practice, over a large number of steps the error starts to accumulate due to this kind of estimation. Ideally, it is desired to estimate the curve by prediction line (as shown in figure 2-40) instead of tangent line.

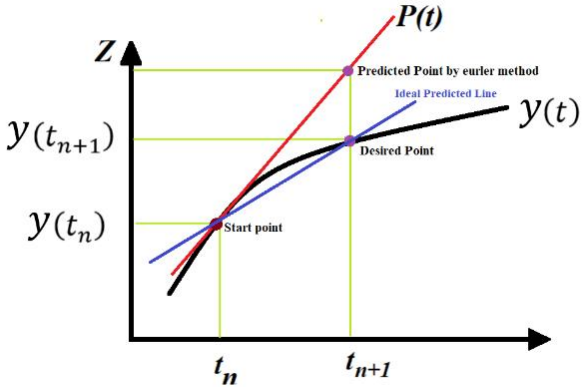

Figure 2-40 Geometric illustration of Euler method and prediction line

To solve this problem, Heun method addresses this correction requirement. Heun's methodology is to consider the tangent line to the solution curve at both ends of the interval that we are investigating. Figure 2-41 depicts the geometric illustration of two tangent lines in both ends. The tangent line in the right side ($P_1(t)$) overestimate the desired point and the left tangent line ($P_2(t)$) underestimate the desired point. The basic of Heun method is to use the prediction line whose slope is the average of the slopes of the tangent lines at either end of the interval.

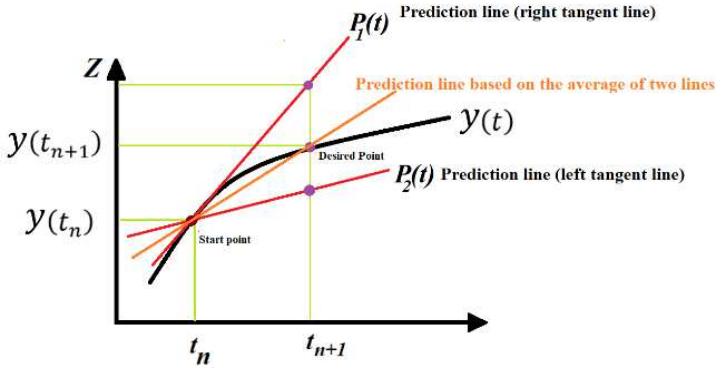

Figure 2-41 Geometric illustration of Heun method

Therefore, considering basic of Euler method and ideal slopes, (Appendix A.5 equation (A.5.12) -(A.5.13)) the iterative formulas for Heun method is as equation (2.75). This equation has second-order accuracy.

$$y_{n+1} = y_n + \frac{h}{2}[f(t_n, y_n) + f(t_{n+1}, y_n + f(t_n, y_n))] \tag{2.66}$$

Let us consider a linear state equation as below:

$$\dot{Y}(t) = AY(t) + BU(t) \tag{2.67}$$

where $U(t), Y(t)$ are input signal and state variable respectively. A and B are the multiplied coefficients. To have simple notation of equation (2.67), it can be defined as below:

$$Y_{n+1} = Y_n + \frac{h}{2}[K_1 + K_2] \tag{2.68}$$

where,

$$K_1 = f(t_n, Y_n) = AY_n + BU_n \tag{2.69}$$

$$K_2 = f\big(t_{n+1}, y_n + f(t_n, y_n)\big) = A(Y_n + hK_1) + BU_{n+1} \tag{2.70}$$

These expressions are used to the integration of all state equations presented in this chapter.

2.5 Conclusion

Considering the limitations of traction system model on real time simulator explained in the first chapter, developed model of four considered components of traction system are proposed, in this chapter. The common model limitation between these four elements are nonlinearity which were not considered in previous models. To improve these four models, methodology of bond graph is chosen which represents all energy transfer from input source to different elements of system using energy links. It is also explained how to establish the state equations of the system based on the causality analysis of generalized variables.

As a first element, an improved model of asynchronous motor is proposed considering nonlinear magnetizing inductance. A model is proposed to simulate its nonlinear behavior. As a second phenomenon, pantograph bounce behavior is modeled inside complete input power chain including substation, catenary and nonlinear transformer. The electrical arc nonlinear behavior is considered as variable resistance depending on the disconnection length between pantograph and catenary, and airflow speed.

The developed model of transformer considering nonlinear behavior of magnetizing inductance is proposed as a third approach. In this model, nonlinear behavior of magnetizing inductance is proposed by two different methodologies; hysteresis behavior using rewritten Jiles-Atherton model and modeling of its characteristics in deep saturation condition.

As a fourth approach, the simple model of Proton Exchange Membrane Fuel cell is improved. Its electrical model is proposed considering electrochemical phenomena which effect the steady and transient behavior of output voltage. All state equations considering the nonlinear characteristics of four models are proposed using bond graph methodology in detail.

To solve the state equations proposed for four models, different methodologies of numerical integrations are explained in detail. The methods of *Euler, Trapezoidal* and *Heun* which will be used in our case are expressed precisely.

All these proposed models require several parameters which have to be identified based on experimental results. Next chapter, the procedure of parameter identification is explained in detail and a similar method is applied on all proposed models. The methods and analysis are proposed to have simple process of identification in the case of ideal experimental test and results.

Chapter 3

Parameter identification and comparison with measurements

3.1 Introduction

In chapter 2, nonlinear behaviors of traction system components were considered to overcome the non-accuracy of real-time simulator explained in chapter 1. The bond graph methodology was used to illustrate the whole system, including nonlinear phenomena. It allowed us to have a better understanding of energy transfers in the subsystems and then obtain state equations of each subsystems. The provided steady state equations can be applied on the real-time simulator using numerical integration methods.

The nonlinear model of components provided in chapter 2 includes several parameters which have to be identified. In the following, the identification process is done by comparing simulation results and system measurements. In this chapter, the parameter identification process and selected methods are explained in detail. Then, the determined method is applied on the proposed model of desired subsystems of the traction system. As a final step, the results are compared with subsystem measurements, obtained either on specific test benches or trains, to validate the proposed models and identification process.

3.2 Parameter estimation and estimator

Parameter estimation refers to a process of using system response to estimate parameters of proposed model. In order to validate or determine parameters of the developed model, it is necessary to have measurements. Then, by exciting the same input to the system and model, the computed results and system response have to be compared. As it is shown in the block diagram of figure 3-1, the optimal set of parameters are determined for the numerical model by minimizing the difference between the output of system and model output.

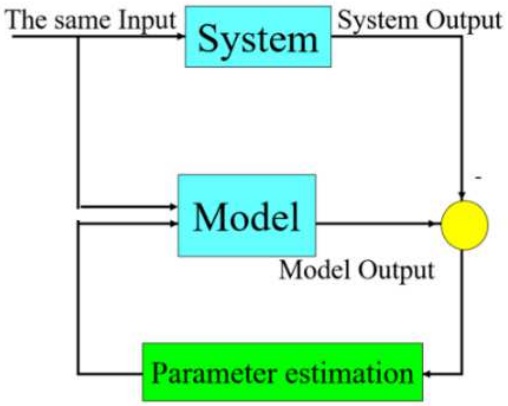

Figure 3-1 Parameter estimation architecture [124]

The techniques used for estimation are called estimators. There are several type of parameter estimators such as maximum likelihood estimator (MLE) [125], maximum pseudo-likelihood estimator (MPLE) [125], method of moments (MOME) [126], Minimum Mean-Square Error (MMSE) [127] and differential evolution (DE) method [128] which is used in this thesis to the

parameter fitting for subsystem models. This method is selected due to its few control variables through the entire minimization process and its good convergence properties.

To find out the optimum set of parameters, DE algorithm starts with a population of candidate for model parameters which is called agents. These agents are moved around the search-space (which is defined before starting the optimization) using a simple mathematical formula (cost function). The cost function for DE method is obtained by minimizing the summation of the difference, between desired and calculated system output. The cost function is:

$$\varepsilon = \sum_{j=1}^{N} \left((f)_{j,M} - (f)_{j,S} \right) \tag{3.1}$$

where ε represent sum of error, $(f)_{j,M}$ is the measured function of system, $(f)_{j,S}$ is the calculated function by simulation and N is number of input data vector. If the new position of agents is an improvement (having lower sum of error) then it is accepted and forms a part of population, otherwise, the new positions will be discarded [129] and [130]. This procedure is repeated several times until finding a satisfactory set of parameters. In this thesis, an internal software is used do the optimization using DE algorithm by setting two important parameters: number of population and number of evaluations. These two parameters indicate the number of iterations which has to be done within optimization process. This method is applied on the four developed model depicted in chapter2. Then, model parameter values will be optimized regarding the cost function.

3.3 Parameter identification, simulation and comparison with measurements

3.3.1 Asynchronous motor model

3.3.1.1 Identification of magnetizing inductance model parameters

As it is mentioned in chapter 2, the nonlinear magnetizing inductance in ASM varies by rotor flux variation (which has relation with speed variation). Let us remind that the proposed equation (2.8) has three parameters (a, b and c) which have to be identified using datasheet information. The nonlinear equation of magnetizing inductance is mentioned again as below:

$$L_m = \frac{\left| \emptyset_{r_{p.u}} \right|}{\left(\frac{1}{c}\right)\left(a \left| \emptyset_{r_{p.u}} \right| + (1-a) \left| \emptyset_{r_{p.u}} \right|^{b} \right)} \tag{3.2}$$

In this case the input is rotor flux proposed by the datasheet using FEM simulations. The output of (3.2) is compared with the measured one. Therefore, $(f)_{j,M}$ is the magnetizing inductance proposed by datasheet and $(f)_{j,S}$ is the calculated one by (3.2). The target error ε is set to ensure a relative error less than 1% for operating points given by the datasheet. Considering the

datasheet information about magnetizing inductance as figure 3-2, the adapted parameters can be easily obtained using DE method of estimation.

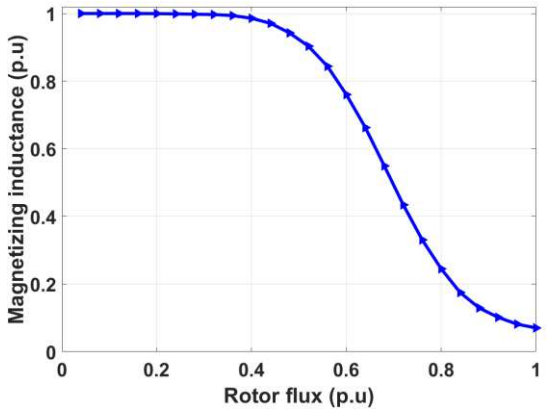

Figure 3-2 Magnetizing inductance based on the datasheet

The optimization is started with 10 for number of population and 100 for number of evaluations. As a matter of facts, 1000 number of iterations are applied. The results of parameter identification are shown in Table 3-1.

Table 3-1 Identified parameters of magnetizing inductance equation

Parameters	Values
a	0.68
b	8.78
c	0.005116

Once parameters are obtained, the magnetizing inductance model is simulated by applying the absolute value of rotor flux in datasheet as the input. Figure 3-3 depicts the comparison of simulation results and datasheet information for magnetizing inductance.

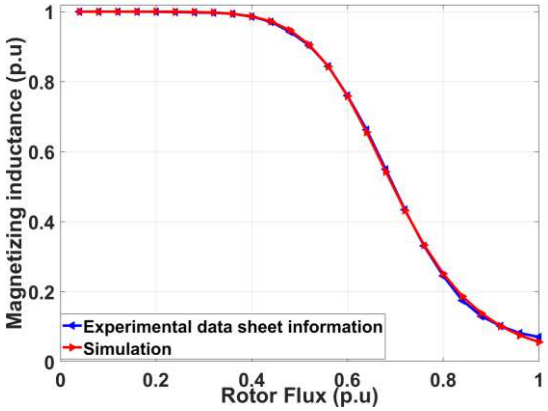

Figure 3-3 Comparison of simulated magnetizing inductance and the datasheet information

It is shown in figure 3-3 that the proposed equation is enough accurate to provide the value of magnetizing inductance in different operating points.

3.3.1.2 Comparison of simulation and measurements

Now, it is needed to validate the proposed model of ASM with the nonlinear magnetizing inductance by comparing with the measurements. The test bench results of regional train in Alstom applications is selected. The whole traction system is supplied by a DC source of 1500V. The DC source is connected to a preload circuit to avoid the voltage overshoot and then it is connected to a low pass filter. The DC voltage has to be converted to AC voltage to supply the motor. The voltage conversion is done by the inverter. Depending on the operator demand of traction or braking, the techniques of voltage conversion and parameters of modulation are different. The control command system applies the parameters corresponding to the pulse width modulation technique to the inverter to convert the DC to AC voltage with specific value of stator voltage and/or frequency to change the speed and minimize the harmonic components. The block diagram of traction system under test is shown in figure 3-4.

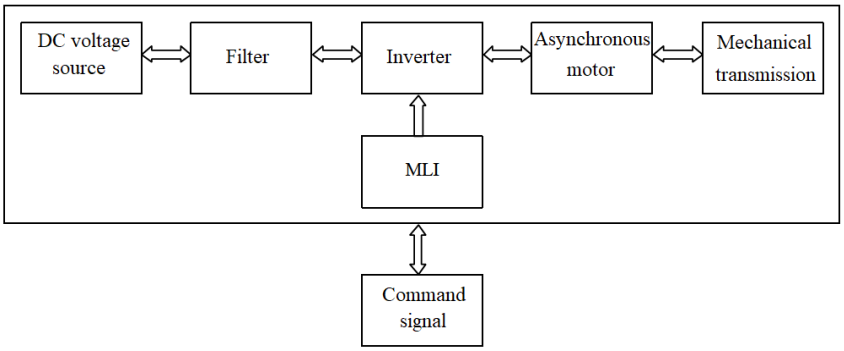

Figure 3-4 Traction system with DC voltage supply

By applying different operating points on traction system on test bench, the stator and rotor flux and current change. Consequently, the magnetizing inductance value could be different based on datasheet information. To do the comparison, different operating points are applied on test bench: 80, 130, 135 and 150 km/h.

Note that the percentage of effort demanded from driver desk to traction system by handle or manipulator is 100%. The effort value in motor level is controlled by the percentage of manipulator (0-100%) and speed. In fact, motor drive control system generates the fundamental voltage magnitude and frequency via inverter to create the required effort level on the motor. By applying the selected operating points on traction system in test bench, the AC voltage of inverter and stator voltage are registered simultaneously.

The simulation is launched to do the comparison with measurement. The proposed model of ASM including nonlinear model of magnetizing inductance is simulated using the identified parameters. The input of simulated motor is the measured AC voltage of inverter on test bench. The simulation results are obtained using state equations (2.2) and (2.3) and inverse Clarke transformation to have stator current in phases. Then, it is compared with the measured one on steady state condition. Figure 3-5 depicts the simulation environment.

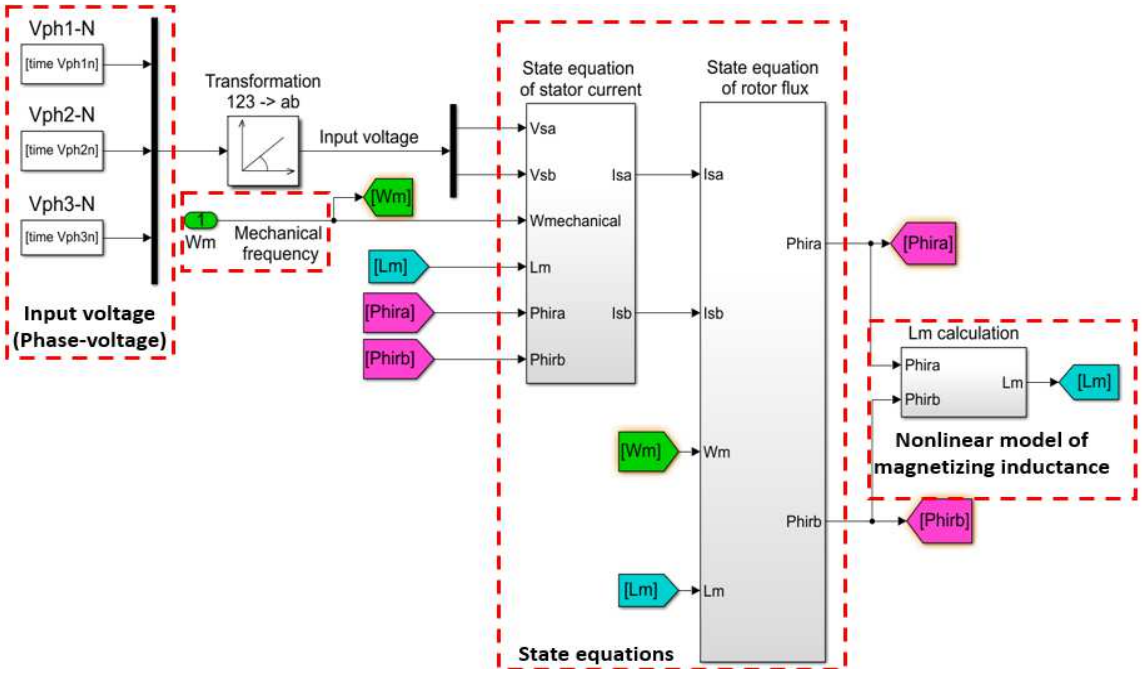

Figure 3-5 Simulation environment

As it is shown in the simulation environment in figure 3-5, the calculated rotor flux in α and β axes are the input of magnetizing inductance subsystem. In this block (namely L_m calculation in figure 3-5), the absolute value of rotor flux is calculated and united by nominal value. Then, the magnetizing inductance value is calculated using the equation (3.2). The absolute value of rotor flux is different for each operating point.

Note that simulation is done in two conditions: old model of ASM with constant magnetizing inductance and proposed model of ASM with nonlinear magnetizing inductance presented in chapter 2. The constant value of ASM magnetizing inductance is obtained based on the datasheet information (the magnetizing inductance while the absolute value of rotor flux is close to zero or while there is no demand of effort). Notice that this constant value is considered for magnetizing inductance in the old model of ASM in the beginning of the thesis. For the proposed model ASM, the magnetizing inductance is calculated using the state variables as shown in figure 3-7. Let us remind that magnetizing inductance changes by the united absolute value of rotor flux ($\left|\frac{\emptyset_r}{\emptyset_{nominal}}\right|$). As the absolute value of rotor flux changes for each operating point, therefore, the magnetizing inductance would be different for each operating point. This means that by applying an input voltage for one operating point, its value is constant, even if the magnetizing inductance is calculated for each sampling time. This is due to the fact that absolute value of rotor flux is constant for each operating point. The required information of motor parameters for simulation such as stator resistance, rotor resistance, stator leakage inductance and rotor leakage inductance can be obtained by datasheet. Table 3-2 depicts the comparison of measured stator current on fundamental frequency on test bench and the

simulated one while the magnetizing inductance is constant and nonlinear one. Note that the provided values are united by nominal current of ASM mentioned in datasheet.

Table 3-2 Comparison of amplitude of stator current on fundamental frequency

Speed km/h	Stator current on fundamental frequency (p.u)		
	Test bench	Simulation (L_m ($\emptyset_r$))	Simulation ($L_m = L_{m_0}$)
80	1.026	0.992	0.913
130	0.807	0.777	0.713
135	0.735	0.711	0.636
150	0.6412	0.63	0.613

For better visual representation of comparison results and errors between measurement and simulation, the figure 3-6 is provided.

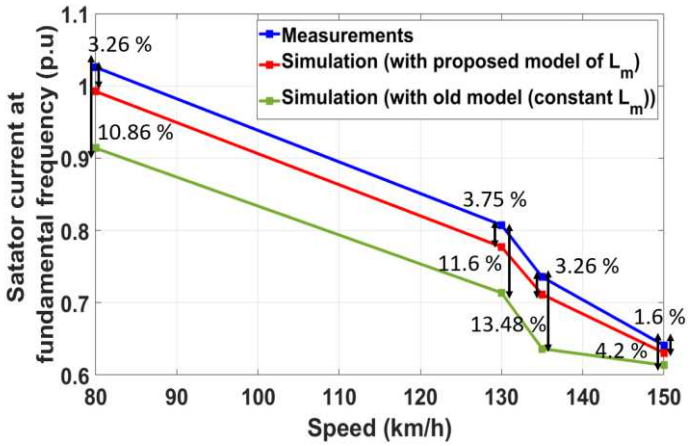

Figure 3-6 Comparison of stator current on fundamental frequency on test bench, simulation with and without nonlinear model of magnetizing inductance

Thanks to the model of magnetizing inductance, the difference between measurements and simulation of stator current in fundamental frequency is reduced about 7% in the average of all operating point.

Based on the simulation results, the magnetizing inductance using the nonlinear model is changed for each operational point as Table 3-3.

Table 3-3 Magnetizing inductance variation for different operational points

Speed (km/h)	Magnetizing inductance (L_m ($\emptyset_r$))
80	4.6 mH
130	5.137 mH
135	5.337 mH
150	6.116 mH

Note that the in the previous model of ASM, the magnetizing inductance is constant and equal to 7.5 mH. This result illustrates the necessity of considering magnetizing inductance variation in simulation as depicted in this thesis.

3.3.2 Pantograph bounce

3.3.2.1 Parameter identification of the nonlinear arc model

As it is explained in chapter 2, the electrical arc has nonlinear characteristics which can be obtained using (2.22) which are highlighted again as below:

$$R_{arc}(t) = \frac{1}{g_{arc}(t)} = \frac{1}{g_c(t)} + \frac{1}{g_m(t)}$$

$$\frac{dg_m}{dt} = \frac{1}{\tau_1}\left[\frac{I_p(t)^2}{P_0(t)} - g_m(t)\right]$$

$$\frac{dg_c}{dt} = \frac{1}{\tau_2}\left[\frac{I_p\,(t)^2}{u_c(t)^2 g_c(t)} - g_c(t)\right]$$

with,

$$u_c(t) = CL_{arc}(t)$$

$$P_0(t) = \begin{cases} kg^{\beta}L_{arc}(t)^n & if \quad v < v_0 \\ L_{arc}(t)bk_1(v+a)\sqrt{I_p} & if \quad v \geq v_0 \end{cases} \tag{3.3}$$

Based on these equations, the parameters of model such as $k, \beta, n, k_1, v, v_0, a$, b and C which are the coefficient of pyroelectric, the power constant of arc dissipation, undetermined arc parameter, correlation coefficient of dissipated power for arc, speed of train and specific value of train speed, arc coefficients respectively have to be identified. To do so, it is required to have measurements of arc phenomenon.

3.3.2.2 Comparison of simulation and measurements

In our case, a specific test is done on train close to the substation and moving in very low speed (less than 10 km/h). The test is developed on Alstom high speed train project (figure 3-7).



Figure 3-7 high speed train developed in Alstom transport

The substation provides a power grid of frequency 16.2/3 Hz and rms voltage of 15 kV for train. The pantograph is connected to catenary to transfer the substation voltage to train traction system. Once the traction system is in steady state, the pantograph is disconnected from catenary quickly and it is reconnected to catenary slightly. Therefore, the electrical arc can be captured in reconnection time. The pantograph maximum disconnection length is about 5 cm. [131]. The impact of electrical arc on the measured primary voltage of transformer is depicted on figure 3-8.

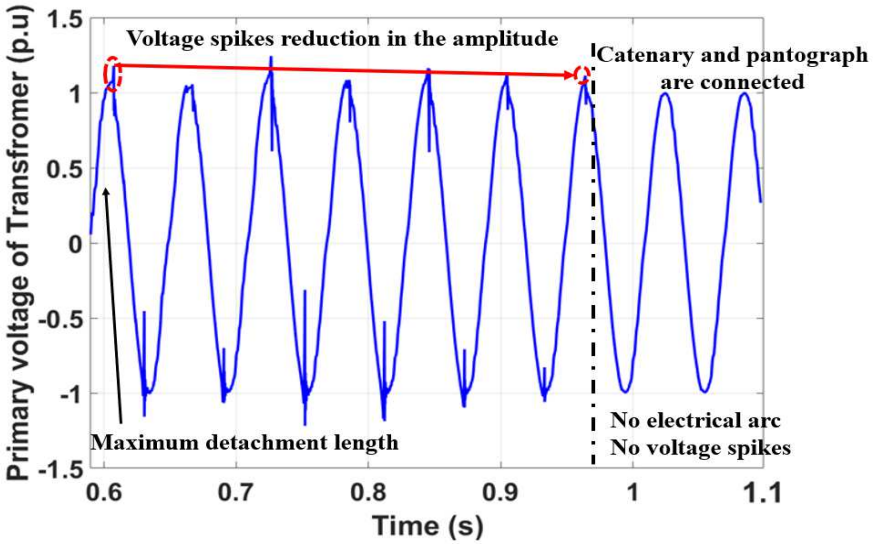

Figure 3-8 Measurements on voltage of input power chain

It can be seen that the voltage spikes due to the electrical arc, started from 0.6 s and it is finished around 1s. As it is explained in last paragraph the detachment length is decreasing in this time interval. The less detachment length exists between catenary and pantograph, the less voltage spikes amplitude appears on the primary voltage of transformer. Figure 3-8 depicts the reduction of voltage spikes on each period. It is also seen that voltage spikes are disappeared while there is no disconnection between catenary and pantograph (after 1 second). The simulation of whole input power chain is developed using state equations (2.13)- (2.16) presented in chapter 2. As the train is in very low speed (less than 10 km/h), the arc model follows equation (2.22) considering dissipated energy as equation (2.21) in low speed condition. The disconnection length is obtained using ramp equation proposed in chapter 2. As the arc phenomenon is captured only in the reconnection level, the arc drawn step has to be considered in $L_{arc}(t)$ equation.

The simulation environment is shown in figure 3-12. As it is in figure 3-9, the substation voltage (U_E) while it is not impacted by arc phenomenon is applied as system input.

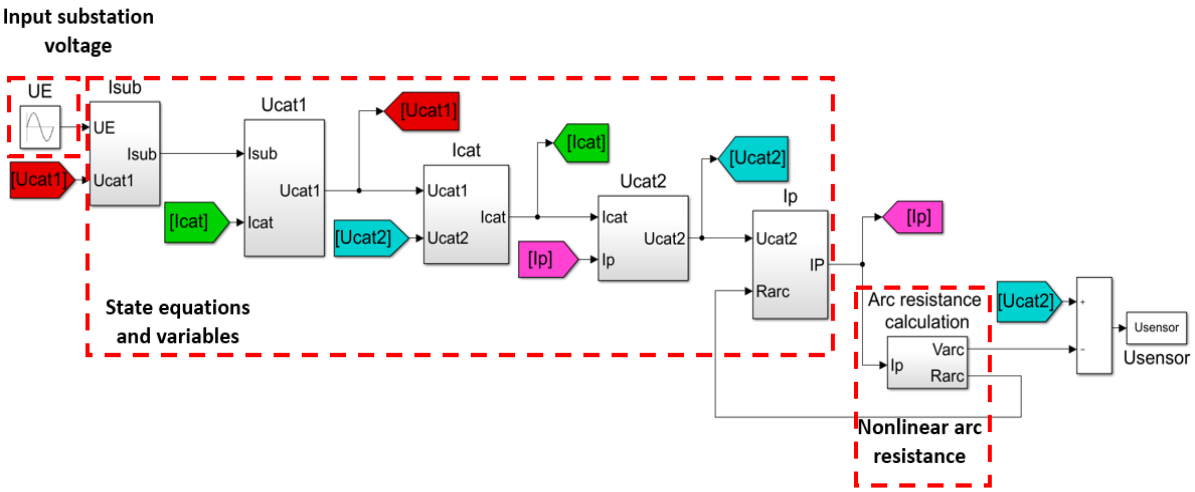

Figure 3-9 Simulation environment for pantograph bounce model

As it is shown in simulation environment, the calculated $I_p(t)$ is an input of nonlinear model of electrical arc. The system output is the voltage measured by the sensor (U_{sensor})provided in the primary of transformer. The provided voltage of sensor calculated by subtracting the catenary voltage (U_{cat_2}) from the calculated electrical arc voltage ($V_{arc}(t)$). This is due to the fact that electrical arc reacts as a resistance which decrease the catenary voltage ($U_{cat_2}(t)$) by passing the current ($I_p(t)$).

To do the identification of parameters, the experimental arc voltage is extracted by subtracting the measured voltage from the input power chain and the waveform from the stable voltage in one period (a few cycles just after the arc phenomenon (the time interval between $t = 1.01s$ and $t = 1.07s$ in figure 3-8)). The arc voltage is considered as measurements and the arc parameters in proposed model are adapted using differential evolution method. Therefore, the functions used for optimization process $(f)_{j,M}$ and $(f)_{j,S}$ are voltage of arc (V_{arc}) in measurement and simulation, respectively. The optimization is started with 10 for number of population and 500 for number of evaluations. Therefore, 5000 number of iterations are applied. The target error ε is set to ensure a relative error less than 2%. The identified parameters are shown in Table 3-4.

Table 3-4 The identified parameters of electrical arc

Parameters	Values
C	15
β	1
k	35000
n	0.5

Note that due to the experimental constraints, it is not possible to have the recorded measurements on high speed condition. Therefore, the other parameters related to the dissipated energy in high speed case (k_1, v, v_0, a, b) are not identified. This can be done as a future approach.

The comparison of arc voltage between simulation and measurements are depicted in figure 3-10.

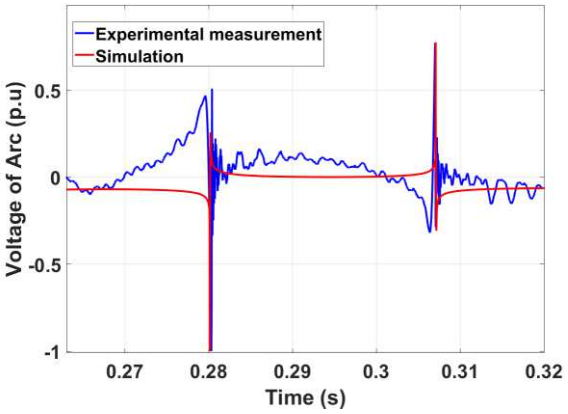

Figure 3-10 Comparison of arc voltage in measurement with simulation one

Once the parameters are obtained, the primary voltage of transformer on simulation can be compared with measurements. Figure 3-11 shows the comparison results.

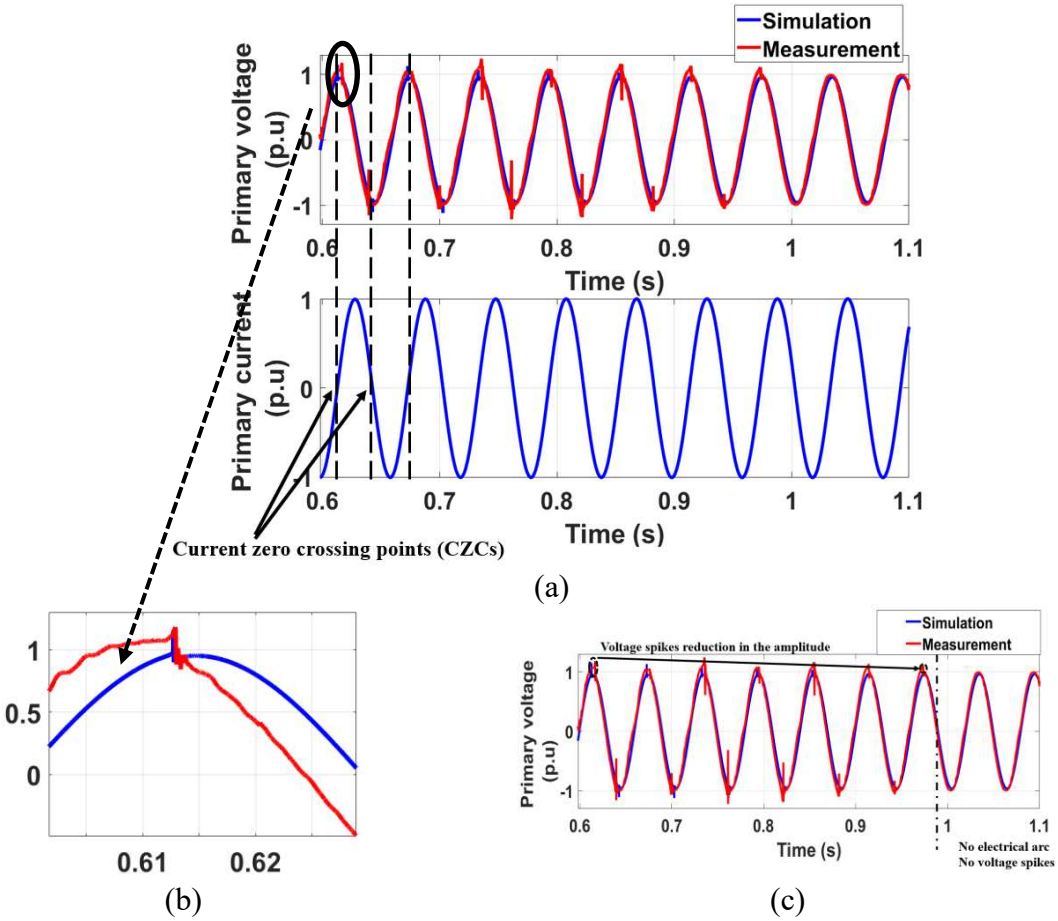

Figure 3-11 Primary voltage of transformer on train and simulation in presence of arc phenomenon

As it is depicted in figure 3-11 (a), there are two voltage spikes per period due to the zero-crossing point of current. The zero crossing points that creates the voltage spikes on the primary

voltage are perfectly predicted (figure 3-11 (a)) thanks to modeling of the whole power chain. As it is shown in figure 3-11 (b), the amplitude of voltage spikes obtained in the simulation are close to measurements by relative error less than 2% which is acceptable in industrial point of view (less than 5% of error). The reduction of voltage arc (spikes) as a function of disconnection length is in good agreement with measurements thanks to the disconnection length ($L_{arc}(t)$) model presented in chapter 2, (figure 3-11 (c)). It can be seen that effects of arc phenomenon on primary voltage of transformer in simulation is representative of measurements on train. Due to the parameters of measurements such as sample time, the comparison of spikes in high frequency oscillations is difficult. However, this is balanced by the fact that the worst effect of arcing lies in the values of spikes that can induce overvoltage and then damages in the traction system.

3.3.3 Nonlinear power transformer

The nonlinear model of power transformer in railway application is proposed in chapter 2. The magnetizing inductance characteristics are modeled based on Jiles-Atherton model. The JA model is rewritten, and some measurements are defined to help parameter identification. The rewritten JA model helped us to avoid the algebraic loop problems in the simulation. It is described that JA model is representative enough for magnetizing current in steady and transient state (having inrush current). However, characterization of magnetizing inductance using measurements provides better representativity for deep saturation region. Note that the deep saturation condition of transformer is determined as highest value of inrush current (1.5-2 times more that nominal current of transformer) in transient state. Therefore, a final model is proposed using both methodologies to provide a complete model of magnetizing inductance in deep saturation, transient and steady state regions. As an initial proposition, it is considered to use the method JA while the first peak of primary current is less than nominal current of transformer. Otherwise, the final model which is combination of JA model and curve fitting method has to be used. Figure 3-12 depicts the preference of proposed models in simulation as an initial proposition or hypothesis of this thesis that should be approved.

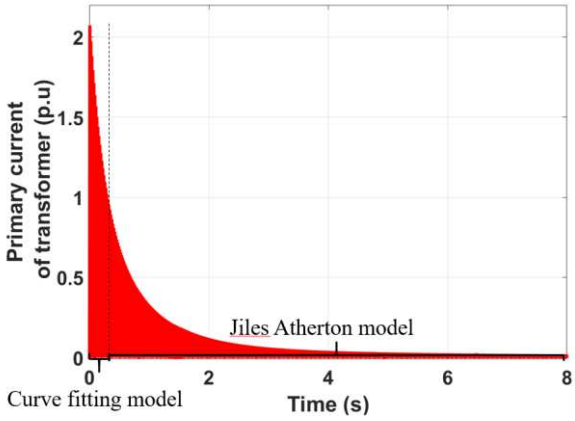

Figure 3-12 The preference of two methodology of magnetizing inductance model

In the following section, JA model parameters are identified using measurements. In order to estimate the JA parameters in the case of non-ideal test condition, specific analysis is done on parameter identification just by part of a hysteresis cycle (section 3.3.3.1). The proposed identification process is applied to train measurements. The obtained parameters are then inserted into the overall system model. The consecutive simulations are compared to measurement data obtained through traction system test bench (section 3.3.3.2). Then, to characterize the nonlinear behavior of $B-H$ curve in deep saturation region, identification of parameters is done with polynomial equations (section 3.3.3.3). Finally, the proposed models for magnetizing inductance are confirmed by comparing the measurements and simulation in the case of having inrush current.

3.3.3.1 Jiles-Atherton parameter identification

As it is mentioned in section 3.2, it is required to have measurements of system to do the parameter identification. However, in industrial applications and in application where several components are embedded, it is not easy to have an ideal test condition. The test condition can be affected by nonlinear sensors for measurements, non-ideal environment condition and effect of other parts of traction system. Moreover, the accurate model is not often provided by the transformer designer. Nevertheless, in high power transport applications, it is important to be able to model and identify the model parameters on the component. This allows having simulation results close to measurements.

In last few years, different methods of parameter identification for JA model have been proposed. The traditional and known method is numerical determination as proposed in [132]. In [133], random and deterministic searches were done to perform the identifications. False position method is used in [134] as a method of parameter estimations for JA model. In [135], an alternative approach based on ‘‘branch and bound’’ optimization method is explained. A robust method to determine numerically the Jiles-Atherton model parameters is presented in [136]. These parameter estimations require no load test of transformer with an ideal test condition to have the complete hysteresis loop and in addition, the data sheet information to set the ranges for parameters. These test procedures are not easy to do in railway applications. Effectively, the presence of all traction system or non-ideal sensors during the no load test may alter the complete hysteresis loop monitoring. This may result to have uncomplete $B-H$ hysteresis cycle in having a part of the $B-H$ hysteresis cycle exploitable. Therefore, it is important to do the analysis on parameter estimation when the whole $B-H$ hysteresis cycle can not be provided.

In the following, the section is organized as follow: first, to illustrate the use of the JA model and its parameter identification, a first example taken from a previous study is considered [137]. In this previous study, a test with a transformer with no load condition is done to obtain the hysteresis characteristics and a simplified model of transformer is considered to obtain theatrically the parameters of JA model. In our approach, the parameter identification is done by part of a hysteresis cycle to analyze the estimation of JA parameters in non-ideal test

condition. Secondly, the study is applied to train test bench measurements in no load condition with an uncomplete hysteresis cycle.

3.3.3.1.1 Example of JA model parameter identification

The transformer model with the open secondary is modeled as depicted in figure 3-13.

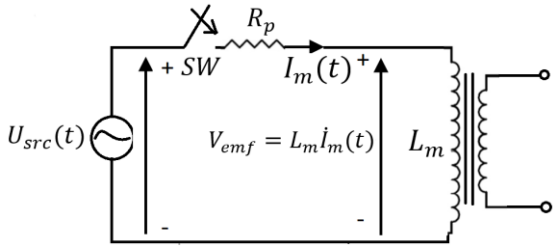

Figure 3-13 Model of transformer with no load.

The bond graph method is applied to obtain the state variable and equation. Consequently, the related state equation is:

$$\dot{I_m}(t) = \frac{U_{src}(t)}{L_m} - \frac{R_p I_m(t)}{L_m} \tag{3.4}$$

With:

$$L_m = \frac{N^2 S \mu_0 \left(1 + \frac{dM}{dH}\right)}{l} \tag{3.5}$$

In (3.5), $\frac{dM}{dH}$ expresses as in (2.48) and depends on state variable using (2.35), (2.36), (2.28), where Faraday's law (Appendix A.3 (equation A.3.9)) is replaced by (3.6).

$$\dot{B}(t) = -\frac{U_{src}(t) - R_p I_m(t)}{NS} \tag{3.6}$$

As our first wish is to validate the method, the parameters of electrical circuit and JA are considered based on data provided in [85] and summarized in Table 3-5. The simple transformer model is simulated where the magnetizing core characteristics are computed based on Appendix A.3 (equation A.3.10)) and (3.4)- (3.6).

Table 3-5 Transformer electrical magnetic parameters

Symbol	Values
M_{sat}	1497000
k	125.24
c	0.319
α	0.0008851
a	458.57

In [137], $M(H)$ characteristic of the magnetic material is under concern. However, our proposed modelling methodology based on bond graph and specific writing of JA equations lead us to recover the hysteresis characteristic $B(H)$ in figure 3-14 that is linked to $M(H)$ one. Note that B_r and H_c in the figure 3-14 represent the remanence and coercive field.

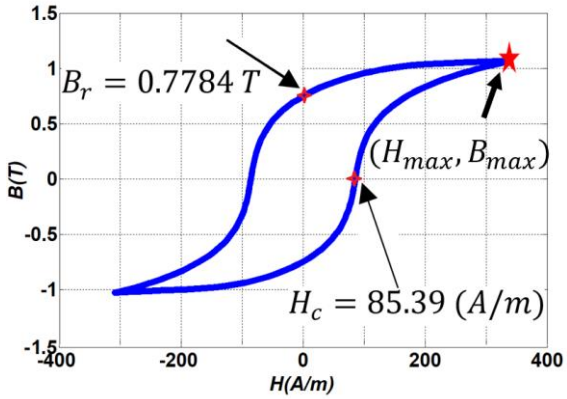

Figure 3-14 Hysteresis loop of transformer with the JA parameters in table I.

In subsections 3.3.3.1.2 and 3.3.3.1.4, parameter identification is done with the entire hysteresis loop and with a percentage of the hysteresis loop. The comparisons between these two study cases are proposed and discussed in the following.

3.3.3.1.2 Identification process with complete hysteresis loop

As a first step of identification, numerical determination method is used to identify the initial value of parameters as in [132]. Secondly, Differential Evolution (DE) method [128], [138] is used in order to do the parameter fitting for whole hysteresis loop of the transformer. The cost function for DE method (3.1) is achieved by $(f)_{j,M}$ and $(f)_{j,S}$ which are magnetizing current $I_m(t)$ in this case. The objective is to recover the JA model parameters $(\alpha, k, c, a, M_{sat})$ given in Table 3-5. The optimization is started with 500 for number of population and 100 for number of evaluations. As a matter of facts, 50000 number of iterations are applied. To set the initial values for every parameter some boundaries have to be fixed. The boundary of each parameter is considered between minimum and maximum values as provided in [85] and reported Table 3-6. This table depicts the selected boundaries for each parameter. Note that as in [132] and [85], M_{sat} is known for particular materials and so it can be obtained from datasheet or the references. It is constant for all analysis step.

Table 3-6 Boundaries of JA parameters used in simulation

Parameters	Boundaries
k	$\epsilon[61.23, 138.7] \Leftrightarrow \langle k \rangle \pm 38.7\%$
c	$\epsilon[0.048, 0.374] \Leftrightarrow \langle c \rangle \pm 43.5\%$
α	$\epsilon[0.0001634, 0.0009081] \Leftrightarrow \langle \alpha \rangle \pm 69.5\%$
a	$\epsilon[103.2, 474.6] \Leftrightarrow \langle a \rangle \pm 65\%$

The target error ε is set to ensure a relative error on $I_m(t)$ over a period lower than 1%. Table 3-7 shows the result of parameter identification for one entire loop of hysteresis.

Table 3-7 Parameters achieved by 100% of a period

Symbol	Differential Evolution	Relative error (Table 3-6) (%)
M_{sat}	1497000	-
k	126.97	1.37
c	0.32	0.03
α	0.000889	0.4
a	460.85	0.49

The relative error presented in Table 3-7 shows that the identified parameters values are close to those initially used and given in Table 3-6. Let us remind that M_{sat} is constant for all analysis step, therefore, the relative error is not provided in Table 3-7. That validates the identification method based on DE algorithm. Notice that, initial boundaries for the parameters are required to identify and are detailed in the following.

- Boundary Setup

Based on [135], the boundaries of JA parameters considering their physical definitions in [132] are as following:

$$\begin{cases} M_{sat} \in \langle M_{max}, 1.2M_{max} \rangle \\ a \in \langle 0.5H_c, 5H_c \rangle \\ k \in \langle 0.2H_c, 5H_c \rangle \\ \alpha \in \langle 10^{-10}, \frac{H_{max}}{M_{max}} \rangle \\ c \in \langle 0,1 \rangle \end{cases} \tag{3.7}$$

To set these boundaries, it is required to have maximum values of magnetization M_{max} which can be calculated by B_{max} and H_{max} ($M_{max} = \frac{B_{max}}{\mu_0} - H_{max}$) and coercive field H_c. Note that parameters obtained after identification process in last section are included in the boundaries defined in (3.7).

3.3.3.1.3 Identification process with uncomplete hysteresis loop

In transport application, it is sometimes difficult to get the complete hysteresis loop. To overcome this drawback, in the following, it is studied how to recover JA parameter identification by the use of a part of the hysteresis cycle. As a matter of facts, different percentages of one hysteresis period from 10% to 100% with a step of 10% are selected. Among these tests, Figure 3-15 shows four examples of selected data. The four study cases are: 80%,

60%, 40% and 20% of the entire loop. Note that, over a period, signals are constantly sampled regarding time. Every example has the same start point which is $(max(H), max(B))$.

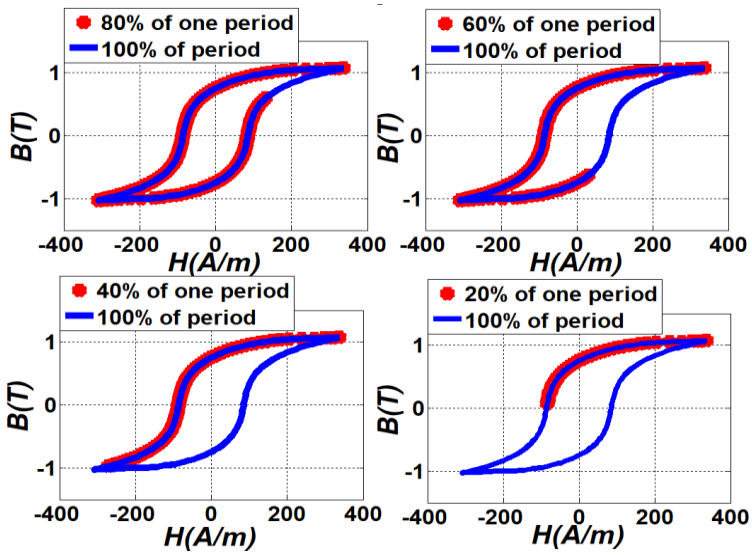

Figure 3-15 Uncomplete hysteresis loop (based on percentage of one period of hysteresis loop 20-40-60-80%)

The identification process of proposed example is repeated for every case of study. The DE parameters (number of evaluations, population and boundaries) are identical. The results are compared to the initial JA parameters shown in Table 3-5. Figure 3-16 shows the relative error of parameters for all percentage of hysteresis loop.

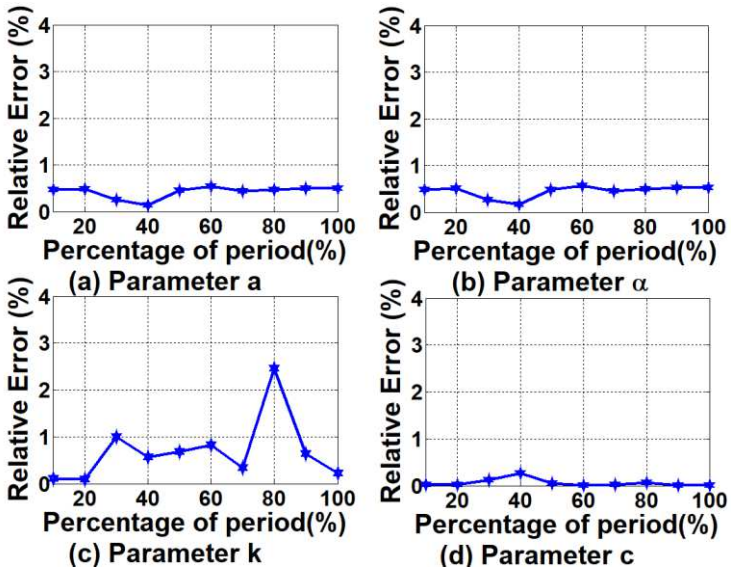

Figure 3-16 The difference of JA parameters achieved by percentage of period compared to initial JA parameters

It can be observed that the difference between each parameter achieved by percentage of period and those initially is less than 3%. Note that every percentage from 10% to 100% leads to the same conclusion. It means that in the case of an uncomplete hysteresis cycle, the identification

process can be done correctly even if there is only 10% of the hysteresis cycle. Figure 3-16 highlight the fact that the most sensitive parameter to identification process is *k*, figure 3-16 (c).

To validate the proposed approach, 2 main points in each hysteresis loop are compared to the initial ones. The points chosen are the coercive H_c and remanence points B_r. The initial points are computed where the magnetic induction is zero and where the magnetic field is zero. Figure 3-20 illustrates the relative error for coercive (H_c), remanence points (B_r). In the last curve (figure 3-17 (c)), the error is based on the hysteresis area produced by different percentage of one period of hysteresis loop compared to initial data.

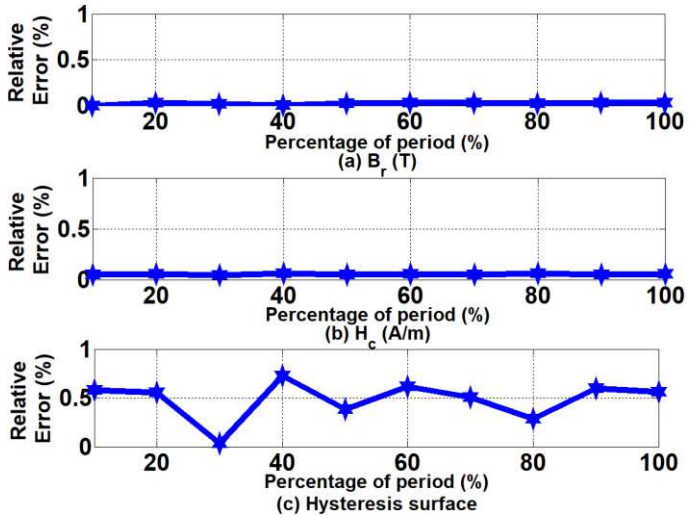

Figure 3-17 Relative error for coercive, remanence field and hysteresis area calculated for each hysteresis loop

As depicted in figure 3-17, the percentage taken for identification process has low impact on the error made on remanence and coercive fields. Note that the average error of about 0.5% made on overall hysteresis surface remains acceptable. Finally, the sensitivity on parameter *k* does not have a strong impact on final hysteresis characteristics. Note that, in this case, the start point for identification is the positive extreme value of hysteresis loop. In section 3.3.3.1.4, identification processes are done with different start points or different data selection in one period.

3.3.3.1.4 Identification process by the part of a signal period with different start points

In the following, the boundaries defined in (3.7) are considered and used for identification process. In this section, 20% of period is chosen. The impact of different start points as depicted in figure 3-18, is studied:

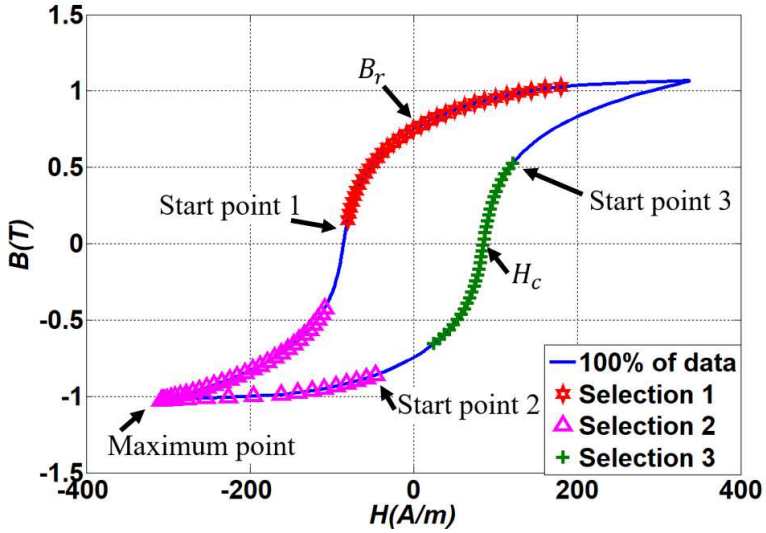

Figure 3-18 Uncomplete hysteresis loop with different start point for identification

The first and third selections include respectively remanence field B_r, and the coercive field H_c. But the maximum point of hysteresis loop is not included in these two selections. However, the second selection considered is taking into account the extremum point.

To do the analysis on the effect of start point on the results of parameters identification, two comparisons are done. The first comparison is done with the initial data in Table 3-5. The second one is achieved with identified data obtained for 20% of the hysteresis cycle in section 3.3.3.1.3. Table 3-8 and Table 3-9 present the relative error on each parameter.

Table 3-8 Relative error of JA parameters achieved by different start points compared to initial JA parameters

Parameters	Selection1	Selection2	Selection3
a	1.4%	0.051%	0.64%
k	19%	0.1%	40%
α	1.7%	0.078%	0.6%
c	25%	0.19%	45.5%

Table 3-9 Relative error of JA parameters achieved by different start points compared to JA parameters achieved by 20% of period

Parameters	Selection1	Selection2	Selection3
a	1.4%	0.0046%	0.68%
k	19.48%	0.0114%	66.9%
α	1.5%	0.073%	0.63%
c	33.7%	0.0615%	83.07%

The comparisons shown in Table 3-8 and 3-9 illustrates that the selection 2 including the extremum point of hysteresis cycle, has less error.

Hysteresis cycle area is also calculated for each selection case and is compared with the initial hysteresis cycle area, and the one achieved with parameters obtained with 20% of the signal period. The relative errors made on the hysteresis cycle areas are given in Table 3-10.

Table 3-10 Relative error of hysteresis cycle area

Compared with	Selection1	Selection2	Selection3
Initial Hysteresis cycle area	1.9%	0.0029%	6.37%
Hysteresis cycle area obtained by 20% of period	1.9%	0.01%	6.3%

It is concluded that the relative error made on hysteresis cycle area is the lowest when the percentage of period includes one of the extremum values of the hysteresis loop. Note that the data are sampled constantly regarding time. Based on the results shown in Table 3-8, 3-9 and 3-10, it is concluded that the parameter identification with uncomplete loop must be done with one of the extremum values of loop included in the selected part of the period.

3.3.3.2 Measurement and simulation results

- Hysteresis cycle and Magnetizing current

A test bench of a traction system developed for an ALSTOM railway project is used. The test bench includes a transformer (25kV/60Hz, of about 3MVA). The transformer is fed by a power source of frequency f=60Hz and rms voltage of 25kV directly. Electrical parameters of the transformer are given by its datasheet from the supplier and are synthetized in Table 3-11:

Table 3-11 Transformer electrical parameters

Symbol	Values
R_p	$0.0011\ \Omega/turn$
L_p	$0.535\ \mu H/turn$
R_f	$0.04\ \Omega/turn$

In order to have the hysteresis loop of transformer, the secondary of transformer is isolated by control command system to have no-load condition for transformer. Then, the contactor is closed by demand of operator. The mechanical contactor is closed by a specific delay of closure. The measurement is ceased once the steady state is achieved. The sensors used are the one already inserted for the control of the traction system. In this section, the test bench reproduces zero speed train behavior. Most of the parameters of the power input of the traction system are constant. Then, measured primary current $I_p(t)$ is provided in figure 3-19 in steady state. Note that currents are shown in per unit (p.u).

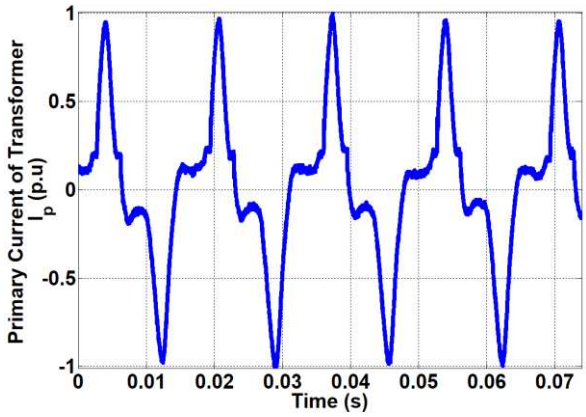

Figure 3-19 Measured primary current of transformer (I_p(A))

Using numerical trapezoidal integration [122] and (2.27), (2.33) and (Appendix A.3 (equation (A.3.4))), magnetic flux and magnetizing current can be computed by having measured primary voltage $U_{cat_2}(t)$ and current I_p (t) of transformer. Figure 3-20 (a) and (b) show one period of the steady state measurement of a voltage and current, respectively. Computed magnetic flux and magnetizing current are illustrated in figure 3-20 (c) and (d), respectively. Note that computing $I_m(t)$ needs the derivative of magnetic flux, then introduces high-pass filter, and finally, leads to an increase of high frequency noise.

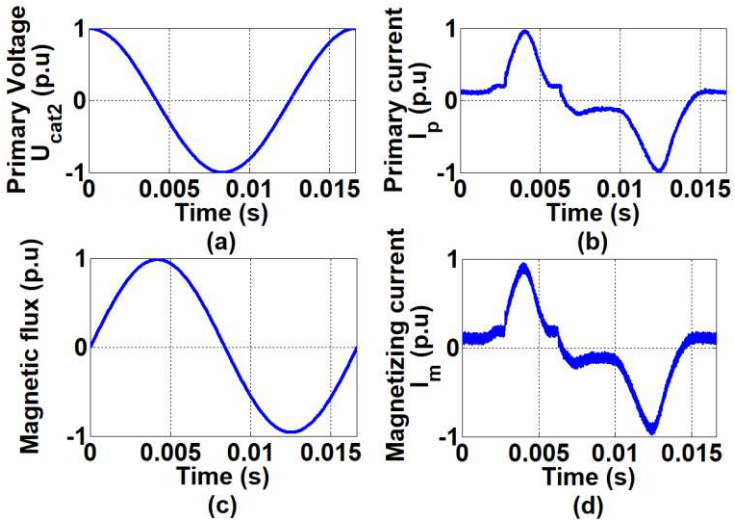

Figure 3-20(a) Measured primary voltage of transformer (U_{cat_2}), (b) Measured primary current of transformer (I_p), (c) Calculated magnetic flux of transformer ($\emptyset_m$) and (d) Calculated magnetizing current of transformer (I_m)

Due to the nonlinear characteristics of sensor, there is less accuracy in low value of current. As the sensor is designed to measure inrush current and full load current, there exists an error. This is due to the great difference between the maximum rating of the sensor and the maximum value of the measured primary current in steady state and no-load condition. Consequently, the current is deformed, and nonlinearities exists.

To estimate the hysteresis loop of desired transformer, it is required to compute the magnetic field and magnetic induction through previous variables (Faraday's law (Appendix A.3 (equation A.3.9))), (Ampere theorem (Appendix A.3 (equation A.3.10))). The corresponding hysteresis loop is depicted in figure 3-21 (a). In order to perform an accurate identification process, the signal is filtered by a nonlinear median filter of even order. The filtered signal is shown in figure 3-21 (b).

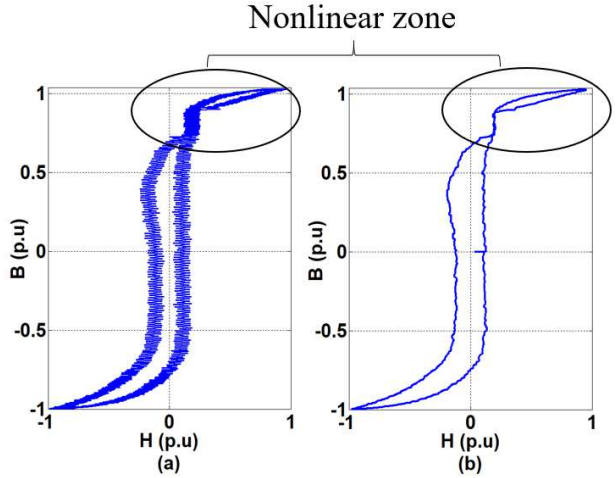

Figure 3-21(a) Computed hysteresis cycle using measurements ($B-H$), (b) Filtered hysteresis cycle.

A transient state appears on filtered hysteresis loop due to the numerical filtering. Therefore, we do not have a symmetric and complete hysteresis loop. Based on analysis done in section 3.3.3.1.1 and in section 3.3.3.1.3, a part of hysteresis cycle including the coercive field value and the extremum of the hysteresis loop is necessary for parameters identification. In our case of study, two parts of hysteresis which are not affected by nonlinearity of sensor are selected. These two parts represent 30% of the whole hysteresis cycle with and without extremum point (shown in figure 3-22).

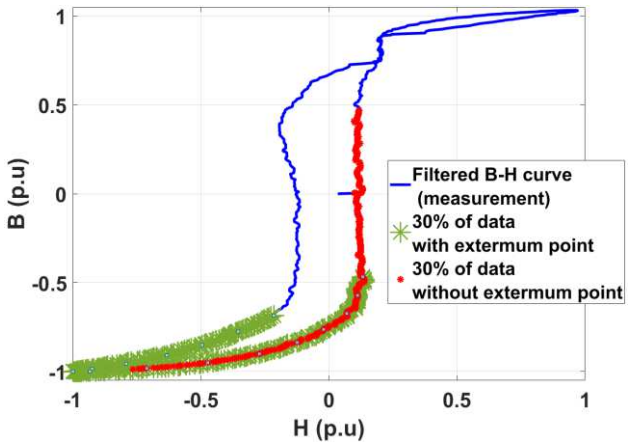

Figure 3-22 two selected part of hysteresis cycle with and without extremum points for identification process

All the procedure of identification is done as in sections 3.3.3.1.2-4, numeric values for H_c, H_{max} $M_{max} = \frac{B_{max}}{\mu_0} - H_{max}$ and JA parameters of equation (3.8) are obtained.

$$\dot{I}_m(t) = \frac{l.U_l(t)}{N^2 S\mu_0 \left(1 + \frac{\frac{cdM_{an}}{dH_e} + \frac{\delta_m(M_{an}-M)}{\delta k - \frac{\alpha(M_{an}-M)}{1-c}}}{1 - \frac{\alpha c dM_{an}}{dH_e}}\right)} \tag{3.8}$$

Thanks to the identification procedure, Table 3-12 shows the parameters of JA model obtained considering two different mentioned parts of hysteresis cycle.

Table 3-12 Identified JA parameters

Symbol	Values (with extremum point)	Values (without extremum point)
M_{sat}	11305398.6	11305398.6
k	69.55	221.55
a	102.4	122.4
α	0.00026786	0.0002579
c	0.2296	0.7996

Figure 3-23 shows the comparison between measurement and simulated hysteresis cycles. Parameters in Table 3-12 are used in simulation. The simulation using the parameters obtained by part of hysteresis cycle with extremum point is in good agreement with experimental data, figure 3-23.

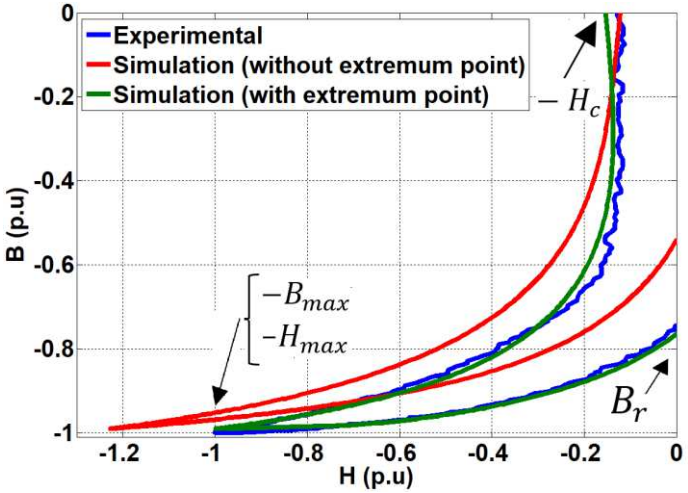

Figure 3-23 Comparison of measurement and simulated hysteresis cycles

Figure 3-24 confirms the conclusion of section 3.3.3.1.4: having the extremum point is necessary for an accurate identification process. To confirm the whole model proposed in this section, the simulated primary current is also compared with the measured one on test bench, Figure 3-24.

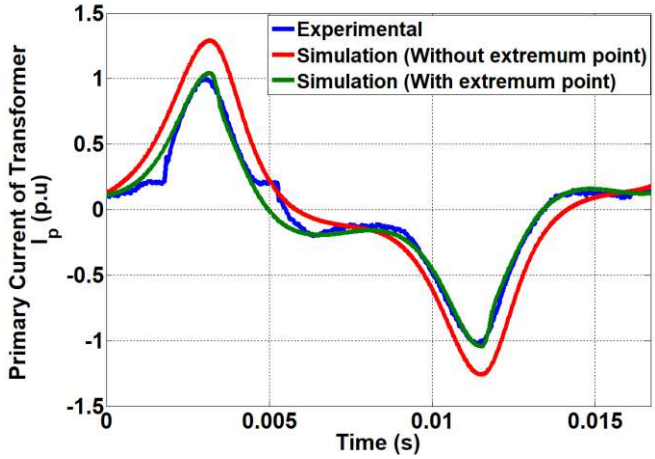

Figure 3-24 Comparison of simulation result and measurement of primary current

Figure 3-24 demonstrates the accuracy of the method. The difference of current in low values is due to the impact of sensor. The necessity of having the extremum point in identification process is confirmed by this comparison.

- Inrush current

To complete our steady state study, the previous test bench is set to have the inrush current of the transformer. The platform and module used to do the measurements are similar to the previous subsection. To know the exact closure time of the main power contactor on test bench, the measured primary voltage of transformer and the contactor command signal are presented in figure 3-25.

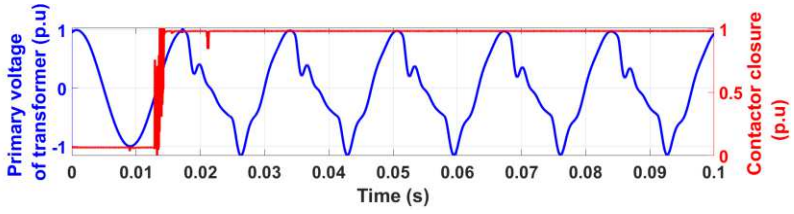

(a)

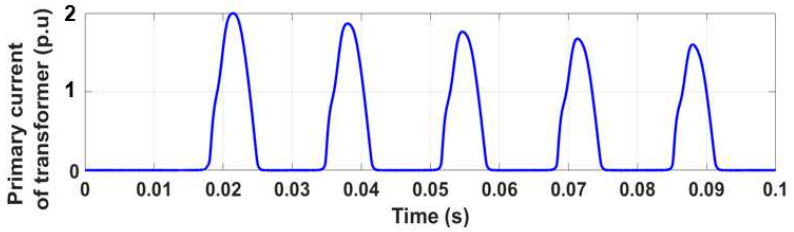

(b)

Figure 3-25 (a) Primary voltage of transformer and contactor closure time (b) Primary current of transformer on testbench

The primary voltage is deformed after contactor closure. This is due to the intermediate impedance exist between source and transformer in test bench. It deforms the voltage waveform in the case of having high amplitude of inrush current (more than nominal current of

transformer) due to the high current variation in small time interval ($\frac{dI_p}{dt}$). This will be explained in the following sections. Figure 3-25 also illustrates that the contactor closure is done while the voltage of primary was quite zero. To validate the model proposed in chapter 2, it is required to consider the closure time and the Jiles-Atherton parameters obtained in previous section. The state equations (2.27)- (2.33) are simulated considering the JA model of magnetizing inductance provided in chapter 2. A sinusoidal voltage, $U_{cat_2}(t)$, of frequency f = 60 Hz and rms voltage of 25 kV is applied on simulated model. The moment of contact closure is set at zero volt of $U_{cat_2}(t)$. Considering the remanence magnetization of $M_r = -685398.63$ A/m which can represent the initial value of magnetic flux, the simulation results are compared with the measurements. Figure 3-26 illustrates the comparison results.

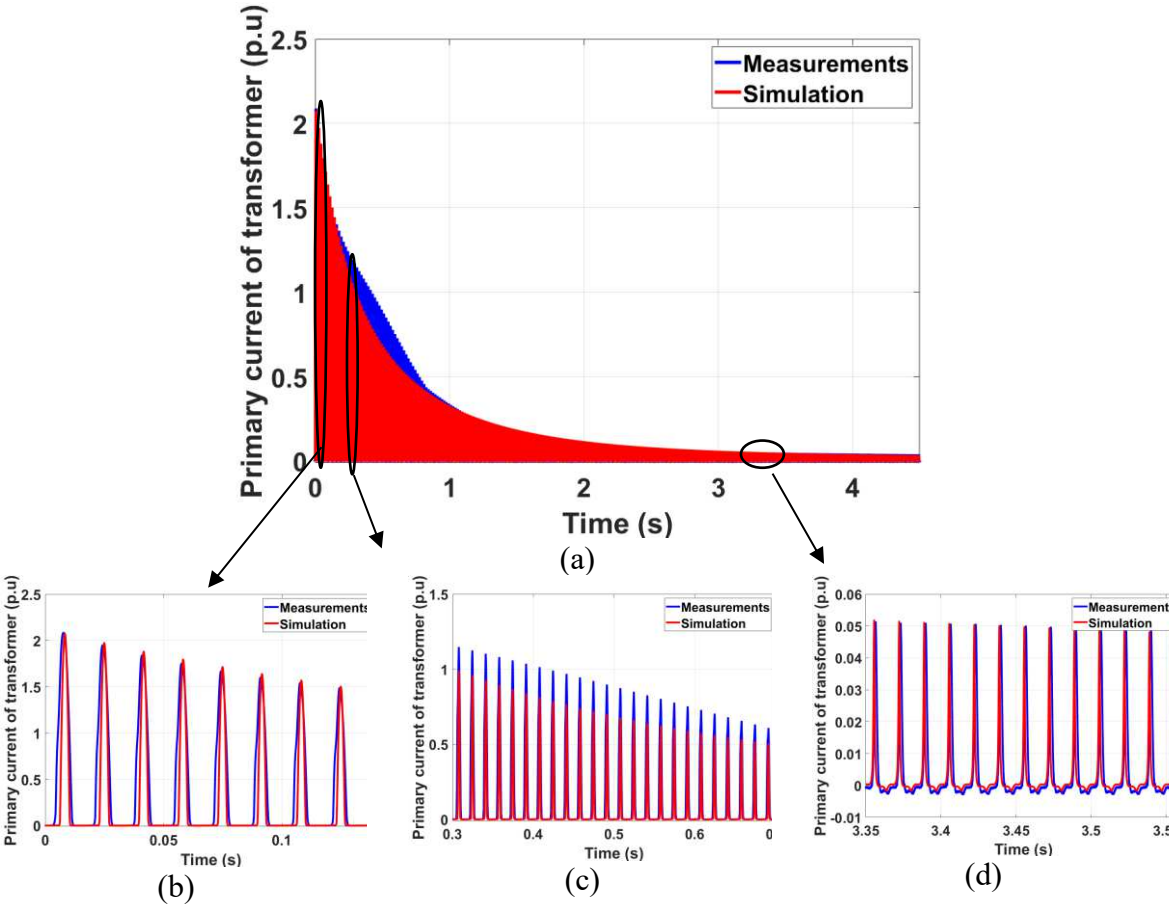

Figure 3-26 Inrush current comparison between simulation using JA model and measurements

Figure 3-26 depicts that the simulation of inrush current using JA model is in good agreement with measurement. It is able to predict the first inrush current peak accurately. However, as it is shown in figure 3-26, there are differences between the simulation and measurement in the period of 0.25 sec to 1.2 sec (figure 3-26 (b)). This is due to the fact that the voltage source is deviated in the deep saturation state due to the high intermediate impedance between source and primary of transformer which exists on test bench for system protection. The deviation of primary voltage increases the inrush current at this period. Figure 3-27 depicts the deviated

voltage source of test bench which causes this impact on inrush current. This voltage source is considered to be ideal on simulation.

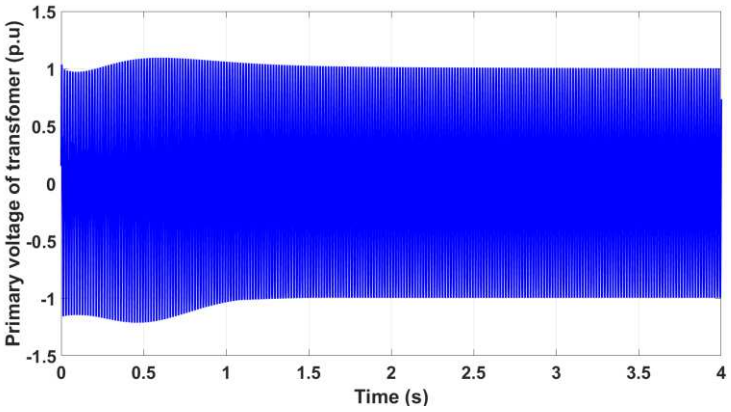

Figure 3-27 Primary voltage of transformer on test bench

The difference of simulation and measurement in figure 3-26 is not related to the accuracy of proposed method. This methodology has enough accuracy to be a representative model of transformer on real time simulator as it predicts the first peak of inrush current precisely.

Let us remind that the voltage of source is pure on real time simulator. Therefore, to represent the nonlinear characteristic of transformer in deep saturation and predict the value of each peaks in each period, the method of curve fitting is proposed to model the nonlinear behavior of magnetizing inductance on this region. Next subsection confirms this method with measurement.

3.3.3.3 Curve fitting parameter identification

In chapter 2, it is explained how to extract the nonlinear characteristics of magnetizing inductance using measurement. The inrush current test is done several times on the same test bench, transformer and platform for the measurements as described in the previous section. Figure 3-28 depicts several tests done to have the deepest saturation condition in transient state.

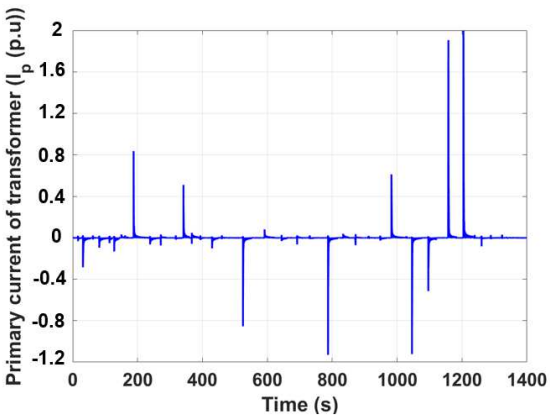

Figure 3-28 Primary current of transformer by several contactor closure

Let us remind that inrush current depends on the residual flux and amplitude of voltage at the moment of contactor closure. Therefore, even by closing the contactor at zero value of voltage, it is not certain to have the maximum peak of inrush current. This is due to the fact that the residual flux at the moment of closure also has an impact on the maximum peak (it is explained in detail in chapter 2). Therefore, it is assumed to obtain the maximum peak of inrush current on test bench during several times of contactor closure. As it is shown in figure 3-28, the maximum amplitude of inrush current is obtained at 1200 second of test. The obtained maximum value of inrush current is verified by the data sheet information.

The magnetic flux and magnetizing current are computed using the state equations of (2.27), (2.30) and Appendix A.3 (equation (A.3.4)). Then, the peak points of magnetic flux and current are extracted in deep saturation region. As the amplitude of measured inrush current is positive, the obtained peak points are mirrored to have the negative part. This method is explained in detail in chapter 2. Figure 3-29 depicts the extracted peak points of magnetic flux and corresponding magnetic current.

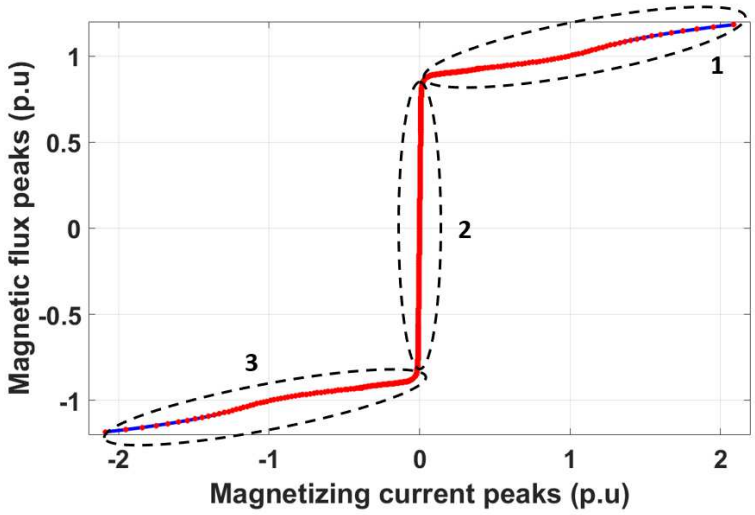

Figure 3-29 Experimental peaks of magnetic flux vs peaks of magnetizing current

As it is shown in figure 3-29, there are three different zones in the magnetizing inductance characteristics. In the zones 1 and 3, the transformer performs in positive and negative deep saturation conditions. The zone 2 represents the magnetic characteristic of transformer in steady state. Therefore, the model provided have to represent all these three zones. The proposed equation to fit the figure of magnetic flux and magnetizing current is as below:

$$I_m(\emptyset_m) = \begin{cases} a\emptyset_m^7 + b\emptyset_m^6 + c\emptyset_m^5 + d\emptyset_m^4 + e\emptyset_m^3 + f\emptyset_m^2 + g\emptyset_m + h & if\ \emptyset_m \geq \emptyset_0 \\ K_1\emptyset_m + K_2 & if\ -\emptyset_0 < \emptyset_m < \emptyset_0 \\ -(-a\emptyset_m^7 + b\emptyset_m^6 - c\emptyset_m^5 + d\emptyset_m^4 - e\emptyset_m^3 + f\emptyset_m^2 - g\emptyset_m + h) & if\ \emptyset_m \leq -\emptyset_0 \end{cases} \quad (3.9)$$

The parameters of proposed equations are adapted to obtain the measurements presented in figure 3-29. The identification results are presented in Table 3-13.

Table 3-13 Identified parameters of proposed equation for magnetizing inductance on deep saturation region

Symbol	Values
a	$2.8e12$
b	$1.29e13$
c	$1.853e12$
d	$1.712e10$
e	$-3.27e10$
f	$3.722e9$
g	$-1.788e8$
h	$3.277e6$
K_1	17.885
K_2	-0.9209

Considering the identified parameters, the proposed model is simulated based on state equations of chapter 2 and proposed equation for magnetizing inductance. The inrush current is compared with simulation result as figure 3-30.

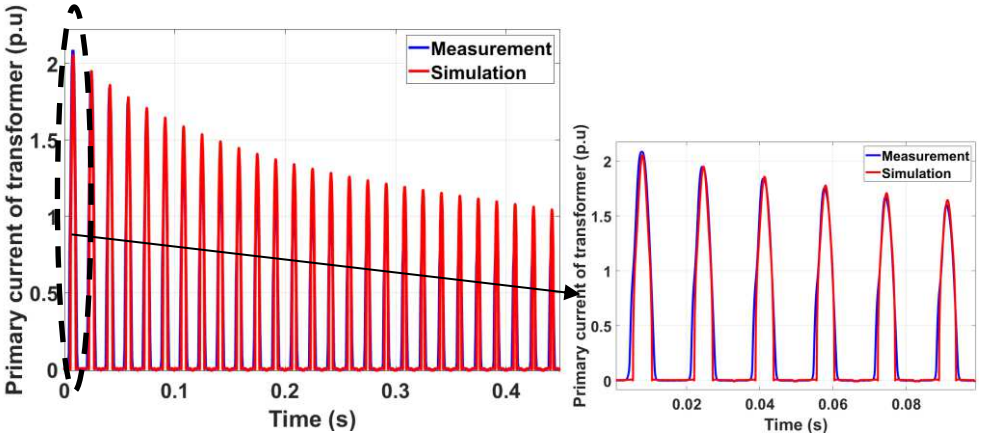

Figure 3-30 Inrush current comparison between simulation using curve fitting model and measurements

Figure 3-30 depicts that method of curve fitting have a good accuracy to predict the peak of inrush current on deep saturation region. However, this method is not representative enough on steady state region. This is due to the fact that the equation used in the period of $-\emptyset_0 < \emptyset_m < \emptyset_0$ does not have adequate accuracy as it is linear. For this period, as it is explained in chapter 2, the characteristics of magnetizing inductance is a hysteresis cycle. Next subsection confirms the final model using measurements.

3.3.3.4 Final model of nonlinear transformer and comparison with measurements

The final model proposed in chapter 2 is the combination of the JA model and deep saturation curve fitting. All the required parameters for model are adapted in the two last sections. The critical point is considered the nominal current. This means that the simulation starts by detecting the first peak. As the first peak is more than 1 p.u, the simulation continues by deep saturation model. As it is shown in figure 3-31, the nonlinearity of magnetizing inductance characteristics is going to be ended for the value of current about 1 p.u after 0.5s. Therefore, the deep saturation model is switched to the JA model. Figure 3-31 presents the comparison of

simulation using the final model of magnetizing inductance and measurements done on the same test bench and transformer in previous sections.

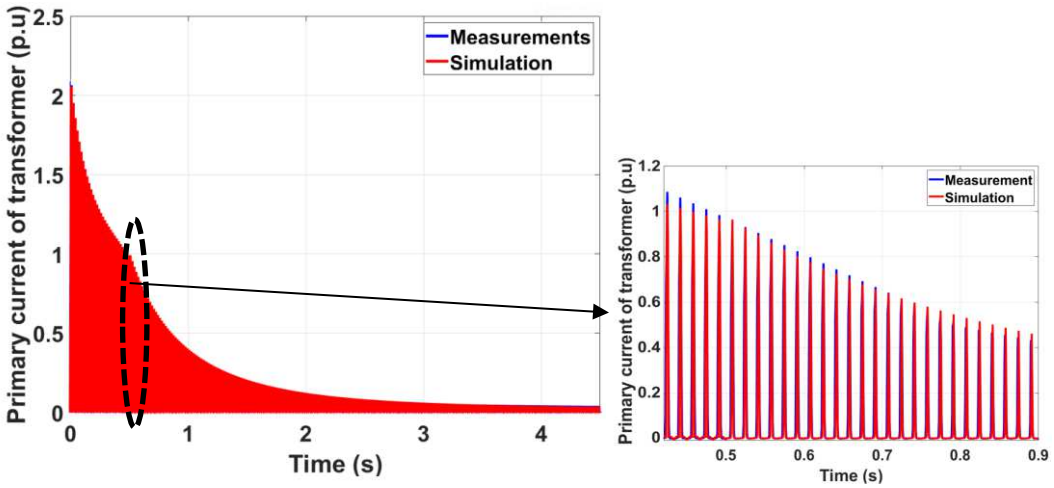

Figure 3-31 Inrush current comparison between simulation using the combination of curve fitting and JA model and measurements

The comparison done in figure 3-31 demonstrates that the final model of magnetizing inductance has a good accuracy to predict the peak value of current for each period in deep saturation state.

3.3.4 PEM Fuel cell

The equations of PEM Fuel cell stack obtained using the bond graph are proposed in chapter 2. To do the parameter identification of PEMFC model, the polarization curve obtained in simulation is compared with the experimental one. As it is explained in the previous chapter, the PEMFC system includes set of subsystems that interact inner. The static and dynamic behavior of the system output are impacted by the subsystems and PEMFC stacks. Figure 3-32 demonstrates the effect of subsystems on polarization curve during 3 hours of measurements.

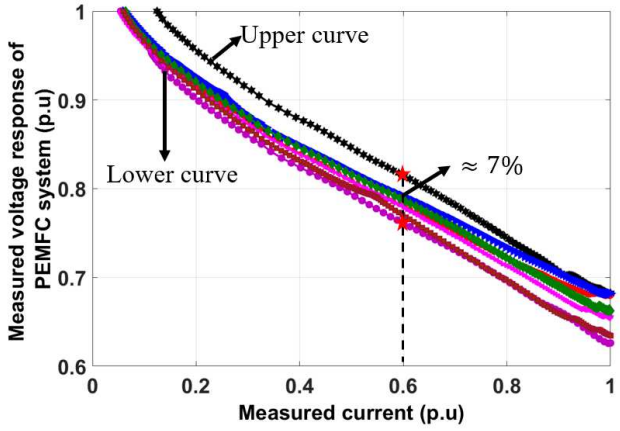

Figure 3-32 Polarization curve of PEMFC system impacted by subsystems

As it is shown, the polarization curve is changed (around 7% for the same power demand) during long time measurements due to the several parameters and elements in the PEMFC subsystems. The aim of this thesis is to propose a model which is able to predict the static and dynamic behavior of system. However, as it is required to have a simple and representative model of PEMFC system, it is focused on the user point of view model. Therefore, we will base the identification process on the measurements available while PEMFC system is integrated on the train traction system. To do so, the average profile mission which represent the PEMFC system during several hours of measurement is taken into account. This method allows us to have a simple model for PEMFC system and estimate its average behavior by unique polarization curve. It is explained in the following sections.

3.3.4.1 Experimental profile mission

To have the experimental results, the measurements are done on Alstom railway project in Germany. The train started to move from the substation in Cologne to the substation of Marienheide. The test duration was about 3 hours. Figure 3-33 depicts the measured current (a) and voltage of PEMFC system (b). These figures depict a part of signals' behavior for a recording of one hour, during the train profile mission. Note that the sampling time of measurement is 0.5 second.

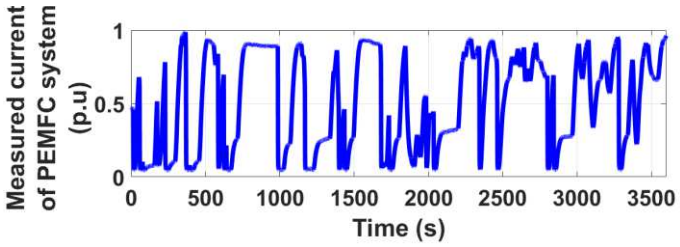

(a)

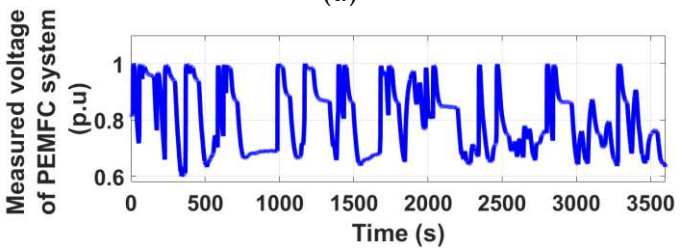

(b)

Figure 3-33(a) measured current and (b) voltage of PEMFC system

As depicted in figure 3-33, various voltage-current curves are observed based on the power demand to ensure the railway profile mission. All experimental polarization curves in mission profile are shown in figure 3-34, within 3 hours of measurement.

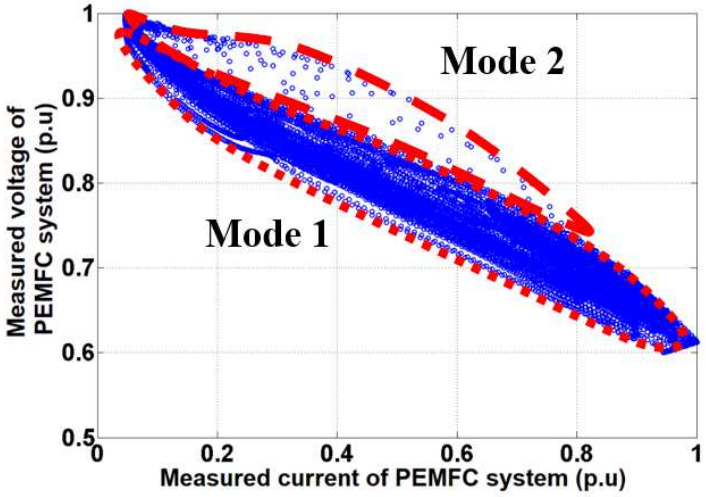

Figure 3-34 Measured voltage response versus the current extracted from profile mission for 3 hours of test procedure

The complete polarization curve can be obtained while progressive power range is demanded. Within 3 hours of measurement, 21 curves with the progressive time of more than 5 seconds are registered. As illustrated in figure 3-34, it is distinguished two modes, denoted Mode 1 and Mode 2. The Mode 1 defines the typical polarization curve impacted by the dynamic feature of system for different operating points considering the variation of temperature, level of the hydration etc. The voltage variation for the same demanded power is around 7% in polarization curves extracted from measurements (shown in figure 3-32). This is due to the factors mentioned in chapter 2 which impact the polarization curve of PEMFC system. However, to identify the parameters, it is required to have unique polarization curve which represents a typical behavior of the PEMFC system during profile mission. This typical polarization curve allows us to identify the static parameters of system. Therefore, an average of polarization curve is obtained in next section.

The Mode 2 is due to the dynamic response of PEMFC system in fast power variation (<5 seconds response) which is out of the usual polarization curve. This mode occurs at maximum power while dramatically power reduction is demanded. At maximum power demand the hydration level of membrane is high and does not respond instantaneously. This mode allows us to identify the dynamic parameters of system.

3.3.4.2 Identification of parameter of static model

To identify the parameters, the cost function is consisted of the $(V_{out})_{j,S}$ which is the simulated output voltage of PEMFC system in steady state operation and $(V_{out})_{j,M}$ which is a part of measured output voltage of PEMFC system in test procedure (we selected the last 2 hours of measurement). Please note, to do the parameter identification, a part of measured data is used. Then, to confirm the model, the comparison is done in the following with other part of measured data which is not the same as part used in identification process.

To have a unique voltage response, the part of PEMFC system characteristics in Mode 1 (within the last 2 hours of measurements) can be considered as an average polarization curve. The average of polarization curve is obtained using a window of 6% of maximum measured current as figure 3-38. For each window, the average value voltage and current values in mode 1 are represented by ($V_{out,i}$, $I_{out,i}$) operating points which are plotted by the red curve in figure 3-35.

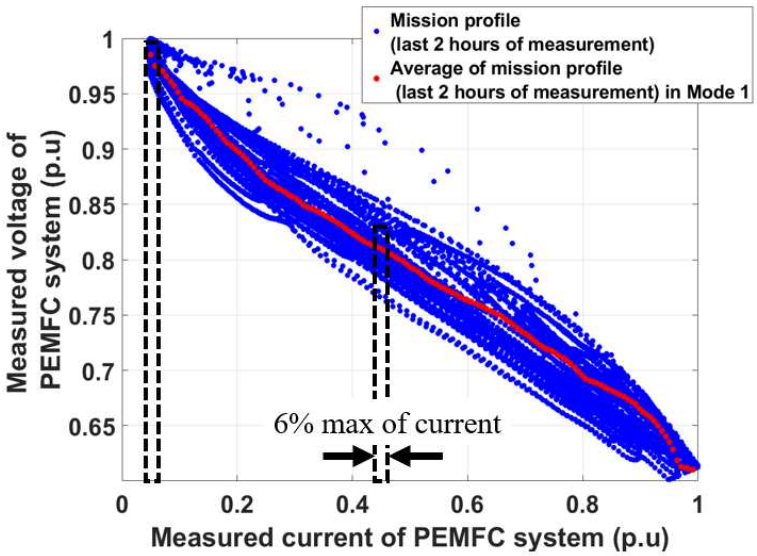

Figure 3-35 Average voltage-current points for profile mission in last 2 hours of measurements

The average curve represents the simplified polarization curve of PEMFC system used to identify the parameters of the PEMFC stack steady state model presented below:

$$V_{cell}(t) = E_{cell}(t) - \frac{RT}{\alpha nF} ln\left(\frac{I_{cell}(t) + I_n}{I_0}\right) + \left|\frac{RT}{\beta nF} ln\left(1 - \frac{I_{cell}(t)}{I_{limit}}\right)\right| - I_{cell}(t)\frac{l}{S\sigma} \tag{3.10}$$

The cost function is evaluated on the voltage of PEMFC system which is measured on last 2 hours of the test procedure. The optimization is started with 100 as the population number and 100 evaluations. As a matter of facts, 10000 numbers of iterations are done. The required parameters for steady state model of PEMFC stack are I_n, I_0 and I_{limit}. α, β and σ are given in PEMFC stack datasheet. As mentioned in chapter 2, authors have no access of detailed information about stack characteristics; and have taken some hypothesis for S and l. Based on the state of the art, they are assumed to be constant.

3.3.4.3 Identification of parameter of dynamic model

Once the desired parameters are obtained, the identification process has to be redone for the dynamic model. In this case one cycle of response voltage in Mode 2 is selected as figure 3-36.

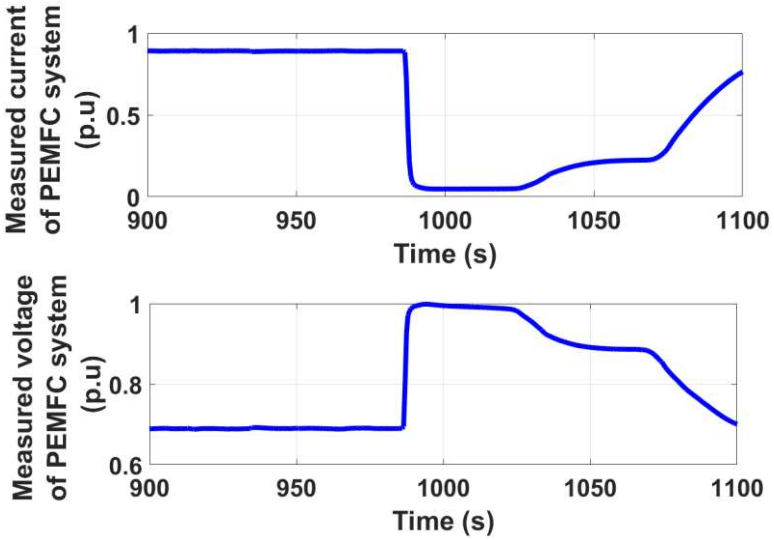

Figure 3-36 The selected part of measured voltage and current to identify the parameters of dynamic model

The second identification process provides the values of λ_e, τ_e and $T_C = C.(R_{act,cell} + R_{conc,cell})$ for the dynamic model of PEMFC highlighted again as below:

$$V_{cell}(t) = E_{cell}(t) - \lambda_e\left(I_{cell}(t) - I_{cell}(t) * exp\left(-\frac{t}{\tau_e}\right)\right) - V_{c,cell}(t) - I_{cell}(t)\frac{l}{S\sigma} \tag{3.11}$$

The cable impedance value is computed based on the its nominal value per meter. Table 3-14 depicts the identified parameters of PEM Fuel cell model.

Table 3-14 Identified parameters of PEM Fuel cell model

Static model parameters		Dynamic model parameters	
Symbol	Values	Symbol	Values
I_n	0.03 A	λ_e	0.005
I_{limit}	747.87 A	τ_e	1
I_0	0.00001 A	T_C	0.3

3.3.4.4 Comparison the simulation results with experimental

The PEMFC system model is simulated using (2.55) - (2.61). All the identified parameters in section 3.3.4.2-3 are inserted in the model. The measured power demand of PEMFC system in the first 1 hour of measurement is applied to the simulated model; then the results are compared with the measured output voltage as illustrated in figure 3-37.

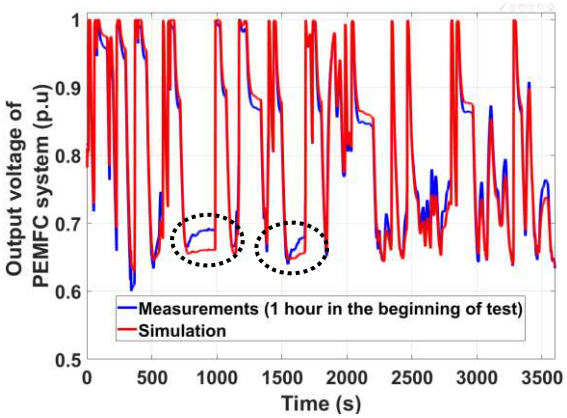

Figure 3-37 Comparison of measured output voltage of PEMFC system and the simulated one using identified parameters

The average error of model during the profile mission in the first one hour of measurement is 1.85%. In mode 1 which consists about 90% of profile mission, the average value of error is about 1.7% and in mode 2 which consists about 10% of profile mission, the error is about 5%. On the proposed model, the average of profile mission is considered to identify the parameters, therefore it is obvious to have error on some specific (shown by circles in figure 3-37) which are far from the average polarization curve (mode 1). The polarization curve obtained in the simulation is compared with result on train in the first one hour of testing in figure 3-38. It is shown that simplified model of PEMFC system can represent two modes of experimental polarization curve.

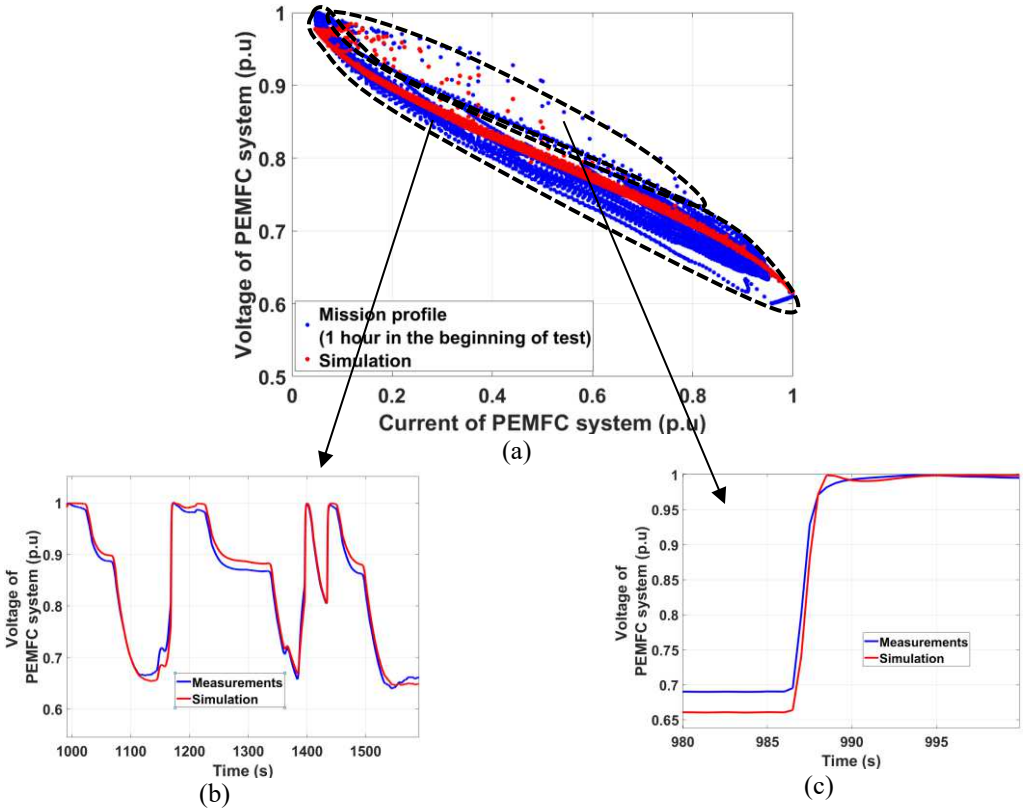

Figure 3-38 (a)Comparison of measured voltage and current of PEMFC system on train and the simulated one, example of voltage comparison in (b) mode 1 and (c) mode 2.

It is concluded that having average polarization curve allows to predict the overall behavior of PEMFC system with enough accuracy in mode 1. Also, in mode 2, the simulation results have enough agreement with measurement generally. However, some differences can be seen in low value of voltage in mode 2. This is due to the fact that the dynamic behavior of PEMFC system depends on several reactions of internal subsystem which are not considered in PEMFC stack model. But these differences are neglectable in the applications in which the user point of view model is required.

3.4 Conclusion

In this chapter, the required parameters of proposed model in chapter 2 are identified using differential evolution estimation method. The identification procedure is applied to four models, which presents nonlinearities. The identification procedure is applied to magnetizing inductance, pantograph bounce, transformer model and PEMFC.

The parameters of magnetizing inductance function are identified using the experimental results proposed in the datasheet of asynchronous motor. The effect of variation of magnetizing inductance on stator current is depicted by comparing the simulation results and test bench. It is deducted that considering the magnetizing inductance variation on asynchronous motor model can reduce by 9% the relative error between experimental and simulation form certain specific operating points.

The electrical arc parameters are identified using the measurements on train. Comparison between measurements on train and simulation results shows that presented model is sufficiently accurate to predict the behavior of the whole system during pantograph bounce phenomenon.

The proposed transformer model including nonlinear magnetizing inductance is validated by comparing the simulation result and test bench measurements. Due to non-ideal test conditions, analyses are done considering entire and uncomplete hysteresis cycle. It is shown that JA parameter identification can be done with a part of the hysteresis cycle that includes the extremum point and coercive field. Then, the parameter identification is performed on a transformer included in a test bench representative of a railway traction system. The simulated primary current is compared with the measured one and shown a great accuracy. It is demonstrated that few measurements are needed to completely and precisely identify parameters of power transformer in order to simulate it. To have an accurate representation of transformer in deep saturation and steady state region, a complete model consisted of JA model and curve fitting is proposed. By comparing the simulation and experimental results, it is demonstrated that it has enough accuracy to predict the inrush and magnetizing current. These simulations used during validation and verification process may lead to a clear evaluation of performances of the traction system.

The parameters of PEMFC stack model proposed in chapter 2 are identified using average experimental profile mission on train. This leads to have a simplified model of overall system in order to be easily simulate in railway application. The parameters of model are identified using the experimental average polarization curve. The two major characteristics of system in various operating modes are simulated using the dynamic model. Comparison between measurements and simulation results depict that the presented model sufficiently accurate to predict the behavior of PEMFC system.

This study has to be completed by providing the sensitivity analysis of models. It is also needed to validate the compatibility of each model in overall traction system simulation and verify the accuracy of proposed models compare to the previous models. These studies are provided in next chapter.

Chapter 4

Traction system experimental measurements, comparison with simulation, sensitivity analysis

4.1. Introduction

Sensitivity analysis and validation of model are linked together in that both of them attempt to confirm the accuracy of a particular model and appreciate the strength of the conclusion being drawn from a model [139]. The validation of a model is useful to evaluate the model fit within a specific research dataset. The sensitivity analysis is particularly useful in gaining confidence in the results of the primary analysis and is important where a model is likely to be used in a future research investigation [139].

In this chapter, the model validation in overall system and sensitivity analysis are done to complete our studies and strength the conclusions. Therefore, in the first step, the proposed model of transformer and asynchronous motor is adapted to be integrated in the traction system simulation. Then, validation is done by comparing the traction system simulation results with test bench measurements.

In chapter 3, the parameters of four proposed models are identified using the measurements. The four models are validated separately by comparing the simulation results using identified parameters and measurements on train and/or test bench. To measure the impacts of fluctuations in the identified parameters of the output behavior, a sensitivity analysis is required. In this chapter, the sensitivity analysis definitions and process are explained. In section 4.3, it is applied to parameters of the nonlinear magnetizing inductance model in transformer. To demonstrate the impact of nonlinear elements on overall model, the sensitivity analysis is done on system transfer function. Then, the Numerical Estimation technique and Design of Experiment is used to find out the parameters of nonlinear element models which have the most important impact and likely effect the system behavior. Finally, in section 4.4 a conclusion is provided.

4.2. Validation of proposed models in the overall traction system simulation

The model validation process is done by comparing the simulation results and measurements in different operating points. To do so, Alstom test platform for high speed train project is selected to obtain the experimental results, as illustrated in Figure 4-1. Figure 4-1 depicts the block diagram of the overall system test bench. The primary of the power transformer is connected to an AC voltage source (25kV/60Hz) by main contactor. The secondary of transformer is connected to a motor block which consists of two traction chain. Each traction chain is constituted by one rectifier (AC/DC), a low pass filter, an inverter (DC/AC), an asynchronous motor (ASM) and mechanical part (gear box and generator). To ensure the harmonic features, power losses etc., the control system applies PWM methods on converters (rectifier and inverter). The auxiliary circuits are connected to the voltage bus of traction chain to be supplied and provide the required voltage for cooling systems.

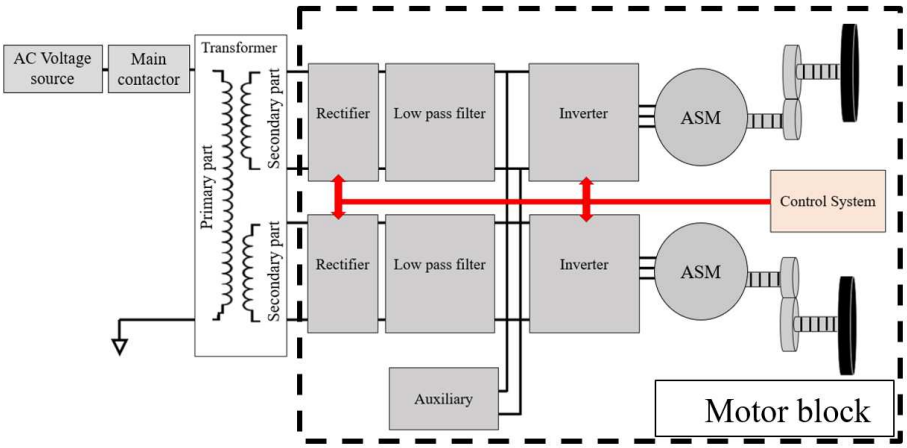

Figure 4-1 Block diagram of the overall system test platform for high speed project

As it is mentioned in chapter 1, the test bench is an environment including a part of the train system to do validations and verifications. The considered train system includes two motor blocks. However, the test bench is set by one motor block chain and its control system. Figure 4-2 depicts the test bench environment where the measurements are done. The main contactors, transformer, power modules (Converters), asynchronous motor (ASM) and control system are depicted respectively.

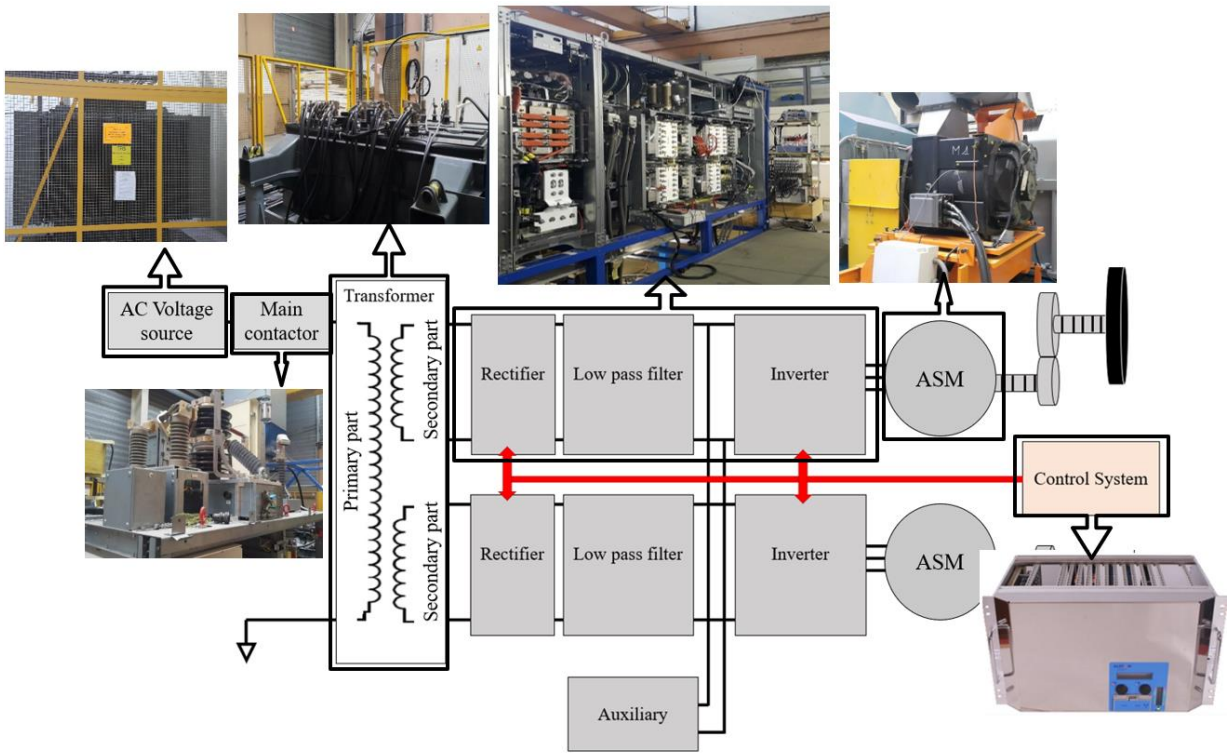

Figure 4-2 Test bench environment including the AC voltage source, the main contactor, transformer, power modules (converters and rheostat chopper), ASM and control system

The measurements are done using the DI-722-EN data acquisition system and Banana Jack Signal Interface Option. The acquisition system and its interfaces on test bench are shown in figure 4-3.

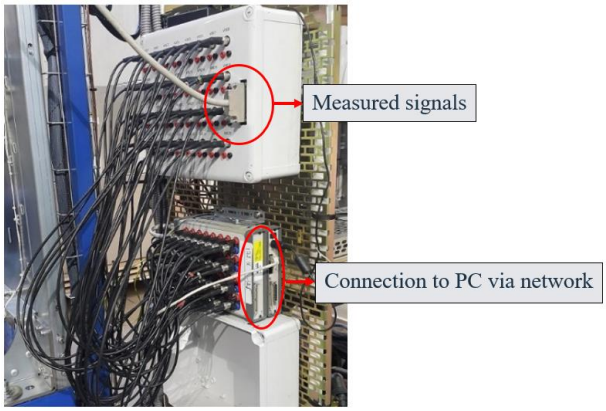

Figure 4-3 The acquisition system and its interface

The data are recorded by 1ms of sample time.

As a first step of test, the test bench has to be launched by demand of main contactor closure. The main contactor is placed in the primary part of transformer which will be closed after ensuring the security aspects by control system. An interface software shown in figure 4-4 allows to send the closure or open contactor demand. After a while (about 1 minutes), the preload is done, and the voltage is supplying the overall traction system. Preload process is automatically achieved by the control system. Its role is to avoid the overshoot of voltage within the secondary contactor closure. After this step, it is possible to demand the traction by a manipulator (handle) shown in figure 4-4. Let us remind that the effort value in motor level is controlled by the percentage of manipulator (0-100%) and speed. Then, motor drive control system generates the fundamental voltage magnitude and frequency via inverter to create the required effort level on the motor. Handle value is registered by the data acquisition system.

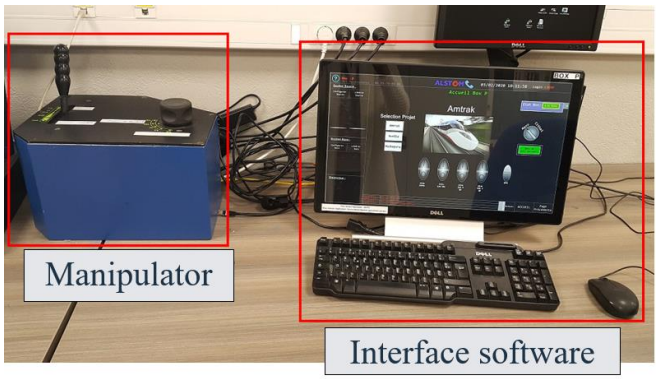

Figure 4-4 The interface software and manipulator in test bench

To start the test, the manipulator percentage is increased progressively. Then, the speed will increase consequently. Note that the technician that does the test have the control of manipulator

percentage and speed as well. This means that it is possible to have a specific operating point by forcing the speed and/or percentage of manipulator on specific value. Figure 4-5 depicts the signals applied on traction system in test bench and the speed measurement.

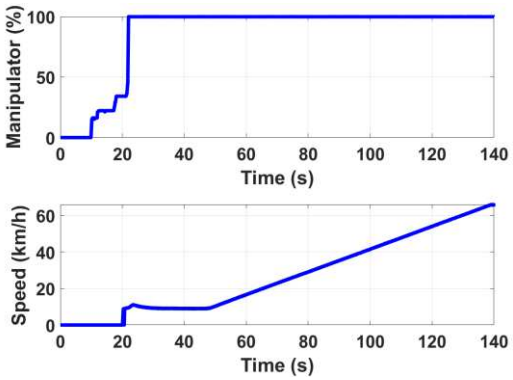

Figure 4-5 The applied percentage of manipulator and recorded speed on test bench

In the beginning of test, there is no effort demand therefore there is no speed augmentation. After 10 seconds, the effort is demanded progressively (in 4 steps: 15%, 20%, 35% and 100%). After applying the 35% of effort which is the required initial value of effort for train to do the traction in this specific project, the speed is started to be increased. The augmentation of speed is continued for 5 seconds. Then, the technician forces a constant value of speed (about 9 km/h) for 25 seconds. The speed limitation is removed at 48 second which the speed is going to be increased. The measurements were ceased in 140 second which the speed reached to 65 km/h. The maximum value of speed in this specific project is around 150 km/h. Please notice that the applied operating points was done for other specific purpose of validation teams in the company and we are going to use these data to validate our models.

In the following, as the purpose is focused on transformer and ASM, the primary transformer current and one phase of ASM currents are measured in order to do the comparison with simulation results. Please note that due to the experimental constraint, the simulation comparison of two other models (pantograph bounce and PEM Fuel cell model) were not possible in overall traction system.

The simulation scheme of overall traction system and its associated control system are provided as figure 4-6. The simulations are obtained thanks to the traction system model that reproduces every components of the test bench (one motor block), including the control system. Due to the lack of impact between two traction chain in one motor block in our case, the simulation is performed considering one motor block with one traction chain. Then, the demanded current from traction system (primary current) is multiplied by factor 2. Let us remind that in this section, it is aimed to verify the compatibility of proposed models in overall traction system simulation: more precisely fundamental values are under concerns. However, for analysis of harmonic and/or transformer behavior in saturation region (Inrush current), this hypothesis is no longer valid.

Note that the auxiliary system is necessary in test bench to regulate the temperature of power components. As this system does not have a great impact on the final measurements in our cases, it is not considered in the simulation. Note that the simulation of overall traction system has been already existed and used for the simulation tests in control command and power electronic requirements in company. The ASM model existed in this simulation file was the one with constant magnetizing inductance. In addition, the nonlinear model of magnetizing inductance for transformer model was not considered in the beginning of thesis. In this part of the thesis, it is desired to replace the old models by proposed models of ASM and transformer (ASM model with constant magnetizing inductance and transformer without nonlinear magnetizing inductance). As a first step, it is necessary to have the same input and output for each improved subsystem in order to be compatible to be integrated in the overall system. The input and output of these two subsystems are provided in chapter 2 thanks to the bond graph method. The bond graph of ASM demonstrates that its inputs are the three phase voltages provided by inverter and the demand of torque (in our case it is applied as the demand of speed) and its output is the stator current. The bond graph of transformer also depicts that the inputs of this subsystem are the voltage of catenary and the voltage of rectifier in the secondary part of transformer. As the simulation of system is provided like test bench condition, the catenary voltage is an AC voltage source connected directly to the transformer. The output of this subsystem is the primary current of transformer.

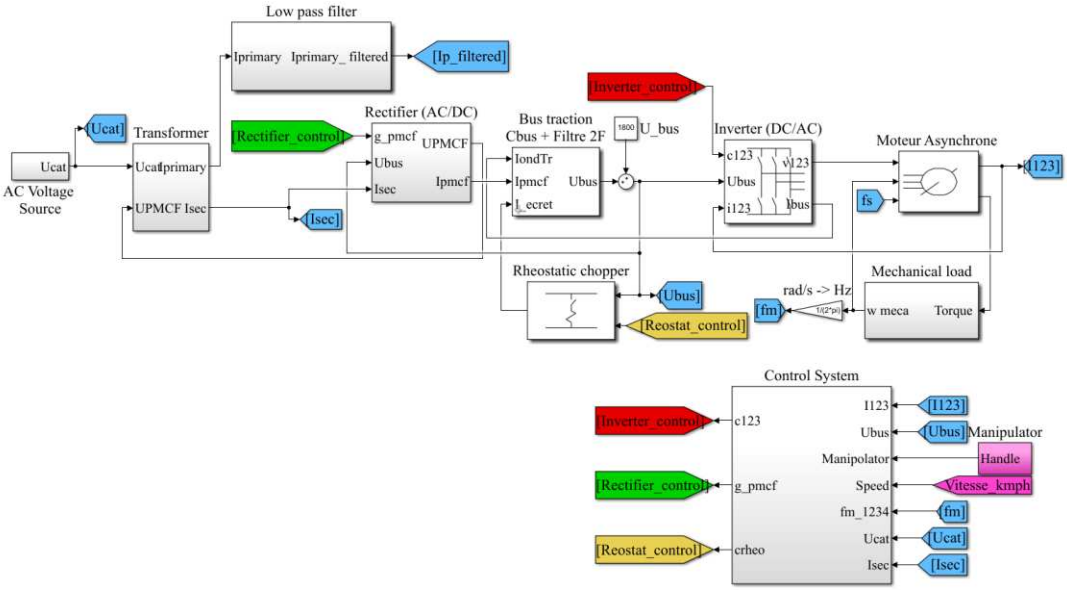

Figure 4-6 Overall traction system simulation blocks

The measured manipulator percentage and recorded speed (with sample time of 1ms) are applied as an input of traction system. In simulation environment, there is a control system which has to send the command to the converters in time interval less than input time steps (1ms). In some cases, the system may have some instantaneous variations which again required to have time steps less than input (1ms). Therefore, the simulation is set on variable step to

obtain the correct and accurate results in all conditions (steady and transient states) and to have a balance between the accuracy and simulation time.

To demonstrate the impact of nonlinear model of transformer and ASM, the simulation is done in two conditions with proposed model and old one. Then, the results are compared with the measurements. Figure 4-7 depicts the comparison result. Note that to eliminate the undesirable harmonics appeared due to the regulation of rectifier, a first order filter is designed as equation (4.1). It is set to pass the low frequencies with cut-off frequency ($f_{cut\ off}$) of 300 Hz to eliminate the higher frequency occurs due to rectifier switching.

$$H_{LPF}(s) = \frac{1}{(T_s s + 1)} \tag{4.1}$$

where $T_s = \frac{1}{2\pi\, f_{cut\ off}} = 5.3052^{e-4}\frac{s}{rad}$. Note that since the cut off frequency and fundamental frequency (60 Hz) are close (less than one decade); therefore, the gain at fundamental frequency is affected by the factor of 0.83. So, to have an effective representation in figure 4-7, we multiplied the filter output signals by $\frac{1}{0.83} = 1.204$ to compensate this effect.

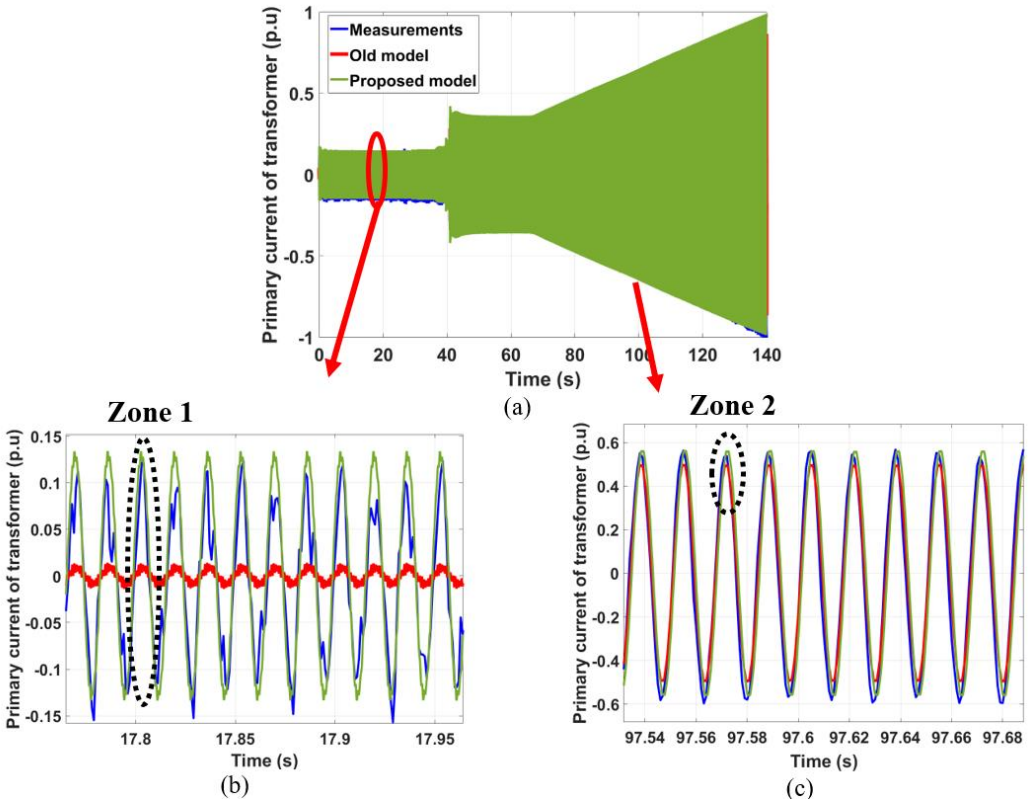

Figure 4-7 (a) Comparison of simulated primary current of transformer and measurements (b) without traction (0% of manipulator and 0 km/h of speed) (c) with traction

Figure 4-7 demonstrates the compatibility of nonlinear model of transformer proposed in this thesis with overall model of traction system. In figure 4-7, the primary current of transformer obtained by proposed model is compared with the old model of transformer and measurements

on test bench. In the time interval shown in figure 4-7 (b), there is no traction and speed demand. This means that the primary and preload contactor are closed but no current is demanded from traction system. In this case, the primary current consists of the magnetizing current and leakage current. As the magnetizing inductance model is neglected in the old model of transformer, the primary current obtained in the simulation is much lower than the results from proposed model. The harmonic effects in measurements are due to the non-ideal sensor used in test bench which is not able to measure low value of current (no load current). The voltage source in test bench also is non-ideal and has some variation of frequency along time. However, the voltage source frequency is constant in simulation. The difference between the old and proposed model is lower while the traction is demanded (figure 4-7 (c)). This is due to the fact that the magnetizing current is negligible compare to the overall current demanded from traction chain load. However, generally, it can be seen that the proposed model simulation result is more accurate and representative compare to the old model. Table 4-1 presents the comparison of peak value of primary current in one period for zone 2 to emphasize this conclusion.

Table 4-1 Comparison of simulated current peak and measurement in zone 2 of figure 4-7

Old model (p.u)	**Proposed model (p.u)**	**Measurement (p.u)**	**Relative error (Old model)**	**Relative error (Proposed model)**
0.5	0.56	0.558	10%	0.3%

Relative errors of 0.3% of proposed model comparing to 10% of old model in 2 emphasize and prove the accuracy and necessity of proposed nonlinear model of transformer. The simulation results are in good agreement with experimental ones. Let us remind that the measurements were done by the validation team for different purpose. As the main contactor had been closed before data recording, therefore, the inrush current was not recorded. So, there is no available recorded data to do the comparison on the transient state of transformer for this specific test.

To verify the compatibility of ASM model with overall traction system model, the stator current is compared with the measurements as shown in figure 4-8.

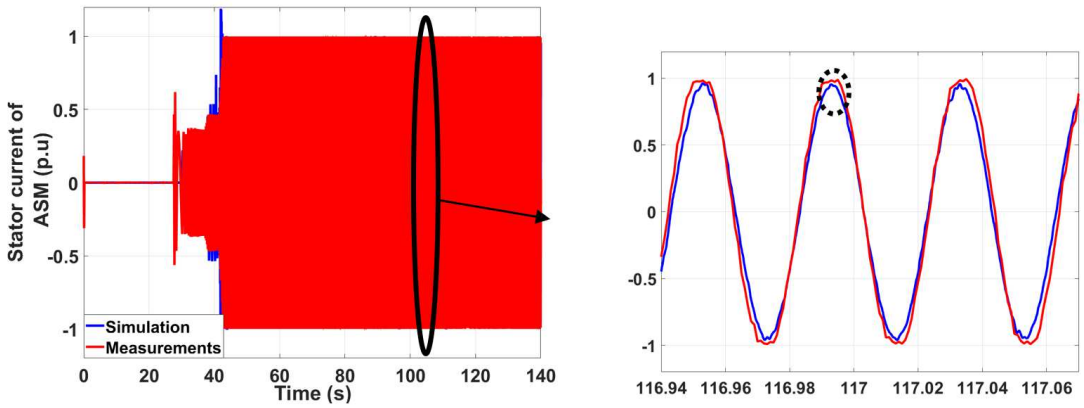

Figure 4-8 Comparison of simulation and test bench result of stator current of ASM

It is shown that by applying different percentage of manipulator (handle) and speed, the ASM model responses accurately and it is compatible with overall model of traction system. The maximum peak of stator current (shown by circle in figure 4-8) in simulation and measurement are 0.98 p.u and 1 p.u respectively which represent 2% of error of simulation (less than 5% based on industrial criteria).

In this case, the comparison is not provided for the old model with constant magnetizing inductance. This is due to the fact that the variation of magnetizing inductance is negligible for these provided operating points measured on the test bench. This means that at these operating points, the magnetizing inductance is equal to the constant magnetizing inductance considered in the old model. Therefore, the simulation results with and without variation of magnetizing inductance are the same in our specific case.

It is concluded that to have an accurate result, considering the nonlinearity of the models are necessary.

4.3. Sensitivity analysis

As a model is created, the sensitivity analysis should be performed to have a global vision on the effect of parameters and their interaction on the variables. Therefore, once the corresponding parameters are identified, it is required to do the sensitivity analysis. Sensitivity analysis is done to understand how uncertainty in the output of the model can be apportioned to different sources of uncertainty in the parameters of model [140]. In other words, the sensitivity analysis is the simulation response to extreme values of model parameter or drastic changes in the structure of model [141]. The results of a sensitivity analysis are used to:

- validate a model.
- remark the important assumptions.
- adjust model structure, simplify a model, etc [142].

It allows to interpret what happens when a parameter of simulation model changes. Sensitivity analysis can help us to demonstrate the sensitive parameters identified previously that can impact the output of model. There are many researches on global sensitivity analysis for large simulation models [143] and [144]. In this thesis, a simple technique of sensitivity analysis which require less computation is used to intuition of subsystems output behavior regarding the variation of inputs.

4.3.1. Sensitivity functions and definitions

As described in [142], there are two classes of sensitivity function, namely, analytic and empirical. When the system under study is relatively well-defined and simple, the analytic sensitivity functions are used. Otherwise, the empirical sensitivity functions are applied. One of the main functions in this category of sensitivity analysis is the absolute-sensitivity function.

It is used to understand which parameter has great impact on the output for a fixed size changes in the parameters. As an example, the absolute sensitivity analysis, S of the function f, when the parameter a varies, is expressed in equation (4.2).

$$S_a^f = \frac{\partial f}{\partial a} \qquad @ \text{ Normal operating mode} \tag{4.2}$$

The normal operating mode means where all the parameters have their normal values (there is no parameter variation). This method of deviation is also used to know the impact of parameters interaction. In this case, several parameters are changing at the same time. As an example, the absolute sensitivity analysis, S , in the case of changing parameter a and b in function of f, is expressed in equation (4.3), [142].

$$S_{a,b}^f = \frac{\partial^2 f}{\partial a \partial b} \qquad @ \text{ Normal operating mode} \tag{4.3}$$

In previous examples f is perfectly known. In this thesis, the models of real systems are provided in which deriving the sensitive functions is difficult. In this case the Numerical Estimation technique which is a kind of empirical sensitivity functions can be performed to find the system sensitivities [142]. In this case, the model is evaluated at its normal operating point, when there is no variation in the model parameters, and they have their normal values. Then a specific parameter of model, denoted as an example a is decreased or increased, and a new operating point is obtained by the evaluated function, $f(x)$. Equation (4.4) depicts the difference between these two function values [142].

$$S_a^f = \frac{\Delta f}{\Delta a} = \frac{f(x)_{a=a_1} - f(x)_{a=a_0}}{a_1 - a_0} \tag{4.4}$$

where, Δa and Δf represent the parameter and output variation respectively while parameter a changes from a_0 to a_1. Therefore, the first derivative of function S_a^f demonstrates the ratio of output variation to one input variation. In [142], the second derivative of function $f(x)$ considering the variation of two and more parameters are presented. The numerical estimation method is used in this thesis to do the sensitivity numerically.

To do the sensitivity analysis on the model of system, it is required to run the simulation program for several combination of model parameters. The different combinations are called scenarios and the simulation inputs are called factors in Design of Experiment (DOE) [145]. DOE is an important and practical method for sensitivity analysis of simulation models, and it can be applied to all simulation models such as deterministic, stochastic, either in steady state or transient state. In this thesis, this technique is used to determine the individual and the interactive effects of the factors in nonlinear parameters of proposed model that could affect the state variables. This is explained in detail in the following sections.

4.3.2. DOE definitions and method

The basic idea in DOE is to assign N level for each factor, therefore, the required experiments is $n = N^k$ where k is the number of factors. As a simple example, it is considered to have 2 factors with 2 levels. Considering 2 levels for each factors means that in one level the parameter is decreased by several percentages from its normal value (low level, denoted by -1) and the in other level, the parameter is increased by several percentages from its normal value (high level, denoted by +1). To analyze the model sensitivity while two parameters are changing, it is needed to consider the interactions between parameters. The interaction between the parameters occur while the level of one factor (parameter of model) is not the same at all level of other factor. In the experimental plan, the interactions between parameters has also two levels: low and high (denoted by -1 and +1). In this example, the low level of interactions between two parameters is defined while the two parameters are not in the same level (one of the parameters is in low and another in high level). The high level of interaction (denoted by +1) occurs while the both parameters are in high level or low level. Table 4-2 illustrates an example of experimental plan for DOE method for 2 factors with 2 levels. Note that $Y_i, i = 1,..4$ is the output of model considering the parameters (A and B) variations for each scenario.

Table 4-2 Example of experimental plan for DOE method for 2 factors and 2 level

Experiment = scenario	A	B	AB(Interaction)	Output response
1	-1	-1	+1	Y_1
2	+1	-1	-1	Y_2
3	-1	+1	-1	Y_3
4	+1	+1	+1	Y_4

To analyze and demonstrate the impact of each parameters and interactions on the system output, f in normal operating point, a function as (4.5) is considered.

$$y \sim f_0 + S_A^f A + S_A^f B + S_{AB}^f (AB) \tag{4.5}$$

where f_0 is the normal value derived from experiments, A and B are the factor and AB is the level of interaction between A and B. Note that A and B are defined on a coded scale from -1 to +1 (the low and high levels of model parameters). S_A^f, S_B^f and S_{AB}^f illustrate the effect of individual and interaction factors in the global response of a given output (y) where they are calculated by sensitivity functions or Numerical estimation technique using (4.4). Equation (4.5) illustrates the fact that each factor has an effect on response with respect to the nominal value f_0. In the following sections due to the several scenarios in level +1 and -1, $f(x)$ represents the average of output response. This method of sensitivity analysis is used in the following sections.

4.3.3. Applying the sensitivity analysis on proposed models

As a first step of sensitivity analysis, it is required to identify the state variables which are directly impacted by variation or error on nonlinear parameters presented in this thesis. To do so, the bond graph of overall traction system including proposed models are presented as illustrated in figure 4-9.

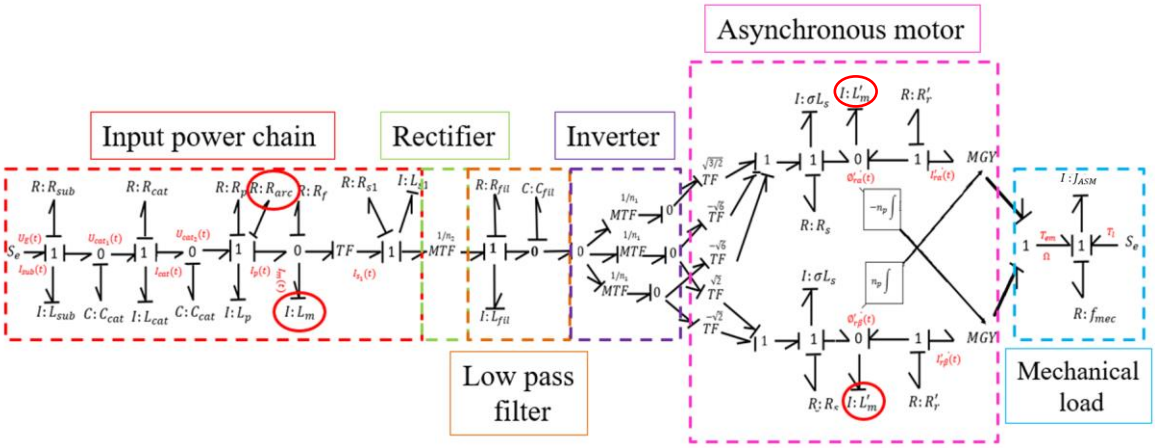

Figure 4-9 Bond graph of overall traction system

As represented in the bond graph, the substation voltage feeds the overall system. And based on mechanical load, traction system demands current from substation. In this case, the primary current of transformer is the output and representative variable of traction system. There are 14 state variables: current of substation, current of catenary, current of primary, magnetizing and secondary of transformer, current of inductance of low pass filter, stator current in α and β axes, voltage of catenary (in 2 parts), voltage of capacitor of low pass filter, rotor flux in α and β axes and speed rotation. In figure 4-9, the nonlinear parameters of subsystems proposed in this thesis are shown by red circles. The state variables that are directly impacted by these nonlinear parameters and that can be measured on test bench as well, are required to do the sensitivity analysis. Based on that, the primary current of transformer and stator current of motor (the phase stator current is obtained by two state variables: stator current in α and β axes) are matching both criteria. However, as it is shown in chapter 3, the nonlinear magnetizing inductance improves around 80A (0.075 p.u) in the best case. This means that by having around 400V of stator voltage, the total differences in output power of ASM is 32 kW. As the power of input and output of system have to be the same, therefore, in the case of having 25kV as primary voltage, the impact of stator current variation on primary current would be less than 32kW/25kV=1.28A which is negligible. Therefore, the variation in stator current due to magnetizing inductance error does not impact highly the primary current of transformer, $I_p(t)$ as the traction system representative variable from overall system point of view. As well, based on the bond graph in figure 4-9, the $I_p(t)$ is not directly impacted by variation on magnetizing inductance of ASM due to the passive and active components such as inverters, rectifier and transformer which change the current ratio (from 80A at motor stator current to 1.28A at $I_p(t)$).

Therefore, the sensitivity analysis is studied on transfer function of transformer by considering error or variation on magnetizing inductance on state variable, $I_p(t)$. This is explained more in detail in the following section.

4.3.3.1. Transformer transfer function

As a first step, the bond graph of transformer is presented as below in isolated secondary and test bench condition (No substation and catenary).

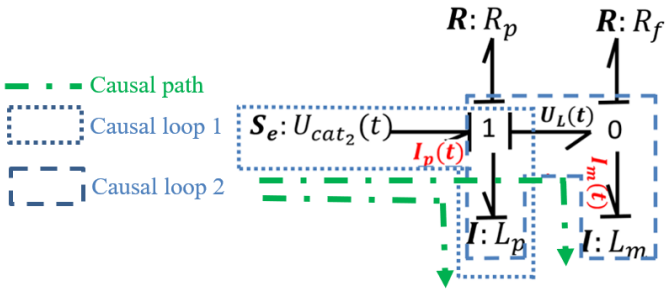

Figure 4-10 Bond graph of transformer in test bench condition and isolated secondary

Based on the bond graph, it is obtained that there are 2 state variables in the transformer model. These two important state variables are the primary and the magnetizing current. The link between storage elements obtained by causal loop/path definitions in bond graph (shown in figure 4-10), can lead us to know the possibility and/or necessity of doing the sensitivity analysis in a system. It is shown that there is a causal loop which make a link between two storage elements: magnetizing inductance and leakage inductance. This determines that in the case of having variation of magnetizing inductance, the energy variable of leakage inductance which is $I_p(t)$ receives this impact. There are also two direct causal paths (shown in green dot dash in figure 4-10) which pass from voltage source to two storage element *I* related to leakage inductance and magnetizing inductance. The voltage source is as an exciter for these two storage elements. This means that the energy variables of these two storage elements, $I_p(t)$ and $I_m(t)$, are the system output and the voltage source, $U_{cat_2}(t)$ is the input. Therefore, based on the electrical model and the bond graph, the transfer function of transformer can be obtained in Laplace domain explained in the following.

To obtain the transfer function using bond graph, it is required to provide the state space representation of the system [146]. The transfer function $H(s)$ based on the state variables in Laplace domain is obtained as below [146].

$$H(s) = \frac{X(s)}{U(s)} = (sI_n - A)^{-1}B \tag{4.6}$$

where $X(s)$, $U(s)$, s, I_n, A and B are state variable, input source, Laplace operator, identity matrix, dynamic and input matrix, respectively. Based on the equation (4.6), the state space

matrix of transformer is as below. Please note that to obtain the transfer function and state space matrix, the nonlinearity of magnetizing inductance is not considered in this case.

$$\begin{bmatrix} \dot{I}_p \\ \dot{I}_m \end{bmatrix} = \begin{bmatrix} -\frac{(R_p + R_f)}{L_p} & \frac{R_f}{L_p} \\ \frac{R_f}{L_m} & -\frac{R_f}{L_m} \end{bmatrix} \begin{bmatrix} I_p \\ I_m \end{bmatrix} + \begin{bmatrix} \frac{1}{L_p} \\ 0 \end{bmatrix} U_{cat_2}(t) \tag{4.7}$$

The transfer function of transformer using (4.7) for two state variables is as (4.8) and (4.9):

$$\frac{I_p(s)}{U_{cat_2}(s)} = \frac{\left(\frac{1}{L_p}\right)\left(s + \frac{R_f}{L_m}\right)}{\left(s + \frac{(R_p + R_f)}{L_p}\right)\left(s + \frac{R_f}{L_m}\right) - \left(\frac{R_f^2}{L_m L_p}\right)} \tag{4.8}$$

$$\frac{I_m(s)}{U_{cat_2}(s)} = \frac{\frac{R_f}{L_m}\frac{1}{L_p}}{\left(s + \frac{(R_p + R_f)}{L_p}\right)\left(s + \frac{R_f}{L_m}\right) - \left(\frac{R_f^2}{L_m L_p}\right)} \tag{4.9}$$

To have global vision of the sensitivity of system on parameter (L_m), the impact of magnetizing inductance variation is analyzed on the bode diagram of provided transfer functions. The variation of magnetizing inductance is done based on the acceptable error (from industrial point of view) on I_p at the fundamental frequency which is about 5%. Therefore, the magnetizing inductance is changed for $\pm 10\%$ to have around 5% changes on I_p at fundamental frequency (60 Hz). Figure 4-11 depicts the impact of $\pm 10\%$ variation of the magnetizing inductance on the gain and phase of transfer functions of $\frac{I_p(s)}{U_{cat_2}(s)}$ and $\frac{I_m(s)}{U_{cat_2}(s)}$ respectively. The impact of magnetizing inductance variation on $\frac{I_m(s)}{U_{cat_2}(s)}$ is also shown even if the only state variable that can be measured on test bench is $I_p(t)$. This result is presented just to have a global vision of magnetizing inductance variation of other state variables of transformer. The normal value of magnetizing inductance is considered to be 5 mH based on the datasheet.

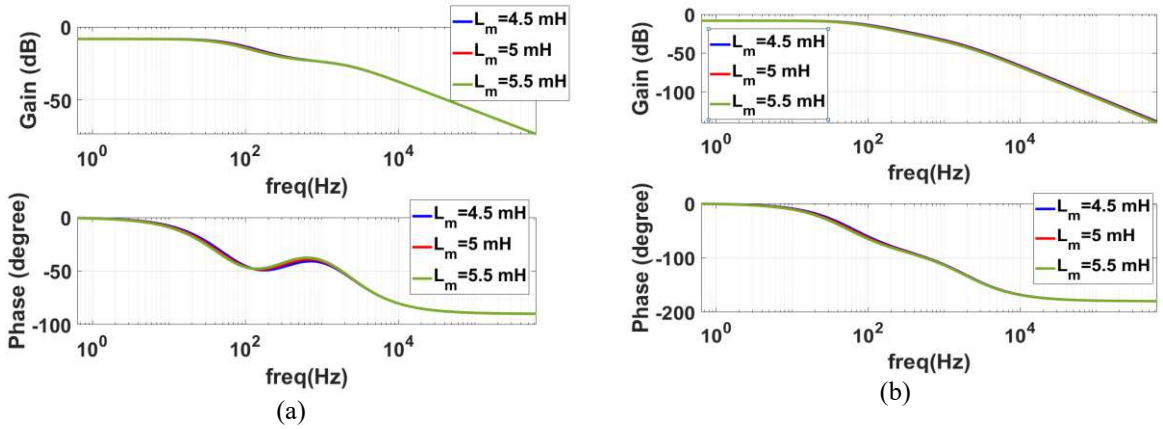

Figure 4-11 Bode diagram of transfer function (a) $\frac{I_p(s)}{U_{cat_2}(s)}$ (b) $\frac{I_m(s)}{U_{cat_2}(s)}$

The phase figure of I_p depicts that for high frequencies, it is stable and constant on -90 degree as there are 2 poles and one zero in its transfer function (4.8). The phase figure of I_m also is goint to be -180 degree for high frequencies as there are 2 poles in its transfer function (4.9). The value of I_p and I_m at the fundamental frequency (60 Hz) can be extracted from figure 4-11. The relative error of I_p and I_m are presented graphically in the figure 4-12.

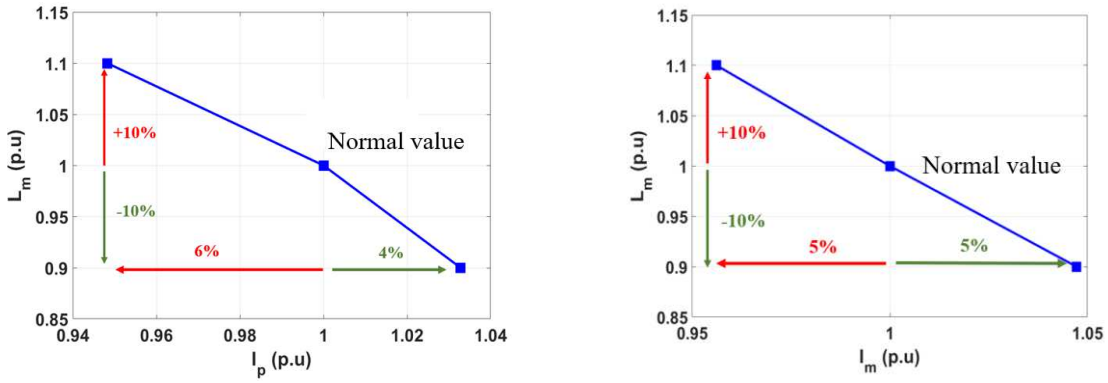

Figure 4-12 Magnetizing inductance variation effect on fundamental frequency of the state variables

In this figure the normal value of L_m, I_p and I_m are denoted by 1. It is shown that by changing 10% of magnetizing inductance from its normal value, the primary current I_p and magnetizing current I_m at fundamental frequency changes around 5% from its normal point. Note that the variation on magnetizing inductance is considered while other parameters are set on their normal value. Now, the sensitivity of L_m nonlinear model parameters on the value of L_m and system output, $I_p(t)$ are important to know. The nonlinear model of L_m obtained using JA method. Therefore, the sensitivity analysis is done on primary current, $I_p(t)$ considering the variations of Jiles-Atherton parameters, in the following section. This allows us to have the global vision of all the parameters and find out the most sensitive parameters in the calculation of primary current.

4.3.3.2. Numerical Estimation and Design of Experiments on transformer model

As it is presented in chapter 2 and 3, to calculate the magnetizing current in steady and transient states, it is needed to have four Jiles Atherton parameters (a, k, c and α). Four Jiles-Atherton parameters are obtained by identification process and it is desired to analyze the sensitivity of primary current on these parameters. Note that the sensitivity analysis is done considering the transformer with isolated secondary and in the test bench condition. To calculate the sensitivity function for all combination of parameters, the DOE method is applied. All the procedures are described in detail for both cases in the following.

As there are four parameters, 2^4 full factorial experiments are created. Therefore, to do the sensitivity analysis, the impact of four individual parameters and their interactions: each 2

parameters (6 combinations), each 3 parameters (4 combinations), 4 parameters (1 combination) have to be studied on the output of transformer. The example of [85] is considered. In this example, the transformer is in the transient state. Therefore, based on the explanations provided in chapters 2 and 3, the JA model has good accuracy in this condition. The output function f, taken as an indicator is the amplitude of the first peak of primary current (Inrush in transient state), $I_{p_{max}}$.

The elements are assigned as -1 and +1 values which represent the -3% and +3% of variation of each parameter from its nominal value respectively (Table 4-3). The ±3% of variation on JA parameters represents about 6% of error on magnetizing inductance value. This causes about 5% of error on the amplitude of first peak in primary current, $I_{p_{max}}$ which mentioned as acceptable error in industrial point of view in the previous section 4.3.3.1.The amplitude of first peak in primary current is extracted from simulation for all the combinations. The Table 4-3 depicts the experiments, the simulation results for the combinations and relative error of $I_{p_{max}}$ compare to normal value, denoted as $I_{p_{\max_N}}$ and relative error of calculated magnetizing inductance (L_m) compare to normal value without variation of parameters. Note that the magnetizing inductance is calculated using (2.34). The provided values for inrush current peak are united by $I_{p_{\max_N}}$ when there is no variation on the JA parameters.

Table 4-3 Full 2^4 factorial design experiments of JA parameters and the simulation results for all the combinations

k	a	α	c	**First peak of inrush current ($I_{p_{max}}$) (p.u)**	**Absolute value of error comparing to normal value $I_{p_{max_N}}$ (%)**	**Absolute value of error comparing to normal value of L_m (%)**
-1	-1	-1	-1	1.04	3.9	1.4
-1	-1	-1	1	1.04	4	1.6
-1	-1	1	-1	1.053	5.2	5.9
-1	-1	1	1	1.054	5.2	6.1
-1	1	-1	-1	1.03	3.4	5.8
-1	1	-1	1	1.03	3.4	5.6
-1	1	1	-1	1.04	4.5	1
-1	1	1	1	1.048	4.6	0.8
1	-1	-1	-1	1.039	3.7	0.9
1	-1	-1	1	1.04	3.8	1.1
1	-1	1	-1	1.052	5	5.4
1	-1	1	1	1.053	5.1	5.6
1	1	-1	-1	1.03	3.2	6.3
1	1	-1	1	1.035	3.3	6.1
1	1	1	-1	1.04	4.3	1.6
1	1	1	1	1.046	4.4	1.3

As explained in the previous sections, to represent the experiment results, equation (4.5) has to be defined. In this case, the equation (4.5) will be rewritten as below for 16 experiments:

$$y \sim I_{p_{\max_N}} + S_a^{I_{pmax}} a + S_k^{I_{pmax}} k + S_c^{I_{pmax}} c + S_\alpha^{I_{pmax}} \alpha + S_{ak}^{I_{pmax}} (ak) + S_{ac}^{I_{pmax}} (ac) + S_{k\alpha}^{I_{pmax}} (k\alpha) + S_{\alpha c}^{I_{pmax}} (\alpha c) + S_{a\alpha}^{I_{pmax}} (a\alpha) + S_{kc}^{I_{pmax}} (kc) + S_{akc}^{I_{pmax}} (akc) + S_{kc\alpha}^{I_{pmax}} (kc\alpha) + S_{a\alpha c}^{I_{pmax}} (a\alpha c) + S_{akc\alpha}^{I_{pmax}} (akc\alpha) \quad (4.10)$$

where it is required to calculate the 14 sensitivity functions: $S_a^{I_{pmax}}$, $S_k^{I_{pmax}}$, $S_c^{I_{pmax}}$, $S_\alpha^{I_{pmax}}$, $S_{ak}^{I_{pmax}}$, $S_{ac}^{I_{pmax}}$, $S_{k\alpha}^{I_{pmax}}$, $S_{\alpha c}^{I_{pmax}}$, $S_{a\alpha}^{I_{pmax}}$, $S_{kc}^{I_{pmax}}$, $S_{akc}^{I_{pmax}}$, $S_{kc\alpha}^{I_{pmax}}$, $S_{a\alpha c}^{I_{pmax}}$ and $S_{akc\alpha}^{I_{pmax}}$. As it is mentioned in the section 4.3.2, a, k, c and α are defined on a coded scale from -1 to +1 (the low and high levels of a, k, c and α). In the two following subsections, the sensitivity functions are obtained for individual and interaction parameters.

4.3.3.2.1. Impact of individual parameters

To calculate the effect of each JA parameter, the definition of sensitivity functions is used. To do so, the equation (4.4) can be rewritten as (4.11) for parameter a as an example. Please note that due to several experiments for one scenario, the average of output response is considered for each level.

$$S_a^{I_{pmax}} = \frac{\overline{I_{p_{max}}(a=1)} - \overline{I_{p_{max}}(a=-1)}}{(a=1)-(a=-1)} \tag{4.11}$$

where $\overline{I_{p_{max}}(a=1)}$, $\overline{I_{p_{max}}(a=-1)}$, are the average of maximum value of primary current when the value of the parameter a get +3% and -3% respectively. $(a=1)$ and $(a=-1)$ are the values of a with +3% of variation and -3% respectively. In this case the simulation has to be run for $2^3 = 8$ experiments for each level of a because three other parameters take 2 values. Table 4-4 depicts the rearranged Table 4-3 in order to calculate the parameter of equation (4.11).

Table 4-4 The rearranged of Table 4-3 to calculate the parameters of equation (4.12)

Scenario	$\boldsymbol{I_{p_{max}}(p.u)}$								$\boldsymbol{\overline{I_{p_{max}}}(p.u)}$
$(a=-1)$	1.0413	1.042	1.053	1.054	1.039	1.04	1.05	1.05	1.0473
$(a=+1)$	1.035	1.036	1.047	1.048	1.034	1.035	1.045	1.04	1.0413

As a matter of facts; applying equation (4.11) leads to:

$$S_a^{I_{pmax}} = \frac{1.0413 - 1.0473}{0.03 - (-0.03)} = -0.1504 \tag{4.12}$$

The effects of other parameters are calculated in the same way as parameter a. The results are presented in Table 4-5.

Table 4-5 The effect of each JA parameter on the maximum peak of primary current

Sensitivity function	$\boldsymbol{S_k^{I_{pmax}}}$	$\boldsymbol{S_a^{I_{pmax}}}$	$\boldsymbol{S_\alpha^{I_{pmax}}}$	$\boldsymbol{S_c^{I_{pmax}}}$
Values	-0.0443	-0.1504	0.302	0.026

Table 4-5 demonstrates that parameter α and a have the most impact on the $I_{p_{max}}$ comparing to other individual parameters. In order to represent graphically the effect of each parameters on $I_{p_{max}}$, figure 4-13 is provided. This figure demonstrates that by changing each parameter from low to high level, how much the variation of the maximum value of current peak is. The slope

of each line (which is the calculated sensitivity functions in Table 4-5) for each parameter help us to understand easily and visually the impact of each parameter on the output.

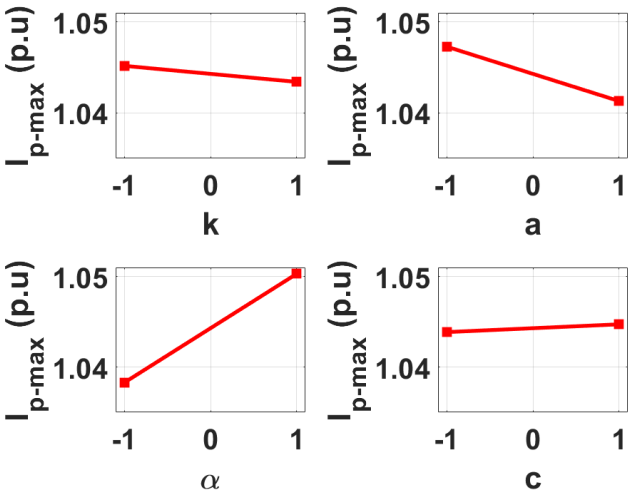

Figure 4-13 The main effect of Jiles Atherton parameters

Figure 4-13 illustrates the same conclusion as the one obtained from Table 4-5 that the parameters α and a have the largest impact on $I_{p_{max}}$ due to the highest line slope. In next subsection the parameter interactions are analyzed in detail.

4.3.3.2.2. Impact of parameter interactions

As it is mentioned in the previous section, the DOE is also helpful to know the effect of interactions between the parameters in a design and how these interactions affect the variation in the output of system. In this case the elements of equation (4.11) have to be changed. As an example, to calculate the sensitivity function to know the impact of interaction between parameters a and α, equation (4.13) is provided as below:

$$S_{a\alpha}^{I_{p_{max}}} = \frac{\overline{I_{p_{max}}(a\alpha = 1)} - \overline{I_{p_{max}}(a\alpha = -1)}}{(a\alpha = 1) - (a\alpha = -1)} \tag{4.13}$$

The Table 4-3 is rearranged to calculate the average of $I_{p_{max}}$ while $a\alpha = -1$ and $a\alpha = 1$. Table 4-6 depicts the results.

Table 4-6 The rearranged of Table 4-3 to calculate the parameters of equation (4.14)

Scenario	$I_{p_{max}}(p.u)$								$\overline{I_{p_{max}}}\ (p.u)$
$(a\alpha = -1)$	1.053	1.054	1.035	1.036	1.052	1.053	1.034	1.035	1.0445
$(a\alpha = +1)$	1.041	1.042	1.047	1.048	1.039	1.04	1.045	1.046	1.0441

Considering equation (4.13), $S_{a\alpha}^{I_{p_{max}}}$ is -0.0107. Table 4-6 depicts the sensitivity function results for other interactions ($a\alpha, ac, ak, ck, k\alpha$ and $c\alpha$).

Table 4-7 The effect of parameter interactions on the maximum peak of primary current

Sensitivity function	$S_{a\alpha}^{I_{pmax}}$	$S_{ak}^{I_{pmax}}$	$S_{ac}^{I_{pmax}}$	$S_{k\alpha}^{I_{pmax}}$	$S_{c\alpha}^{I_{pmax}}$	$S_{kc}^{I_{pmax}}$
Values	-0.0107	0.0011	-3.6^{e-4}	-4.9^{e-4}	6.7^{e-5}	6.7^{e-4}

The values presented in Table 4-7 shows that the parameters (a with α) has the highest interactions between each two parameters comparing other interactions. These results can be illustrated graphically. The same graphical representation as figure 4-13 can be provided as figure 4-14.

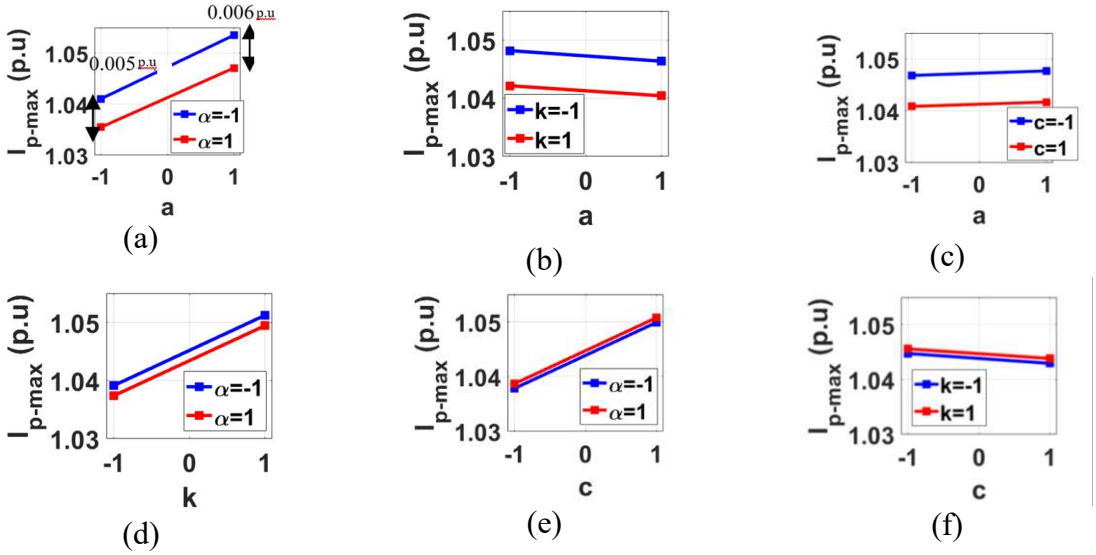

Figure 4-14 Interaction plots between parameters (a) (a with α) , (b) (a with k), (c)(a with c) , (d) (k with α) (e) (c with α) and (f) (c with k)

These figures plot the response data of each parameters against both level of another parameter. As an example, in figure 4-14(f), while parameter c is changing from low to high level, the lines corresponding to parameter k does not have any interaction neither in low nor high level with parameter c. This is deducted from two parallel lines in figure 4-14 (f). This conclusion is the same for parameters of (k with a), (a with c), (k with α), (c with α) and (c with a). However, as shown in figure 4-13 (a), there are small interactions between parameters (a with α) due to unparallel lines (it is shown in the figure 4-14 (a) by providing the differences between lines in low which is 0.005 p.u and high level which is 0.006 p.u). These results also emphasize the conclusion of Table 4-7.

The same procedure is applied to see the interaction impacts between three and four parameters. The results are presented in Table 4-8.

Table 4-8 The effect of parameter interactions (3 and 4 parameters) on $I_{p_{max}}$

Sensitivity function	$S_{akc}^{I_{pmax}}$	$S_{\alpha kc}^{I_{pmax}}$	$S_{\alpha ac}^{I_{pmax}}$	$S_{\alpha ak}^{I_{pmax}}$	$S_{\alpha akc}^{I_{pmax}}$
Values	-1.59^{e-5}	5.17^{e-6}	2.07^{e-5}	-3.49^{e-5}	5.48^{e-7}

The calculation of sensitivity functions shows that JA parameter interactions between two, three and four parameters do not have great impact on $I_{p_{max}}$.

4.3.3.2.3. Sensitivity analysis summary

In this section, the sensitivity analysis was provided on primary current of transformer as the traction system representative output that can be measured on test bench. It is shown that having about 6% of error on magnetizing inductance can have 5% of error on primary current. As the magnetizing inductance characteristics are obtained using JA model, the effect of variation of JA parameters on magnetizing inductance was studied. The impact of individual JA parameters and interaction between them were presented. It was shown that the impact of JA parameters interactions is negligible compare to the impact of individual JA parameters. It is demonstrated that the 3% variation on JA parameters individually can have an impact on $I_{p_{max}}$ about 5%. Among the JA parameters, parameters a and α has the highest impact on the L_m and $I_p(t)$ consequently. To have global vision of the impact of parameters on the $I_{p_{max}}$, the obtained results of sensitivity functions can be replaced in equation (4.10) as equation (4.14).

$$y \sim I_{p_{max_N}} - 0.1504a - 0.0443k + 0.026c + 0.302\alpha + 0.0011(ak) - 3.6^{e-4}(ac) - 4.9^{e-4}(k\alpha) + 6.7^{e-5}(\alpha c) - 0.0107(a\alpha) + 6.7^{e-4}(kc) - 1.59^{e-5}(akc) + 5.17^{e-6}(kc\alpha) - 3.49^{e-5}(a\alpha c) + 5.48^{e-7}(akc\alpha) \quad (4.14)$$

As the sensitivity functions for parameter interactions are neglectable comparing to individual parameters, the equation (4.14) is simplified by considering the effect of individual parameters as below:

$$y \sim I_{p_{max_N}} - 0.1504a - 0.0443k + 0.026c + 0.302\alpha \quad (4.15)$$

This equation can provide the impact of variation of each parameter on $I_{p_{max_N}}$. Please notice that a, k, c and α are defined on a coded scale from -1 to +1 (the low and high levels of a, k, c and α).

Let us remind that the required accuracy to have a representative model of traction subsystem models on real time simulator is defined less than 5% of error comparing to measurements. This target accuracy is considered in parameter identification process. The results in sensitivity analysis on identified parameters give us a vision on impact of having error on identified parameters on the state variables of subsystem model. The results provided in this chapter demonstrates that having the error less than 3% on JA parameters can ensure the required accuracy of subsystem model.

4.4. Conclusion

In this chapter, the compatibility of proposed model is validated by comparing the simulation results and measurements on test bench. It is demonstrated that the nonlinear transformer model has good accuracy to predict the system behavior in various operating point on test bench. Its representability is also approved by comparing with the old model response and measurements. The compatibility of proposed model for asynchronous motor within overall traction system model is also validated. Due to experimental constraints, we had some specific points to do the comparison.

To validate the proposed models and analyze the sensitivity of model parameters, the sensitivity analysis is done using the sensitivity functions and design of experiments. Due to the complexity of proposed models, the empirical sensitivity functions using numerical determination are applied. To analyze the sensitivity of all the parameters combinations and their interaction, design of experiment is used. The graphical interpretation of the impact of each parameter are provided thanks to this methodology.

As a first step of sensitivity analysis, the state variables impacted by nonlinear parameters are detected thanks to the bond graph methodology. Among all these state variables, the stator current of motor and primary current of transformer are the variables that can be measured on test bench. As the primary current of transformer is the output variable and representative of traction system, the sensitivity analysis is done on this variable considering the nonlinear parameter. Thanks to the bond graph methodology, it is shown that the nonlinear parameters of asynchronous motor does not have direct impact on primary current of transformer and its effect is negligible. Therefore, the sensitivity analysis is done on primary current of transformer considering the nonlinear parameter of transformer which is magnetizing inductance.

The transfer function of transformer is provided thanks to the causal paths between source and energy variables of storage elements (leakage and magnetizing inductance). The effect of magnetizing inductance variation is studied on the primary current and magnetizing current using bode diagram. Thanks to the bode diagram of state variables, it is deducted that 10% error on magnetizing inductance can impact the primary and magnetizing current of transformer about 5% at the fundamental frequency. As the primary current is the only state variable of transformer, which is possible to be measured on test bench, the sensitivity analysis is done considering the primary current as the output of system. Then, the impact of 3% variation on the four Jiles-Atherton parameters are determined on the maximum peak of primary current in transient state. The 3% variation on JA model parameters represent about 6% of error on magnetizing inductance which results less than 5% error on primary current of transformer at first peak in transient state. It is deducted that the two parameters of a, α have the most impact on the output compare to the other factors. The JA parameter interaction impacts are neglectable comparing the effect of individual parameters.

Chapter 5

Conclusions and perspectives

Conclusion

This thesis was done under support of national association research technology (Agence Nationale de la Recherche et de la Technologie - ANRT) and funding from the Shift2Rail Joint Undertaking (JU) under grant agreement No 826054.

This research aimed to improve the electrical model of traction system in railway conversion chain design. The purpose is to design accurate model that can be implemented on real time simulator. Having an accurate simulation model of traction system component is necessary to reduce the cost in validation and verification process. The components models are then used in a simulation process to test several risk occurrences, previously to verification procedures. The simulated models should consist of physical phenomena considering exchanged energies. To be implemented in real time simulators as a part of a whole traction system, the proposed models had been simple enough as well.

This thesis was organized as following: As a first step, the weak points of initial traction system components models were highlighted in chapter 1. In chapter 2, a methodology was used to present the energy transfers and obtain the system equations. Then, the traction system component models were improved regarding their limitations. The proposed system models were simulated and validated separately in chapter 3 using the identified parameters. The compatibility of proposed model in overall traction system model is validated by comparing the results with measurements in chapter 4. Finally, the sensitivity analysis is provided to show the effect of identified parameters on the system output.

The limitations of traction system components model were detected by comparing the measurements on real time simulator and experimental one. It was obtained that to improve the components model, the nonlinear parameters in traction components had to be considered. In this thesis, it was focused on four models of traction system components based on Alstom needs: Asynchronous motor, pantograph bounce, transformer and PEM fuel cell. The parameters with nonlinear characteristic were the magnetizing inductance in asynchronous motor, the arc resistance in pantograph bounce, the magnetizing inductance in transformer and PEM fuel cell model parameters.

The bond graph methodology was used to represent the power flow between subsystems of the traction system. Thanks to this methodology, the state equations of desired traction subsystem were provided considering energy links. The link between sources as input and energy variables of storage elements as output were presented which leads us to provide the sensitivity analysis using transfer function of a system.

The asynchronous motor model was improved considering the variation of magnetizing inductance based on state variable. The bond graph methodology leads to achieve the state equations of the system that can be easily simulated on real time simulator. The magnetizing inductance model parameters were obtained using the datasheet of motor. The effect of

magnetizing variation was on stator current. The improved model of asynchronous motor reduced 7% of the difference between simulation and measurements achieved on test bench. It illustrated the necessity of considering magnetizing inductance variation in model. Let us remind that the validation was achieved based on specific project (parameters values) and specific operating conditions.

The pantograph bounce considering arc phenomenon was modeled inside a complex traction system. The major effects of pantograph bounce are on the input of traction system: primary voltage and current of transformer. The effect of train speed and the variation of disconnection length were considered in the arc model. The voltage spike on the primary current of the transformer was used to identify the arc model parameters. Comparison between measurements on train and simulation results shown that presented model was sufficiently accurate to predict the behavior of the whole system during pantograph bounce phenomenon. It was shown that zero crossing point of current were perfectly predicted thanks to modeling of the whole power chain.

The train input power chain including nonlinear transformer was modeled using bond graph representation. The simulation scheme based on state space equation were obtained to accurately simulate the behavior of input power chain. The model of transformer considered the nonlinearity of magnetizing inductance using two proposed methods; the rewritten Jiles-Atherton model and combination of Jiles-Atherton and curve fitting method. The rewritten Jiles-Atherton model was proposed to avoid the algebraic loop while state equations solved. This is an important point to be solved as the Jiles-Atherton model will be implemented on real time simulator in next step. Due to non-ideal test conditions, analyses were done considering the entire and uncomplete hysteresis cycle in parameter identification process. It was shown that the Jiles-Atherton parameter identification can be done with part of the hysteresis cycle considering the extremum point and coercive field. Then, the parameter identification was performed on the transformer included on a test bench, of a railway traction system. The simulated hysteresis cycle and magnetizing current were compared with the measurements and shown a great accuracy. This thesis demonstrated that few measurements are needed to completely and precisely identify parameters of the power transformer in order to simulate it. Nevertheless, to enforce our transient and steady state model, an improvement was needed to model energization stage. To accurately simulate the magnetizing inductance behavior in deep saturation region, the curve fitting method was proposed. It was shown that nonlinear characteristics of magnetizing inductance can be extracted from the experimental measurements in worth condition (high value of inrush current). The complete model of magnetizing inductance was proposed. Comparison of simulation results and experimental measurements demonstrated a great accuracy of proposed model in steady state, transient state and deep saturation region.

The PEM fuel cell system was modeled using the average experimental profile mission. This method leads to have a simplified model of overall system in user point of view in order to be easily simulated in railway application. The parameters of model were identified using the

experimental average polarization curve. The two major characteristics of system in various operating modes were simulated using the dynamic model. Comparison between experimental measurements on train and simulation results depicts that the presented model sufficiently accurate to predict the behavior of PEM fuel cell system.

To validate the compatibility of proposed model in overall traction system, the simulation was done including the control and traction system with developed models. The comparison between simulation and test bench results demonstrates that proposed model is compatible and accurate enough to predict the behavior of each subsystem inside the traction system.

The sensitivity analyses are done on the transformer model to have a global vision of the effect of each parameter in nonlinear elements in model on the traction system output which is primary current of transformer. The process of sensitivity analysis done on transformer model is applicable on the other three models.

Future Work

As short-term researches, I have found that it would be interesting to do the sensitivity analysis on asynchronous motor, pantograph bounce and PEM fuel cell system individually which can indicate the most important parameters that have great impact on each traction subsystem. My second proposition as a short-term research is to implement the pantograph bounce model in overall traction system simulation. This will permit us to validate the model in overall traction system model and in the second step, the control system performance can be verified during the electrical arc occurrence. The model verification inside overall system model is also suggested for PEM fuel cell. It is also suggested to finalize the validation proposed models on real time simulator.

As mid-term researches, it is suggested to implement do the sensitivity analysis considering the nonlinear elements of traction system (rectifiers (AC/DC), inverters (DC/AC)).

As long-term researches, I suggest improving the model of catenary as a first proposition. The catenary model can be improved by several π model which can represent accurately the impedances between the substation and train. As a second proposition, it would be interesting to improve the converters models in order to best take into account new technologies of semiconductors as silicon carbide (SiC) materials and nonlinear elements of system model. As a third proposition, I suggest also improving the energy storage system (ESS) including fuel cell and battery on real time simulator to improve its representativity for hybrid trains.

Appendix

Supplementary information is provided as below:

A.1. ASM

A.1.1 Clarke transform :

The Clarke transformation matrix is as following.

$$\begin{bmatrix} V_\alpha \\ V_\beta \\ V_0 \end{bmatrix} = \left(\frac{2}{3}\right) \begin{bmatrix} 1 & -\frac{1}{2} & -\frac{1}{2} \\ 0 & \frac{\sqrt{3}}{2} & -\frac{\sqrt{3}}{2} \\ \frac{1}{\sqrt{2}} & \frac{1}{\sqrt{2}} & \frac{1}{\sqrt{2}} \end{bmatrix} \begin{bmatrix} V_a \\ V_b \\ V_c \end{bmatrix} \quad \text{A.1.1}$$

In the balanced three phase system, three phases have the same amplitudes and they have $-\frac{2\pi}{3}$ difference in phases. So, $V_a + V_b + V_c = 0$ and the Clarke transformation will be simplified as (A.1.2).

$$\begin{bmatrix} V_\alpha \\ V_\beta \end{bmatrix} = \left(\frac{2}{3}\right) \begin{bmatrix} 1 & -\frac{1}{2} & -\frac{1}{2} \\ 0 & \frac{\sqrt{3}}{2} & -\frac{\sqrt{3}}{2} \end{bmatrix} \begin{bmatrix} V_a \\ V_b \end{bmatrix} \quad \text{A.1.2}$$

A.1.2 Electrical equations of ASM

The basic electrical equations of ASM are explained as following:

$$V_{s_\alpha}(t) = R_s I_{s_\alpha}(t) + \frac{d\phi_{s_\alpha}(t)}{dt} \quad \text{A.1.3}$$

$$V_{s_\beta}(t) = R_s I_{s_\beta}(t) + \frac{d\phi_{s_\beta}(t)}{dt} \quad \text{A.1.4}$$

$$V_{r_\alpha}(t) = R_r I_{r_\alpha}(t) + \frac{d\phi_{r_\alpha}(t)}{dt} + \omega(t)\phi_{r_\beta}(t) = 0 \quad \text{A.1.5}$$

$$V_{r_\beta}(t) = R_r I_{r_\beta}(t) + \frac{d\phi_{r_\beta}(t)}{dt} - \omega(t)\phi_{r_\alpha}(t) = 0 \quad \text{A.1.6}$$

where $\phi_{s_\alpha}(t), \phi_{s_\beta}(t), \phi_{r_\alpha}(t)$ and $\phi_{r_\beta}(t)$ are as below:

$$\phi_{s_\alpha}(t) = L_s I_{s_\alpha}(t) + L_m I_{r_\alpha}(t) \quad \text{A.1.7}$$

$$\phi_{s_\beta}(t) = L_s I_{s_\beta}(t) + L_m I_{r_\beta}(t) \quad \text{A.1.8}$$

$$\phi_{r_\alpha}(t) = L_r I_{r_\alpha}(t) + L_m I_{s_\alpha}(t) \quad \text{A.1.9}$$

$$\phi_{r_\beta}(t) = L_r I_{r_\beta}(t) + L_m I_{s_\beta}(t) \quad \text{A.1.10}$$

where L_s and L_r are the stator and rotor cyclic inductance, which are $L_s = L_1 + L_m$ and $L_r = L_2 + L_m$ respectively.

A.1.3 The equivalent expression for ASM by transferring rotor in stator

The equivalent ASM model parameters by transferring the rotor elements to stator parts are as below:

$$\sigma = 1 - \frac{L_m^2}{L_s L_r} \quad \text{A.1.11}$$

$$R_r' = \left(\frac{L_m}{L_r}\right)^2 R_r \quad \text{A.1.12}$$

$$L_m' = \frac{L_m^2}{L_r} \quad \text{A.1.13}$$

$$F_{EM}'(t) = \frac{L_m}{L_r} F_{EM}(t) \quad \text{A.1.14}$$

where $F_{EM,\alpha}(t) = \omega \phi_{r\beta}(t)$ and $F_{EM,\beta}(t) = -\omega \phi_{r\alpha}(t)$.

Current and flux of rotor will be transferred to stator part by the expressions as below:

$$I_r'(t) = \frac{L_r}{L_m} I_r(t) \quad \text{A.1.15}$$

$$\phi_r'(t) = \frac{L_m}{L_r} \phi_r(t) \quad \text{A.1.16}$$

A.1.4 Electromagnetic torque

The electromagnetic torque of ASM obtained by:

$$T_{em}(t) = P_p(\frac{L_m}{L_r})(\phi_{r_\alpha}(t) I_{s_\beta}(t) - \phi_{r_\beta}(t) I_{s_\alpha}(t)) \quad \text{A.1.17}$$

Considering all the transferred expressions in equations (A.1.11)- equation (A.1.14), (A.1.17) can be changed as below:

$$T_{em}(t) = P_p(\phi_{r_\alpha}'(t) I_{s_\beta}(t) - \phi_{r_\beta}'(t) I_{s_\alpha}(t)) \quad \text{A.1.18}$$

A.1.5 Magnetizing inductance equation

Magnetizing inductance basic equation:

$$\emptyset_m(t) = L_m I_m(t) \quad \text{A.1.19}$$

A.2. Pantograph bounce

A.2.1 The detachment length

The detachment length of pantograph and catenary:

$$L_{arc}(t) = \frac{L_1}{t_1 - t_{start}}(t - t_{start}) \qquad if \qquad t_{start} \le t \le t_1$$
$$L_{arc}(t) = \frac{L_2}{t_2 - t_{end}}(t - t_{end}) \qquad if \qquad t_2 \le t \le t_{end} \qquad \text{A.2.1}$$

In the case of having no arc extinguished region:

$$L_{arc}(t) = \frac{L_{max}}{t_{L_{max}} - t_{start}}(t - t_{start}) \qquad if \qquad t_{start} \le t \le t_{L_{max}}$$
$$L_{arc}(t) = \frac{L_{max}}{t_{L_{max}} - t_{end}}(t - t_{end}) \qquad if \qquad t_{L_{max}} \le t \le t_{end} \qquad \text{A.2.2}$$

A.2.2 Dissipated power of arc

Experimental equation of dissipated power of arc considering blowing speed and arc diameters:

$$p = k_1 d(v + a)^{1.5} \qquad \text{A.2.3}$$

where d, v, k_1 and a are arc diameter, speed of train, correlation coefficient of dissipated power for arc and constant coefficient which should be identify based on experimental data, respectively. In the case of moving with speed more than v_0, d can be expressed by speed and arc current as A.2.4 [55].

$$d = b\sqrt{\frac{I_p}{v + a}} \qquad \text{A.2.4}$$

By substitution of A.2.4 into A.2.3, the total dissipated power will be as below:

$$P_0(t) = p * L_{arc}(t) = k_1 b(v + a)\sqrt{I_p} L_{arc}(t) \qquad \text{A.2.5}$$

A.3. Transformer

A.3.1 Basic relations of transformer

Voltage and current relations in primary and secondary in ideal transformer.

$$k = \frac{E_p}{N_p} = \frac{E_s}{N_s} \quad \text{A.3.1}$$

$$k = I_p N_p = I_s N_s \quad \text{A.3.2}$$

where E is the induced voltage and N is the number of turns in the windings identified by appropriate subscript.

A.3.2 Conductor losses

The total conductor loss in nonlinear transformer:

$$R = R_{DC} + R_{eddy} + R_{Stray} + R_{Skin} \quad \text{A.3.3}$$

A.3.3 Core losses

Core losses depending on the instant of contactor closure and residual flux in transformer:

Let us consider a sinusoidal voltage ($U(t) = U_m \sin(\omega t)$) is applied on primary of transformer (Figure A.3.1) while the secondary is open. The magnetic flux will be produced based on Faraday's law in the core.

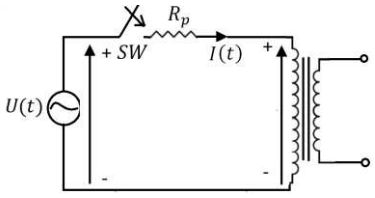

Figure A.3.1 Linear inductor

$$\dot{\emptyset}(t) = -\frac{U(t)}{N} \quad \text{Or} \quad \emptyset(t) = -\frac{1}{N}\int U(t)\,dt \quad \text{A.3.4}$$

If the voltage is applied at *t=0*, the flux can be obtained as below:

$$\emptyset(t) = -\frac{1}{N}\int U(t)dt = \frac{U_m}{\omega N}\cos(\omega t) + \frac{U_m}{\omega N} \qquad \text{If } @t = 0 \quad \emptyset(0) = 0 \quad \text{A.3.5}$$

$$\emptyset(t) = -\frac{1}{N}\int U(t)dt = \frac{U_m}{\omega N}cos(\omega t) + \frac{U_m}{\omega N} + C \qquad \text{If } @t = 0 \quad \emptyset(0) = C \quad \text{A.3.6}$$

In this case, the transformer may experience a flux that may reach up to twice its nominal steady state value [147] and [92] that during energization. In the case of feeding $U(t) = U_m \cos(\omega t)$ at *t=0* or on the other word, $U(t) = U_m \sin(\omega t)$ at $t = \frac{\pi}{2}$, the flux equation will be (A.3.7).

$$\emptyset(t) = -\frac{1}{N}\int U(t)dt = \frac{U_m}{\omega N}\sin(\omega t) + C \qquad \text{If } @t = 0 \quad \emptyset(0) = C \tag{A.3.7}$$

where C is residual flux in transformer.

A.3.4 Faraday's law

The magnetic induction can be expressed using Faraday's law as below:

$$\dot{B}(t) = -\frac{U_L(t)}{NS}. \tag{A.3.8}$$

where S is the cross-section area of the primary winding supposing that B is constant within the whole cross-section area.

A.3.5 Amper theorem:

Amper theorem is as below:

$$I_m(t) = H(t).\frac{l}{N}. \tag{A.3.9}$$

A.3.6 Magnetizing current:

The experimental magnetic flux and magnetizing current can be easily obtained using (A.3.4) and (A.3.8).

$$I_m(t) = I_p(t) - \frac{N}{R_f}\frac{d\emptyset_m(t)}{dt} \tag{A.3.10}$$

A.4. PEMFC

A.4.1 Electrochemical reactions

The electrochemical reaction that happens in anode part is as below:

$$H_2 = 2H^+ + 2e^- \tag{A.4.1}$$

The chemical reactions in cathode part is described in equation (A.4.2):

$$2H^+ + \frac{1}{2}O_2 + 2e^- \rightarrow H_2O \tag{A.4.2}$$

Finally, the total reactions happen in the cell is as (A.4.3):

$$2H_2 + \frac{1}{2}O_2 \rightarrow H_2O + heat + electricity \quad \text{A.4.3}$$

The total chemical reactions between hydrogen, oxygen and finally water, can be express by Gibbs free energy as below [148]:

$$\Delta G = \Delta G_{product} - \Delta G_{reactants} = \Delta G_{H_2O} - \Delta G_{H_2} - \Delta G_{O_2} \quad \text{A.4.4}$$

Where ΔG_{H_2}, $\Delta G_{O_2}$and ΔG_{H_2O} are the chemical potential of hydrogen, oxygen and water respectively and can be obtained by:

$$\Delta G_{H_2} = \Delta G^0_{H_2} - RTln(P_{H_2}) \quad \text{A.4.5}$$

$$\Delta G_{O_2} = \Delta G^0_{O_2} - \frac{RT}{2}ln(P_{O_2}) \quad \text{A.4.6}$$

$$\Delta G_{H_2O} = \Delta G^0_{H_2O} \quad \text{A.4.7}$$

Where $\Delta G^0_{H_2}$, $\Delta G_{O_2}$and $\Delta G^0_{H_2O}$ are standard free enthalpies that can be achieved based the value of enthalpy and entropy in standard condition (T=298 K) shown on table A.4.1 [149].

Table A.4.1 Standard enthalpies and entropies for hydrogen, oxygen, and liquid water

Substance	$\boldsymbol{\Delta H^0}$ $\boldsymbol{(J/mol)}$	$\boldsymbol{\Delta S^0}$ $\boldsymbol{(J/(mol.K))}$
Hydrogen	0	130.684
Oxygen	0	205.138
Water	-285.83×10^3	69.91

Note that standard free enthalpy has a relationship with enthalpy and entropy as below:

$$\Delta G^0 = \Delta H^0 - T\Delta S^0 \quad \text{A.4.8}$$

In the condition of ideal reaction, the Gibbs energy can be transferred to electromotive forces of anode and cathode by the coefficient shown below:

$$E_{anode} = \frac{\Delta G_{H_2}}{nF} \quad \text{A.4.9}$$

$$E_{cathode} = -\frac{\Delta G_{O_2}}{nF} \quad \text{A.4.10}$$

Where n is number of free electrons ($n = 2$ for PEMFC).

A.4.2 Fuel and Oxidant delay

Based on ideal gas equation as (A.4.11), the instantaneous effective partial pressure for species n can be expressed as equation (A.4.13) [119]:

$$pV = NRT \quad \text{A.4.11}$$

Where p, $V$and N are pressure (pascal), volume (m^3) and amount of gas substance (in moles).

$$\frac{V}{RT}\frac{dp_n^*}{dt} = N_n \quad \text{A.4.12}$$

N_n for hydrogen and oxygen can be expressed as equations (A.4.13) and (A.4.14) [119]:

$$N_{H_2} = M_{H_2,in} - M_{H_2,out} - \frac{i}{2F} = M_{H_2,net} - \frac{i}{2F} \quad \text{A.4.13}$$

$$N_{O_2} = M_{O_2,in} - M_{O_2,out} - \frac{i}{4F} = M_{O_2,net} - \frac{i}{4F} \quad \text{A.4.14}$$

Where M_n is mole rate of species n (in mol per second), i current in amperes. The partial pressure is constant during steady state therefore the instantaneous partial pressure would be zero.

$$\frac{dp_n^*}{dt} = 0 \quad \text{A.4.15}$$

Thus, the molar flux rate in net for hydrogen and oxygen can be obtain as (A.4.16) under the steady state condition [119],

$$M_{H_2,net} = 2M_{O_2,net} = \frac{i}{2F} \quad \text{A.4.16}$$

Therefore, to represent the delay of fuel and oxidant, the relationships shown in equations (A.4.17) and (A.2.18) are used based on [119].

$$\tau_a \frac{dM_{H_2,net}}{dt} = \frac{i}{2F} - M_{H_2,net} \quad \text{A.4.17}$$

$$\tau_c \frac{dM_{O_2,net}}{dt} = \frac{i}{2F} - M_{O_2,net} \quad \text{A.4.18}$$

Where τ_a and τ_c are fuel and oxidant delay in second respectively.

A.4.3 Internal potential

Internal potential of PEMFC considering energy links in bond graph and chemical model:

A.4.19

$$E = \frac{\Delta G}{2F} = \frac{(\Delta G^0_{H_2o} - \Delta G^0_{H_2} - \Delta G^0_{O_2}) + RTln(P_{H_2}P^{0.5}_{O_2}))}{2F} = \frac{\Delta G^0}{2F} + \frac{RT}{2F} ln(P_{H_2}P^{0.5}_{O_2}))$$

Considering heat conversion in PEMFC, equation A.4.19 would be modified as below:

A.4.20

$$E_{cell,\ steady\ state} = E^o_{0,cell} - K_E(T - 298) + \frac{RT}{2F} ln(p_{H_2}.p^{*0.5}_{O_2})$$

Where, $E^o_{0,cell}$ is standard reference potential at standard state (298K and 1-atm pressure) and can be obtained as following:

A.4.21

$$E^o_{0,cell} = \frac{\Delta G^0}{2F}$$

and K_E is an empirical constant in calculating E_0 (in volts per Kelvin (1.229 Volt)) and equation (A.4.22) depicts its relationship with standard entropy of total reactions,

A.4.22

$$K_E = \frac{\Delta S^0}{2F}$$

A.4.4 Ohmic law

Basic ohmic law is as following:

A.4.23

$$R_{ohm} = \frac{\rho_m l}{A}$$

A.5. Numerical solutions for the state equations

A.5.1 Basic equation and definitions

As an example, the general solution for a simple function of $g(t)$ in equation (A.5.1) will be as equation (A.5.2):

A.5.1

$$\dot{Y}(t) = g(t)$$

A.5.2

$$Y(t) = \int g(t)\, dt + c$$

where c is a integration constant that can be obtained by specifying $Y(t)$ at some given point.

A.5.2 Euler method

As a first step, let us assume a differential equation as (A.5.3) with initial value of Y_0,

$$Y'(t) = f\big(t, Y(t)\big), \qquad t_0 \le t \le T \tag{A.5.3}$$

$$Y(t_0) = Y_0$$

For solving equation (A.5.3), numerical methods need an approximate solution $y(t)$ at discrete points with step size of h as below:

$$t_0 \le t_1 \le t_2 \le \cdots \le t_N \le T$$

$$t_n = t_0 + nh, \qquad n = 0,1,\dots,N \tag{A.5.4}$$

To have simplified notation of approximate $y(t)$, following expression is used,

$$y(t_n) = y_h(t_n) = y_n, \qquad n = 0,1,\dots,N \tag{A.5.5}$$

The standard derivate approximation (forward difference approximation) is like (A.5.8)

$$Y'(t) \approx \frac{1}{h}[Y(t+h) - Y(t)] \tag{A.5.6}$$

Based on this standard derivative approximation of equation (A.5.3) at $t = t_n$ will obtained as equation (A.5.7),

$$\frac{1}{h}[Y(t_{n+1}) - Y(t_n)] \approx f\big(t_n, Y(t_n)\big), \tag{A.5.7}$$
$$Y(t_{n+1}) \approx Y(t_n) + hf\big(t_n, Y(t_n)\big)$$

Therefore, the Euler's method can be defined as (A.5.8),

$$y_{n+1} = y_n + hf(t_n, y_n), \qquad 0 \le n \le N-1 \tag{A.5.8}$$

The tangent line to the graph of $Y(t_n)$:

$$P(t) = Y(t_n) + f(t_n, Y(t_n))(t - t_n) \tag{A.5.9}$$

which $Y(t_{n+1})$ can be achieved by replacing $t = t_{n+1}$ in (A.5.9).

A.5.3 Trapezoidal method

The integral of $G(t)$ can be obtained as below:

$$\int_a^b G(s)ds = \frac{1}{2}(b-a)[g(a) + g(b)] - \frac{1}{12}(b-a)^3 g''(\xi) \tag{A.5.10}$$

for some $a \leq \xi \leq b$.

By dropping the final error term of equation (A.5.9), the approximate of integral of $G(t)$ will be as equation (A.5.10):

$$\int_a^b G(s)ds = \frac{1}{2}(b-a)[g(a)+g(b)] \quad \text{A.5.11}$$

Using the trapezoidal rule to differential equation of (A.5.3), we obtain equation (A.5.11) [150]:

$$Y(t_{n+1}) = Y(t_n) + \frac{1}{2}h\left[f\left(t_n, Y(t_n)\right) + f(t_{n+1}, Y(t_{n+1}))\right] \quad \text{A.5.12}$$

Where h is the time interval.

The slope of left, right and ideal lines of geometric illustration of Heun method:

$$left\ derivation = f(t_n, y_n) \quad \text{A.5.13}$$

$$right\ derivation = f(t_n + h, y_n + hf(t_n, y_n)) \quad \text{A.5.14}$$

$$ideal\ derivation = \frac{left\ derivation + right\ derivation}{2} \quad \text{A.5.15}$$

References

[1] Vyzikas, Thomas & Greaves, Deborah & Simmonds, Dave & Maisondieu, Christophe & Smith, Helen & Radford, Lisa., "Application of numerical models and codes - Task 3.4.4 MERiFIC project," University of Plymouth, 2014.

[2] Noureen, Subrina & Roy, Vishwajit & Bayne, Stephen., " An Overall Study of a Real-Time Simulator and Application of RT-LAB using MATLAB SimPowerSystems," in *IEEE Green Energy and Smart Systems Conference*, The Pointe (Pyramid), CSULB, Long Beach, CA, 2017.

[3] Roxana Ionutiu, Erich Scheiben, Xinhua Ke, Daniel Stump, Silvia Mastellone, Nikolaos Oikonomou, Didier Cottet, "Need for speed," [Online]. Available: https://library.e.abb.com/public/87271fab927f1facc1257ca900538aa9/34-39%201m423_EN_72dpi.pdf.

[4] H. W. Dommel,, "Digital computer solution of electromagnetic transients in single- and multiphase networks," *IEEE Trans. Power App. Syst.,* Vols. PAS-88, no. 4, pp. 388-399, 1969.

[5] C. Dufour, J. Mahseredjian, and J. Bélanger, "A combined state-space nodal method for the simulation of power system transients," *IEEE Trans. Power Del.,* vol. 26, no. 2, pp. 928-935, 2011.

[6] P. M. Menghal and A. J. Laxmi, "Real time simulation: Recent progress & challenges," in *Proc. Int. Conf. Power, Signals, Controls Comput. (EPSCICON)*, Thrissur, India, 2012.

[7] T. Berry, A. R. Daniels, and R. W. Dunn, "Real time simulation of power system transient behaviour," in *Proc. 3rd Int. Conf. Power Syst. Monitor. Control*, London, U.K, 1991.

[8] Faruque, M.O., Strasser, T., Lauss, G., et al., "Real-time simulation technologies for power systems design, testing, and analysis," *IEEE Power Energy Technol. Syst. J.,* vol. 2, no. 2, pp. 63-73, 2015.

[9] "Real-Time Simulation. [Online]," 2014. Available: http://www.rtds.com.

[10] O. Devaux, L. Levacher, and O. Huet,, "An advanced and powerful real-time digital transient network analyser," *IEEE Trans. Power Del.,* vol. 13, no. 2, pp. 421-426, 1998.

[11] I. Etxeberria-Otadui, V. Manzo, S. Bacha, and F. Baltes,, "Generalized average modelling of FACTS for real time simulation in ARENE," in *Proc. 28th Annu. Conf. IEEE Ind. Electron. Soc. (IECON)*, Seville, Spain, 2002.

[12] R. Krebs and O. Ruhle,, "NETOMAC real-time simulator—A new generation of standard test modules for enhanced relay testing," in *Proc. 8th IEE Int. Conf. Develop. Power Syst. Protection*, Amsterdam, The Netherlands, 2004.

[13] P. Lehn, J. Rittiger, and B. Kulicke, "Comparison of the ATP version of the EMTP and the NETOMAC program for simulation of HVDC systems," *IEEE Trans. Power Del.,* vol. 10, no. 4, pp. 2048-2053, 1995.

[14] L.-F. Pak, M. O. Faruque, X. Nie, and V. Dinavahi,, "A versatile clusterbased real-time digital simulator for power engineering research," *IEEE Trans. Power Syst.,* vol. 21, no. 2, pp. 455-465, 2006.

[15] S. Abourida, C. Dufour, J. Bélanger, G. Murere, N. Lechevin, and B. Yu,, "Real-time PC-based simulator of electric systems and drives," in *Proc. 17th IEEE Conf. Expo. Appl. Power Electron. (APEC)*, Dallas, TX, USA, 2002.

[16] C. Dufour and J. Bélanger,, "A PC-based real-time parallel simulator of electric systems and drives," in *Proc. Int. Conf. Parallel Comput. Elect. Eng. (PARELEC)*, Dresden, Germany, 2004.

[17] C. Dufour and J. Bélanger,, "A real-time simulator for doubly fed induction generator based wind turbine applications," in *Proc. IEEE 35th Annu. Power Electron. Specialists Conf. (PESC)*, Aachen, Germany, 2004.

[18] M. O. Faruque and V. Dinavahi,, "An advanced PC-cluster based realtime simulator for power electronics and drives," in *Proc. IEEE Int. Symp. Ind. Electron. (ISIE)*, Montreal, QC, Canada, 2006.

[19] C. Larose et al., "A fully digital real-time power system simulator based on PC-cluster," *J. Math. Comput. Simul.,* vol. 63, no. 3-5, pp. 151-159, 2003.

[20] G. Sybille and P. Giroux,, "Simulation of FACTS controllers using the MATLAB power system blockset and hypersim real-time simulator," *Proc. IEEE Power Eng. Soc. Winter Meeting,* vol. 1, pp. 488-491, 2002.

[21] F. Guay, J. Cardinal, E. Lemiex, and S. Guerette,, "Digital real-time simulator using IEC 61850 communication for testing devices," in *Proc. CIGRE Canada Conf.*, Montreal, QC, Canada, 2012.

[22] R. Razzaghi, M. Paolone, and F. Rachidi,, "A general purpose FPGA-based real-time simulator for power systems applications,," in *IEEE PES ISGT Europe*, 2013.

[23] Bouscayrol, A. et a, "Teaching drive control using Energetic Macroscopic Representation — Summer schools," in *14th European Conference on Power Electronics and Applications*, 2011.

[24] Bouscayrol (A.), Lhomme (W.), Delarue (P.), Lemaire-Semail (B.), Aksas (S.), "Hardware-in-the-loop simulation of electric vehicle traction systems using energetic macroscopic representation," *Proc. of IEEE-IECON'06,* pp. 5319-5324, 2006.

[25] Dion., C. Commault and J. M., "A comprehensive introduction to the geometric theory of linear multivariable systems," *IEEE Transactions on Education,* vol. 35, p. 92–97, 1992.

[26] Lichiardopol., Stefan, "Study of duality in bond graph models. application to control law synthesis," *Automatic. Ecole Centrale de Lille,* 2007.

[27] G. Gandanegara, X. Roboam, B. Sareni, G. Dauphin-Tanguy, "Modeling and Multi-time Scale Analysis of Railway Traction Systems Using Bond Graphs," in *Proceedings of International Conference on Bond Graph Modeling and Simulation*, 2001.

[28] D.C. Karnopp, R. Rosenberg, A.S. Perelson, "System dynamics: a unified approach," *IEEE Transactions on Systems, Man and Cybernetics,* pp. 724-724, 1976.

[29] B. Trajin, *Analyse et traitement de grandeurs électriques pour la détection et le diagnostic de défauts mécaniques dans les entraînements asynchrones. Application à la surveillance des roulements à billes, Ph.D. thesis,* 2009.

[30] Nerg, Janne & Pyrhönen, J. & Partanen, Jarmo & Ritchie, Ewen., "Induction Motor Magnetizing Inductance Modelling as a Function of Torque," in *ICEM*, Cracow, Poland, 2004.

[31] Yahiaoui A., Boillault F., "2D and 3D Numerical Computation of Electrical Parameters of an Induction Motor," *IEEE Trans. Magn.,* vol. 30, no. 5, pp. 3690-3692, 1994.

[32] Dolinar D., De Weerdt R., Belmans R., Freeman E. M., "Calculation of Two-Axis Induction Motor Model Parameters Using Finite Elements," *IEEE Trans. Energy Conversion,* vol. 12, no. 2, pp. 133-142, 1997.

[33] Zhou P., Gilmore J., Cendes Z., "Finite Element Analysis of Induction Motors Based on Computing Detailed Equivalent Circuit Parameters," *IEEE Trans. Magn.,* vol. 34, no. 5, pp. 3499-3502, 1998.

[34] Yamazaki K., "An Efficient Procedure to Calculate Equivalent Circuit Parameter of Induction Motor Using 3-D Nonlinear Time-Stepping Finite-Element Method," *IEEE Trans. Magn.,* vol. 38, no. 2, pp. 1281-1284, 2002.

[35] Gao & Zhang, Tingting & Wei, Wenfu & Hu, Yi & Wu, Guangning & Zhou, Ning., "A pantograph arcing model for electrified railways with different speeds," *Proceedings of the Institution of Mechanical Engineers, Part F: Journal of Rail and Rapid Transit,* 2017.

[36] Junru Wang and Xueshan Li., "The influence of the load on electrical locomotive to arc," *China Water Transport,* vol. 10, no. 10, p. 107– 112, 2010.

[37] Dong Lei, Guangning WU, Xue-yuan Zhang, etal., "Study on Arc Suppression Method for Pantograph and Overhead Contact Line of High Speed Railway," *Electric Railway,* 2008.

[38] Zongbao Gao, Guangning Wu, Wei Lv, etal., "Research Review of Arc Phenomenon between Pantograph and Catenary in High-speed Electrified Railway," *High Voltage Apparatus,,* pp. 104-108, 2009.

[39] Tianzhi Li ; Guangning Wu ; Lijun Zhou ; Guoqiang Gao ; Wangang Wang ; Bo Wang ; Donglai Liu ; Dajian Li, "Pantograph Arcing's Impact on Locomotive Equipments," *IEEE 57th Holm Conlerence on Electrical Contacts (Holm),* pp. 1 - 5, 2011.

[40] S. Midya, D. Bormann, T. Schutte, and R. Thottappillil, "DC component from pantograph arcing in AC traction system-influencing parameters, impact, and mitigation techniques," *IEEE Trans. on Power Del.,* vol. 53, no. 1, pp. 18-27, 2011.

[41] S. Midya, D. Bormann, T. Schutte, R. Thottappillil, "DC Component rom Pantograph Arcing in AC Traction System - Influencing Parameters, Impact, and Mitigation Techniques," *IEEE Trans. on Electromagnetic Compatibility,* vol. 53, pp. 18-27, 2011.

[42] S. Midya, D. Bormann, T. Schutte, and R. Thottappillil, "Pantograph arcing in electrified railways-mechanism and influence of various parameters-part I: with AC traction power supply," *IEEE Trans. on Power Del.,* vol. 24, no. 4, pp. 1940 - 1950, 2009.

[43] G. N. W. G. Q. G. B. W. Y. C. a. D. L. L. W. G. Wang, "The pantograph-catenary arc test system for high-speed railways," *Journal of the China Railway Society,* vol. 34, no. 4, pp. 22 - 27, 2012.

[44] O. Mayr, "Contribution to the theory of static and dynamic arcs," *Arch. Elec,* vol. 37, no. 1, pp. 589 - 608, 1943.

[45] Y. J. Liu, G. W. Chang, and H. M. Huang, "Mayr's equation-based model for pantograph arc of high-speed railway traction system," *IEEE Trans. on Power Del,* vol. 25, no. 3, pp. 2025 - 2027, 2010.

[46] Y. Wang, "An Extended Habedank's Equation-Based EMTP Model of Pantograph Arcing Considering Pantograph-Catenary Interactions and Train Speeds," *IEEE Trans. on Power Del,* vol. 31, pp. 1186-1194, 2016.

[47] Y. Wang, Z. G. Liu, F. Q. Fan, and S. B. Gao, "Review of research development of pantograph-catenary arc model and electrical characteristics," *Journal of the China Railway Society,* vol. 35, no. 8, pp. 35 - 43, 2013.

[48] U. Habedank, "On the mathematical-description of arc behavior in the vicinity of current zero," *Etz. Archiv,* vol. 10, no. 11, pp. 339 - 343, 1988.

[49] M. T, Cassie, and D. B. Fang, "An Improved arc model before current zero based on the combined Mayr and Cassie arc models," *IEEE Trans. on Power Del,* vol. 20, no. 1, pp. 138 - 142, 2005.

[50] W. Wei, J. Wu, G. Gao, Z. Gu, X. Liu, G. Zhu, G. Wu, "Study on Pantograph Arcing in a Laboratory Simulation System by High-Speed Photography," *IEEE Trans. on Plasma Science,* vol. 44, no. 10, p. 2438 – 2445, 2016.

[51] T. Li, G. Wu, L. Zhou, G. Gao, W. Wang, B. Wang, D. Liu, D. Li, "Pantograph Arcing's Impact on Locomotive Equipments," *IEEE 57th Holm Conlerence on Electrical Contacts (Holm),* pp. 1 - 5, 2011.

[52] Z. Hongyi, L. Zhigang, C. Ye, H. Ke, "Extended black-box model of pantograph arcing considering varying pantograph detachment distance," in *IEEE Transportation Electrification Conference and Expo*, Asia-Pacific (ITEC Asia-Pacific), 2017.

[53] W. G. Wang, "Experimental study on electrical characteristics of pantograph arc," *Low Voltage Electrical Apparatus,* vol. 6, pp. 5-10, 2012.

[54] S. Dan, H. Ouyang, JE. Mottershead, "Vibration of a beam excited by a moving oscillator considering separation and reattachment," *Journal of Sound and Vibration,* vol. 310, pp. 1128-1140, 2008.

[55] Wang Q., "Electric arc theory," *Beijing, China: Machinery Industry Press,* p. 162–167, 1982.

[56] G. Q. Gao, "Study on the mechanism and suppression method of transient overvoltage in the state of fast train," *Chengdu: School of Electrical Engineering, Southwest Jiaotong University,* 2011.

[57] K. Shaarbafi, "Transformer Modelling Guide," Calgary, Alberta, 2014.

[58] Lin, C.E., Cheng, C.L., Huang, C.L., et al., "Investigation of magnetizing inrush current in transformers. I. Numerical simulation," *IEEE Trans. Power Deliv.,* vol. 8, p. 246–254, 1993.

[59] Persson, M., Baig, W., Thiringer, T., "Measurements and modelling of threeand five-limb transformer behaviour during large voltage and frequency disturbances," *IET Gener. Transm. Distrib.,* vol. 10, p. 334–340, 2016.

[60] Rico, J.J., Acha, E., Madrigal, M., "The study of inrush current phenomenon using operational matrices," *IEEE Trans. Power Deliv.,* vol. 16, p. 231–237, 2001.

[61] Adly, A.A., "Computation of inrush current forces on transformer windings," *IEEE Trans. Magn.,* vol. 37, p. 2855–2857, 2855–2857.

[62] Wu, Q., Jazebi, S., Leon, D.F., "Parameter estimation of three-phase transformer models for low-frequency transient studies from terminal measurements," *IEEE Trans. Magn.,* vol. 53, p. 710–718, 2017.

[63] Bronzeado, H., Yacamini, R., "Transformer inrush calculations using a coupled electromagnetic model," *IEEE Proc. Sci. Meas. Tech.,* vol. 141, p. 491–498, 1994.

[64] Smith, K.S., Ran, L., Leyman, B., "Analysis of transformer inrush transients in offshore electrical systems," *IEEE Proc. C Gener. Transm. Distrib.,* vol. 146, p. 89–95, 1999.

[65] Chen, X.S., Neudorfer, P., "Digital model for transient studies of a three-phase five-legged transformer," *IEEE Proc. C Gener. Transm. Distrib.,* vol. 139, p. 21–27, 1992.

[66] Wen, Xishan & Zhang, Jingzhuo & Lu, Hailiang., "Automatic J–A Model Parameter Tuning Algorithm for High Accuracy Inrush Current Simulation," *Energies,* 2017.

[67] M. A. Rahman and A. Gangopadhayay, "Digital simulation of magnetizing inrush currents in three phase transformers," *IEEE Trans. Power Del,* Vols. PWRD-1, no. 4, p. 235–242, 1986.

[68] T. Noda, H. Nakamoto, and S. Yokoyama, "Accurate modeling of core-type distribution transformers for electromagnetic transient studies," *IEEE Trans. Power Del,* vol. 17, no. 4, p. 969–976, 2002.

[69] M. Elleuch and M. Poloujadoff, "A contribution to the modeling of three phase transformers using reluctances," *IEEE Trans. Magn.,* vol. 32, no. 2, p. 335–343, 1996.

[70] M. Elleuch and M. Poloujadoff, "New transformer model including joint air gaps and lamination anisotropy," *IEEE Trans. Magn.,* vol. 34, no. 5, p. 3701–3711, 1998.

[71] Z. Zhang, X. Yin, W. Cao, X. Yin, "The Mathematical Analysis and Modeling Simulation of Complex Sympathetic Inrush for Transformers," in *IEEE Conference*, London, UK, 2017.

[72] V. Oiring de Castro Cezar, P. Lombard, A. Charnacé, O. Chadebec, L-L. Rouve, J-L. Coulomb, F-X. Zgainski and B. CaillaultS., "Numerical simulation of inrush currents in single-phase transformers using the Jiles-Atherton model and the finite element method," in *IEEE Conference on Electromagnetic Field Computation (CEFC)*, Miami, FL, USA, 2016.

[73] O. Ozgonenel H. Dirik I. Guney O. Usta, "A New Transformer Hysteresis Model in MATLAB ™ Simulink," in *IEEE Bucharest PowerTech*, Bucharest, Romania, 2009.

[74] NAIDU, S.R., "Simulation of the hysteresis phenomenon using Preisachs theory," *IEE Proc.,* vol. 137, no. 2, pp. 73-79, 1990.

[75] MAYERGOYZ, 1.D., "Mathematical models of hysteresis," *IEEE Trans., Mag-22,* pp. 603-608, 1986.

[76] J.G. Zhu, S.Y.R. Hui, V.S. Ramsden, "Discrete modeling of magnetic cores including hysteresis eddy current and anomalous losses," *Proc. Inst. Elect. Eng.,* vol. 140, p. 317–322, 1993.

[77] Jiles, D.C.; Atherton, D.L., "Theory of ferromagnetic hysteresis," *J. Magn. Magn. Mater.,* vol. 61, p. 48–60, 1986.

[78] Faiz, J., Saffari, S., "Inrush current modeling in a single-phase transformer," *IEEE Trans. Magn.,* vol. 46, p. 578–581, 2010.

[79] Joern Schliewe ; Stefan Schefler ; Matthias Koeppen ; Stefan Weber, "Adaptation of the Jiles Atherton model based on measurements on the anhysteresis of magnetic material," in *PCIM Europe 2019; International Exhibition and Conference for Power Electronics, Intelligent Motion, Renewable Energy and Energy Management*, Nuremberg, Germany, July 2019.

[80] Wang, X., Thomas, D.W.P., Sumner, M., et al., "Characteristics of Jiles–Atherton model parameters and their application to transformer inrush current simulation," *IEEE Trans. Magn.,* vol. 44, no. 3, p. 340–345, 2008.

[81] Chen, S.D., Lin, R.L., Cheng, C.K., "Magnetizing inrush model of transformers based on structure parameters," *IEEE Trans. Power Deliv.,* vol. 20, p. 1947–1954, 2005.

[82] Wang, Y., Abdulsalam, S.G., Xu, W., "Analytical formula to estimate the maximum inrush current," *IEEE Trans. Power Deliv.,* vol. 23, p. 1266– 1268, 2008.

[83] Jazebi, S., de Leon, F., Wu, N., "Enhanced analytical method for the calculation of the maximum inrush currents of single-phase power transformers," *IEEE Trans. Power Deliv.,* vol. 30, p. 2590–2599, 2015.

[84] Zirka, S.E., Moroz, Y.I., Arturi, C.M., et al., "Topology-correct reversible transformer model," *IEEE Trans. Power Deliv.,* vol. 27, p. 2037–2045, 2012.

[85] Girgis, R.S., Tenyenuis, E.G., "Characteristics of inrush current of present designs of power transformers," *IEEE Power Eng, Soc. General Meeting,* vol. 12, p. 1–6, 2007.

[86] Holcomb, J.E., "Distribution transformer magnetizing inrush current," *Trans. AIEE, Part III: Power Appar. Syst.,* vol. 80, p. 697–702, 1961.

[87] Specht, T.R., "Transformer magnetizing inrush current," *Trans. Am. Inst. Electr. Eng.,* vol. 70, p. 323–328, 1951.

[88] Bertagnolli, G., "Short-circuit duty of power transformers: the ABB approach," Golinelli, Formigine, 1996.

[89] A. Moradi and S. M. Madani, "Technique for inrush current modelling of power transformers based on core saturation analysis," *IET Generation, Transmission & Distribution,* vol. 12, no. 10, pp. 2317-2324, 2018.

[90] M. F.Jaafar, M. A. Jabri, "Study and Modeling of Ferromagnetic Hysteresis," in *International Conference on Electrical Engineering and Software Applications*, Tunisia, 2013.

[91] W. T. Conffey, Yu. P. Kalmyyov and J.Waldron, The Langevin Equation with Applications in Physics, Chemistry and Electrical Engineering, 1996.

[92] T.C. Monteiro, F.O. Martinz, L. Matakas, W. Komatsu, "Transformer Operation at Deep Saturation: Model and Parameter Determination," *IEEE Trans. Ind. Appl.,* vol. 48, p. 1054–1063, 2012.

[93] Mañana, E & Ortiz, M & Renedo, A & Eguíluz, C & Pérez, L & Delgado, S., "A simplified electrical model of small PEM fuel cell," *Renewable Energy and Power Quality Journal,* 2006.

[94] San Martin, Idoia & Ursúa, Alfredo & Sanchis, Pablo, "Modelling of PEM Fuel Cell Performance: Steady-State and Dynamic Experimental Validation," *Energies,* 2014.

[95] Dicks, Andrew & Rand, David., Fuel Cell Systems Explained, 2018.

[96] Prater, K.B., "Polymer electrolyte fuel cells: a review of recent developments," *Journal of Power Sources,* vol. 51, pp. 129-144, 1994.

[97] Becherif, M., Saadi, A., Hissel D., Aboubou, A., Ayad, M.Y., "Static and dynamic proton exchange membrane Fuel Cell models," *Int. J. of Hydrocarbons Mines and Environmental Research, ISSN: 2107-6510,* vol. 2, no. 1, pp. 19-26, 2011.

[98] Lee, Dong-Jing; Wang, Li, "Dynamic and Steady-State Performance of PEM Fuel Cells under Various Loading Conditions," in *IEEE Power Engineering Society General Meeting*, Tampa, FL, USA, 2007.

[99] Caisheng Wang ; M.H. Nehrir ; S.R. Shaw, "Dynamic models and model validation for PEM fuel cells using electrical circuits," *IEEE Transactions on Energy Conversion,* vol. 20, no. 2, pp. 442 - 451, 2005.

[100] Mohamed Becherif, Aïcha Saadi, Daniel Hissel, Abdennacer Aboubou, Mohamed Yacine Ayad, "Static and dynamic proton exchange membrane fuel cell models," *Journal of Hydrocarbons Mines and Environmental Research,* vol. 2, no. 1, 2011.

[101] Ishwar PrasadSahu, Gali Krishna, Manojit Biswas, Mihir Kumar Das, "Performance Study of PEM Fuel Cell under Different Loading Conditions," in *4th International Conference on Advances in Energy Research (ICAER 2013)*, India, 2014.

[102] Ambrosio B. Cultura, Ziyad M. Salameh, "Dynamic Analysis of a Stand Alone Operation of PEM Fuel Cell System," *Journal of Power and Energy Engineering,,* vol. 2, pp. 1-8, 2014.

[103] M. Becherif, D. Hissel, S. Gaagat, M. Wack, "Electrical equivalent model of a proton exchange membrane fuel cell with," *Elsevier Renewable Energy,* vol. 36, pp. 2582-2588, 2011.

[104] Maher A.R. Sadiq Al-Baghdadil,, "Modelling of proton exchange membrane fuel cell performance based on semi-empirical equations," *Renewable energy,* vol. 30, pp. 1587-1599, 2005.

[105] Fmoun, P., Member, S., Gemmen, R. S., "Electrochemical Circuit Model of a PEM Fuel Cell," in *IEEE Power Engineering Society General Meeting*, Toronto, Canada, 2003.

[106] Khan, M., J., Iqbal, M. T., "Dynamic Modelling and Simulation of a Fuel Cell Generator," *Fuel cell,* vol. 5, no. 1, 2005.

[107] Sachin V. Puranik, Ali Keyhani, Farshad Khorrami, "State-Space Modeling of Proton Exchange," *IEEE transactions on energy conversion,* vol. 25, no. 3, pp. 804-813, 2010.

[108] M. Bressel, M. Hilairet, D. Hissel, B. Ould-Bouamama, "Dynamical modeling of Proton Exchange Membrane Fuel Cell and parameters," Toulouse, France, 2014.

[109] César Peraza, Jose Gregorio Diaz,J. Arteaga-Bravo,Carlos Villanueva,Francisco Gonzalez-Longatt, "Modeling and Simulation of PEM Fuel Cell with Bond Graph and 20sim," in *American Control Conference*, Washington, USA, 2008.

[110] Mathieu Bressel, Mayank Shekhar Jha, Belkacem Ould Bouamama, Mickael Hilairet, Hissel Daniel, "Bond Graph for modeling and diagnostics of Proton Exchange Membrane Fuel Cell," in *ICBGM*, montréal, Canada, 2016.

[111] G. Gandanegara, X. Roboam, B. Sareni, G. Dauphin-Tanguy, "Modeling and Multi-time Scale Analysis of Railway Traction Systems Using Bond Graphs," in *Proceedings of International Conference on Bond Graph Modeling and Simulation*, 2001.

[112] Bouziane Mahmah, Ghania Morsli, Mounia Belacel, Hocine Benmoussa, Soulef Achachera, Amina Benhamou, Maïouf Belhamel, "Dynamic Performance of Fuel Cell Power Module for Mobility Applications," *Engineering,* vol. 5, no. 2, pp. 219-229, 2013.

[113] R. Talj, T. Azib, O. Béthoux, G. Remy, C. Marchand, et al., "Parameter analysis of PEM fuel cell hysteresis effects for transient load use," *European Physical Journal: Applied Physics, EDP Sciences,* vol. 54, no. 2, 2011.

[114] G. Fontes, C. Turpin, S. Astier, T.A. Meynard,, "Interactions Between Fuel Cells and Power Converters: Influence of Current Harmonics on a Fuel Cell Stack," *IEEE Trans. on Power Electronics,* vol. 22, no. 2, pp. 670-678, 2007.

[115] D. Gerteisen, T. Heilmann and Ch. Ziegler, "Modeling the phenomena of dehydration and flooding of a polymer electrolyte membrane fuel cell," *Journal of Power Sources,* vol. 187, no. 1, pp. 165-181, 2009.

[116] J.-M. Le Canut, R. Latham, W. Mérida and D.A. Harrington, "Impedance study of membrane dehydration and compression in proton exchange membrane fuel cells," *Journal of Power Sources,* vol. 192, no. 2, pp. 457-466, 2009.

[117] C.H. Li, X.P. Ji, Q.J. Zeng, Y.L. Wang and X.D. Wu, "Modeling and performance analysis of PEM fuel cell system," *Springer Science, Business Media New york,* pp. 943-951, 2014.

[118] Eng. Waseem Saeeda, Dr. Eng. Ghaith Warkozekb, "Modeling and Analysis of Renewable PEM Fuel Cell System," in *International Conference on Technologies and Materials for Renewable Energy, Environment and*, 2015.

[119] Wang, C., Nehrir, M.H., Shaw, S.R., "Dynamic models and model validation for pem fuel cells using electrical circuits," *IEEE Trans. Energy Convers,* vol. 20, no. 2, p. 442–451, 2005.

[120] M. T. Iqbal, "Simulation of a small wind fuel cell hybrid energy system," *Renew. Energy,* vol. 28, no. 4, p. 511–522, 2003.

[121] Caisheng Wang ; M.H. Nehrir ; S.R. Shaw, "Dynamic models and model validation for PEM fuel cells using electrical circuits," *IEEE Transactions on Energy Conversion,* vol. 20, no. 2, pp. 442 - 451, 2005.

[122] K. Atkinson, W. Han, D. Stewart,, Numerical Solution of ordinary differential equations, Wiley Interscience, 2009, pp. 56-62.

[123] Griffiths, David & Higham, Desmond, Numerical methods for ordinary differential equations. Initial value problems, 2010.

[124] Goel, Ankit & Bernstein, Dennis, "Parameter Estimation for Nonlinearly Parameterized Gray-Box Models," *Annual American Control Conference (ACC)*, 2018.

[125] Q. Liu, A. Ihler, "Distributed Parameter Estimation via Pseudolikelihood," in *in Proceedings of the 29th International Conference on Machine Learning*, Edinburgh, Scotland, UK, 2012.

[126] P. Chaussé, "Computing Generalized Method of Moments and Generalized Empirical Likelihood with R," *Journal of Statistical Software,* vol. 34, no. 11, pp. 1-35, 2010.

[127] D. Guo, Y. Wu, S. Shamai, S. Verdú, "Estimation in Gaussian Noise: Estimation in Gaussian Noise," *IEEE Transactions on Information Theory,* vol. 57, no. 4, pp. 2371-2385, 2011.

[128] Aluffi-Pentini, F., Parisi, V. and Zirilli, F., "Global Optimization and Stochastic Differential Equation," *Journal of Optimization Theory and Applications,* vol. 47, p. 1–16, 1985.

[129] Rainer Martin Storn, Kenneth Price, "Differential Evolution - A Simple and Efficient Heuristic for Global Optimization over Continuous Spaces," *Journal of Global Optimization,* vol. 11, no. 4, pp. 341-359, 1997.

[130] Swagatam Das, Ponnuthurai Nagaratnam Suganthan, "Differential Evolution: A Survey of the State-of-the-Art," *IEEE transactions on evolutionary computation,* vol. 15, no. 1, 2011.

[131] DATAQ Instruments, 2014. [Online]. Available: https://www.dataq.com/resources/pdfs/datasheets/720_730b.pdf. [Accessed 29 01 2020].

[132] Jiles, D.C., Thoelke, J., Devine, M., "Numerical determination of hysteresis parameters for the modeling of magnetic properties using the theory of ferromagnetic hysteresis," *IEEE Trans. Magn.,* vol. 28, no. 1, pp. 27-35, 1992.

[133] E. D. M. Hernandez, C. Muranaka, and J. Cardoso, "Identification of the Jiles-Atherton model parameters using random and deterministic searches," *Physica B,* pp. 212-215, 2000.

[134] M. Hamimid, M. Feliachi, S. Mimoune, "Modified Jiles–Atherton model and parameters identification using false position method," *Physica B, Condens. Matter,* vol. 405, no. 1, pp. 1947-1950, 2010.

[135] K. Chwastek, and J. Szczyglowski, "An Alternative Method to Estimate the Parameters of Jiles-Atherton Model," *Journal of Magnetism and Magnetic Materials,* vol. 314, no. 1, pp. 47-51, 2007.

[136] Xiaohui, W., David, W.P.T., Mark, S., et al., "Numerical determination of Jiles-Atherton model parameters," *COMPEL-Int. J. Comput. Math. Electr. Electron. Eng.,* vol. 28, no. 2, pp. 493-503, 2009.

[137] Wang, X., Thomas, D.W.P., Sumner, M., et al., "Characteristics of Jiles–Atherton model parameters and their application to transformer inrush current simulation," *IEEE Trans. Magn.,* vol. 44, no. 3, p. 340–345, 2008.

[138] D. Zhang, Y. Liu, S. Huang, "Differential Evolution Based Parameter Identification of Static and Dynamic J-A Models and Its Application to Inrush Current Study in Power Converters," *IEEE Trans. Magn., Vol.,* vol. 48, no. 11, pp. 3482-3485, 2012.

[139] Salciccioli, Justin & Crutain, Yves & Komorowski, Matthieu & Marshall, Dominic., Sensitivity Analysis and Model Validation, 2016.

[140] Saltelli, A., S. Tarantola, F. Campolongo and M. Ratto, Sensitivity Analysis in Practice: A Guide to Assessing Scientific Models, England: John Wiley & Sons Ltd, 2004.

[141] J.P.C. Kleijnen, "Sensitivity analysis and optimization in simulation: design of experiments and case studies," in *Winter Simulation Conference Proceedings*, Arlington, VA, USA, USA, 1995.

[142] Eric D. Smith, Ferenc Szidarovszky, William J. Karnavas and A. Terry Bahill, "Sensitivity Analysis, a Powerful System Validation Technique," *The Open Cybernetics and Systemics Journal,* vol. 2, pp. 39-56, 2008.

[143] J. P. C. Kleijnen, "An overview of the design and analysis of simulation experiments for sensitivity analysis," *Eur. J. Oper. Res.,* vol. 164, no. 2, pp. 287-300, 2005.

[144] D. G. Cacuci, "Sensitivity and uncertainty analysis," *Chapman & Hall / CRC Press, Boca Raton, FL,* 2005.

[145] Jack P.C. Kleijnen, "Experimental design for sensitivity analysis, optimization, and validation of simulation models," *Tilburg: Operations research,* vol. 15, 2001.

[146] B. Wayne Bequette, "Process Control : Modeling, Design, and Simulation," *IEEE control systems,* 2003.

[147] G. Abdulsalam, W. Xu, W.L.A. Neves, X. Liu, "Estimation of Transformer Saturation Characteristics from Inrush Current Waveforms," *IEEE Trans. Power Deliv.,* vol. 21, p. 170–177, 2006.

[148] Mathieu Bressel, Mayank Shekhar Jha, Belkacem Ould Bouamama, Mickael Hilairet, Hissel Daniel, "Bond Graph for modeling and diagnostics of Proton Exchange Membrane Fuel Cell," in *ICBGM 2016*, Montréal, Canada, 2016.

[149] Peraza, César & Díaz, José & Arteaga, Francisco & Villanueva, Carlos & Gonzalez-Longatt, Francisco, "Modeling and simulation of PEM fuel cell with bond graph and 20sim," in *Proceedings of the American Control Conference*, Washington, USA, 2008.

[150] L. Petzold, L. Jay, and J. Yen, "Numerical solution of highly oscillatory ordinary differential equations," *Acta Numerica 6, Cambridge University Press,* 1997.